

**Numerical Simulation of Ground Movements and Structural Forces in Lining  
for Earth Pressure Balance (EPB) Tunneling in Clay**

by

**Vasiliki Founta**

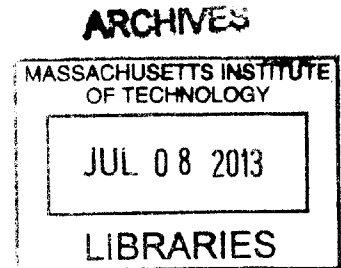
**Diploma in Civil Engineering (2011)  
National Technical University of Athens**


**Submitted to the Department of Civil and Environmental Engineering  
in Partial Fulfillment of the requirements for the Degree of  
Master of Science in Civil and Environmental Engineering**

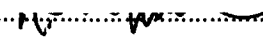
at the

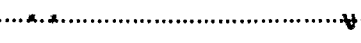
**Massachusetts Institute of Technology  
June 2013**

**© 2013 Massachusetts Institute of Technology  
All rights reserved**



Signature of Author.....  
  
Department of Civil and Environmental Engineering  
May 24, 2013

Certified by.....  
  
Andrew J. Whittle  
Professor of Civil and Environmental Engineering  
Thesis Supervisor

Accepted by.....  
  
Heidi M. Nepf  
Chair, Departmental Committee for Graduate Students



# **Numerical Simulation of Ground Movements and Structural Forces in Lining for Earth Pressure Balance (EPB) Tunneling in Clay**

by

**Vasiliki Founta**

Submitted to the Department of Civil and Environmental Engineering on May 24 2013, in Partial Fulfillment of the requirements for the Degree of Master of Science in Civil and Environmental Engineering

## **Abstract**

This thesis describes the development of a 3D finite element model for representing mechanized tunnel construction using an Earth Pressure Balance (EPB) machine in clay. The model uses the commercial FE code, Plaxis 3D, to represent the face pressure, conical shield, grouting process and activation of precast segmental concrete lining systems through a set of boundary conditions that advance through the soil mass along a prescribed trajectory. The model simulates ground conditions associated with on-going EPB tunnel construction for the Crossrail project in central London. The analyses use a linearly-elastic perfectly plastic (MC) soil model based on design profiles of undrained shear strength and stiffness characteristics of London Clay. The analyses show the importance of the in situ  $K_0$ -effective stress conditions on predictions of the free-field, short-term (i.e., undrained) ground movements caused by tunnel construction as well as the structural forces induced in the segmental lining. The results of the model are in good overall agreement with simulations from a more complex finite element model that uses sub-structuring to represent the EPB machine (Kratos-ekate program; done in collaboration with the research group at TU Bochum). The results of this study form the basis for more extensive research on time dependent ground response and interactions with overlying structures.

Thesis Supervisor: Andrew J. Whittle  
Title: Professor of Civil and Environmental Engineering





## **Acknowledgments**

First and foremost, I want to thank my advisor Prof. Andrew Whittle for his guidance and support throughout my studies at MIT. His knowledge and in-depth understanding of geotechnical engineering concepts had provided me with invaluable help to overcome all the difficulties encountered in this research. He helped me to stay motivated and focused making the whole MIT experience as beneficial as possible.

I am really grateful to Nina, Zhandos, Eva, Yixing, Despina and the rest of the people in my research group for sharing their experience and knowledge with me helping me get through the problems that came up during this work.

Then I would like to truly thank my friends Mariam, Shehab, Albalyra, Alessandra and Rachel for being there for me and making MIT feel like home. I would always cherish the time we spend together.

Finally, I want to thank my parents, my brother Vasilis and my boyfriend Christos for loving me, patiently supporting me and reminding me what are the important things in life.



# Table of Contents

---

<b>1</b>	<b>INTRODUCTION .....</b>	<b>17</b>
<b>2</b>	<b>BACKGROUND .....</b>	<b>29</b>
2.1	INTRODUCTION .....	29
2.2	BORED TUNNELING METHODS.....	29
2.2.1	Conventional open-face tunneling.....	29
2.2.2	Open-face shield tunneling .....	30
2.2.3	Closed-face shield tunneling .....	31
2.3	METHODS FOR PREDICTING GROUND MOVEMENTS.....	33
2.3.1	Empirical methods for ground movements.....	34
2.3.2	Analytical solutions for ground movements .....	38
2.3.3	Numerical simulations of tunnel construction .....	39
<b>3</b>	<b>DEVELOPMENT AND VALIDATION OF FE MODEL FOR TUNNELING .....</b>	<b>57</b>
3.1	INTRODUCTION .....	57
3.2	EVALUATION OF 2D NUMERICAL SOLUTIONS .....	57
3.3	COMPARISON WITH CONVENTIONAL STRESS REDUCTION METHOD .....	59
3.4	3D MODEL OF UNLINED TUNNEL .....	60
3.4.1	Comparison of Plaxis 2D with Plaxis 3D for the unlined case .....	62
<b>4</b>	<b>FINITE ELEMENT MODEL FOR EPB TUNNELING .....</b>	<b>77</b>
4.1	MODEL DESCRIPTION .....	77
4.2	RESULTS .....	81
4.2.1	Ground deformations .....	81
4.2.2	Comparison of surface settlements .....	83
4.2.3	Comparison of tunnel cavity deformations.....	84
4.2.4	Comparison of structural forces.....	85
4.3	EFFECTS OF FACE AND GROUT PRESSURE.....	87

4.3.1	Grout pressure.....	88
4.3.2	Face pressure.....	89
<b>5</b>	<b>EFFECT OF FE ASSUMPTIONS ON EPB TUNNELING PERFORMANCE .....</b>	<b>113</b>
5.1	COMPARISON OF BASE CASE 3D MODEL WITH KRATOS .....	113
<b>6</b>	<b>SUMMARY, CONCLUSIONS AND RECOMMENDATIONS.....</b>	<b>125</b>
<b>7</b>	<b>REFERENCES .....</b>	<b>129</b>
<b>8</b>	<b>APPENDICES .....</b>	<b>135</b>
A.	HARDENING GROUT MODEL.....	135
B.	SCRIPTS FOR COMPUTING TUNNEL INDUCED DISPLACEMENTS USING ANALYTICAL SOLUTIONS .....	141

# List of Figures

Figure 1.1 Regular Cross-section for NATM method (source: FHWA, 2011)..... 23

Figure 1.2 Excavation sequence of the NATM method ( Machi, 2004)..... 23

Figure 1.3 Routing map of extension of the Washington Metro line to Dulles Airport ..... 24

Figure 1.4 Cut-and-cover construction method ( Wong, 2004) ..... 24

Figure 1.5 Amsterdam Metro North/South Line that will be mainly constructed using the cut-and-cover method (source: Net Resources International, 2012)..... 25

Figure 1.6 Types of TBMs (source: FHWA,2011) ..... 26

Figure 1.7 Excavation sequence for Earth Pressure balance (EPB) machine ..... 26

Figure 1.8 Herrenknecht EPB machine used for Crossrail (London)..... 26

Figure 1.9. Regional map of Crossrail Project, new railway underneath central London ..... 27

Figure 1.10 Sources of ground movements associated with tunneling (after Möller, 2006) ..... 28

Figure 2.1 Support elements for sequential excavation, NATM method ( Moller,2006)..... 45

Figure 2.2 Excavation sequence for open face shield tunneling ( Moller, 2006) ..... 45

Figure 2.3 Closed face shield tunneling methods ( Moller, 2006)..... 46

Figure 2.4 Schematic figure of grout injection in the tail void ( Moller, 2006) ..... 46

Figure 2.5 Schematic figure of the assembled precast segmental lining (source: FHWA,2011).. 47

Figure 2.6 Empirical function for transversal settlement trough ..... 47

Figure 2.7 Empirical estimation of inflexion point ( after Mair and Taylor, 1997)..... 48

Figure 2.8 Horizontal ground movement and strain (Mair et.al 1996) ..... 48

Figure 2.9 Under the assumption of equation (2.5) the vectors of the transverse surface displacements are directed to the center of the tunnel. .... 49

Figure 2.10 Variation of trough width parameter $K$ with normalized depth ( $y/H$ ) for tunnels in clay (Mair et.al, 1993) .....	49
Figure 2.11 Longitudinal surface displacement above tunnel centerline .....	50
Figure 2.12 Deformation modes around tunnel cavity .....	51
Figure 2.13 Comparison of computed and measured subsurface ground movements for WB JLE tunnel: (a) vertical displacements; (b) horizontal displacements (Zymnis et.al, 2013) .....	52
Figure 2.14 Effect of input parameters on surface settlement distribution .....	53
Figure 2.15 Stress reduction method ( Möller, 2006) .....	53
Figure 2.16 Step-by-step simulating of open face, NATM tunneling ( Möller, 2006) .....	53
Figure 2.17 Dimensions and mesh of the 2D and 3D models ( Möller, 2006).....	54
Figure 2.18 Transverse settlement troughs for 3D and 2D analyses for different $K_0$ values .....	54
Figure 2.19 Display of grout pressure method (Möller, 2006) .....	55
Figure 2.20 Step-by-step simulating of closed face, shield tunneling (Möller, 2006) .....	55
Figure 3.1. 2D Finite element model and imposed boundary conditions .....	65
Figure 3.2. 15-node triangular elements used in Plaxis 2D FE model .....	65
Figure 3.3. Comparison of ground surface deformations for Plaxis 2D and analytical solutions (Verruijt, 1997).....	66
Figure 3.4 . Comparison of ground surface deformations for Plaxis 2D unlined elastic undrained case to the approximate analytical solutions (Pinto and Whittle, 2012) .....	66
Figure 3.5 Buoyancy effect for the undrained unlined elastic 2D FE model (Elastic analysis) ....	67
Figure 3.6 The ground surface deformations induced by volume loss computed by Plaxis 2D unlined elastic undrained model are compared to the approximate analytical solutions. ....	68

Figure 3.7 Comparison of ground surface deformations for Plaxis 2D unlined undrained model, for the three different three different strength and stiffness soil profiles for elastic and plastic case. ....	68
Figure 3.8 Comparison of zone of yield around tunnel for three different strength and stiffness soil profiles, for the 2D unlined FE model (elasto-plastic soil model M-C) .....	69
Figure 3.9 Comparison of ground surface deformations for Plaxis 2D unlined undrained model, for the design line(plastic soil model M-C) for $\beta$ -value varying from 0-0.5.....	69
Figure 3.10 Comparison of zone of yield around tunnel for for $\beta=0 - 0.5$ , for the 2D unlined FE model (design line , elasto-plastic soil model M-C).....	70
Figure 3.11. Elements used in Plaxis 3D FE model .....	70
Figure 3.12 Mesh and dimensions for 3D Finite element model .....	71
Figure 3.13 Excavation procedure for unlined tunnel .....	71
Figure 3.14 Examined central cross-section of the FE model and the three different positions of the face of the excavation .....	72
Figure 3.15 Comparison of ground surface deformations at central section of FE model ( $y'= 0$ ) for 3D and 2D FE models for the unlined case with a Mohr-Coulomb soil model.....	73
Figure 3.16 Comparison of ground surface deformations as a function of the position of the excavation face at the centerline ( $x=0$ ) of the central section of FE model ( $y'= 0$ ) for 3D unlined case with the empirical method proposed by Attewell and Woodman (1982). ....	74
Figure 3.17 Zone of yield around tunnel for unlined case for the three different positions of the face of the excavation.....	75
Figure 4.1 Soil Profile at Paddington Station area (source: Crossrail Report, 2012) .....	91

Figure 4.2. Schematic representation of the FE model used for the tunnel excavation.....	92
Figure 4.3 Precast segmental lining system.....	92
Figure 4.4 Shape of conical EPB shield (a) dimensions of the shield based on the diameter of the front shield, center shield and tailskin, (b) comparison of the applied displacements on the crown nodes of the shield skin in the 3D model to the desired shape of the shield, for three different positions of the EPB face shield.....	93
Figure 4.5 The buoyancy effect that cancels out the weight of the machine .....	94
Figure 4.6 Contours of ground displacements $ u $ at the three locations of the EPB machine for $K_0=1$ and $K_0=1.5$ .....	95
Figure 4.7 Deformed mesh scaled up by 50 times, at the three locations of the EPB machine for $K_0=1$ and $K_0=1.5$ .....	96
Figure 4.8. (Cont'd) Effect of $K_0$ -conditions on computed surface deformations at mid-section of the base case FE model simulating EPB tunneling London Clay.....	98
Figure 4.9 Middle-plane ( $y'= 0$ ) and the five selected locations to be examined along the mid-plane .....	99
Figure 4.10. Development of surface displacements as functions of the EPB face location at five different locations along the mid-plane of FE model for $K_0$ 1.0 and 1.5 (a) settlements $u_z$ longitudinal and (b) displacements $u_y$ .....	100
Figure 4.11 Displacement trajectories for surface points along the center-plane of the base case FE model of EPB tunneling in London Clay for $K_0$ 1.0 and 1.5 values.....	101
Figure 4.12. Effect of $K_0$ -conditions on interpreted cavity deformation mode parameters from base case FE model of EPB tunneling in London Clay.....	102



Figure 4.13 Contours of mobilized shear strength  $\tau_{rel}$  showing effect of  $K_0$ -conditions on extent of plastic yielding around EPB tunnel in London clay ..... 104

Figure 4.14. Structural forces in linings for  $K_0$  1.0 and 1.5 values, for the lining ring located at the middle plane, after construction process is completed ..... 105

Figure 4.15 Structural forces in linings for  $K_0$  1.0 and 1.5 values, for the lining ring located in the middle plane, when the ring is first activated  $y'/D = -1.9$  and at the end of the construction process  $y'/D = -7$ . ..... 106

Figure 4.16 Structural forces in lining for crown, springline and invert for the lining ring located at the middle plane ( $y' = 0$ ) for  $K_0=1$  and  $K_0=1.5$  as a function of the EPB position. .... 107

Figure 4.17 Interaction diagram M-N for segmental lining with the values of the computed structural forces in the lining for  $K_0$  1.0 and 1.5 values corresponding to the 3D base case model (source :Iftimie, 1996)..... 107

Figure 4.18 Comparison of ground surface deformations at central section of FE model ( $y' = 0$ ) for grout pressure 50 to 200 kPa ..... 108

Figure 4.19 Structural forces in the middle ring ( $y' = 0$ ) for  $K_0$  1.0 and 1.5 values at grout pressure 50 to and 200 kPa ..... 109

Figure 4.20 Comparison of structural forces as a function of the EPB position, at the crown, springline and invert, for grout pressure 50 kPa to 200 kPa at the middle lining ring, for  $K_0$  1.0 and 1.5 values. .... 110

Figure 4.21 Comparison of ground surface deformations at central section of FE model ( $y' = 0$ ) for face pressure 100 to 250 kPa ..... 111

Figure 5.1 Modelling approaches for EPB mechanized tunnelling: a) Plaxis 3D™ b) Kratos-Ekate (source : Whittle et.al, 2013) .....	120
Figure 5.2 3D for closed face tunnelling: Step-by-step simulation procedure: (a) End of previous excavation step; (b) advance of the TBM; and (c) excavation of the soil and introduction of elements representing the tail void grout and the lining.( Kasper and Meschke, 2004) .....	120
Figure 5.3 Comparison of surface settlements trough for Plaxis and Kratos FE models for different positions of machine with respect to middle cross section (source : Founta et.al, 2013) .....	121
Figure 5.4 Comparison of surface settlements trough for Plaxis (P) and KRATOS (K) model for different positions of machine with respect to middle cross section .....	122
Figure 5.5 Structural forces in linings for two different modelling approaches and $K_0$ values, for the lining ring in the middle after construction process is completed.....	123
Figure A.1 Time-dependent Young's moduli of the tail void grout .....	138
Figure A.2 Grouting cube test results: Compressive strength (MPa) as a function of time (h) (Source:Crossrail Geotechnical report 2012-2013) .....	138
Figure A.3 Grout stiffness as a function of time. Comparison between: i) Kasper and Meschke, (2006), ii) Van der Stoel and Van Ree (2000) and ACI using laboratory data from the Crossrail Project and iii)value used for Plaxis 3D base case model.....	139
Figure A.4 Structural forces in the middle ring ( $y'= 0$ ) for Kasper and Meschke,2006 model are compared to the base case model (Crossrail) for $K_0=1$ and $K_0=1.5$ .....	140

## List of Tables

Table 2.1 Analytical solutions for ground deformations around a shallow tunnel .....	44
Table 3.1 Soil properties for the 2D FE model using the stress reduction method ( $\beta$ -method)..	64
Table 3.2 Input parameters for MC model of London Clay based on C300 design profile .....	64
Table 4.1. Properties of tunnel lining and grout.....	90
Table 5.1 Material properties used in FE models .....	119
Table A.1 Grout hardening properties for Kasper and Meschke2006 versus Crossrail data .....	137



# 1 Introduction

Due to improved access to community resources (entertainment, health care etc.) and presumed economic advantages of living in urban areas, the population in most large cities is increasing, at a rate higher than the rest of the population. As a result there is a great demand for infrastructure that can provide cost-effective, efficient and environmentally-friendly urban transportation (e.g., Laver, 1970). The key decisions on the type of transit system (elevated, at-grade or underground) depend on various conditions and parameters such as the capital costs, visual/aesthetic impacts, construction impacts, operational costs, air pollution, risk etc. Underground transportation solutions are usually preferred in urban environments due to the lack of space, high price of surface real estate, preservation of historical areas, minimization of disruption and traffic congestion associated with surface projects (ITA, 2004).

The most common methods for constructing large diameter tunnels in urban areas are cut-and-cover methods, sequential excavation and support (e.g. NATM), and tunnel boring machines (TBM's). The New Austrian Tunneling Method (NATM), also known as the Sequential Excavation Method (SEM) has been widely used for at least 40 years in both rural and urban areas (FHWA, 2011). NATM can be characterized as an observational method, since the design is constantly adjusted based on the observed displacements and the ground conditions. A typical cross-section (**Figure 1.1**) has an ovoid shape to allow a smooth redistribution of the stresses released due to the excavation. The method can be used in rock, soft ground and a variety of other ground conditions with appropriate adjustments. Supporting measures such as rock bolts and shotcrete should be applied immediately in order to reduce/control ground displacements, and

the permanent support can be applied at a later stage (**Figure 1.2**). A recent example of the NATM method is the extension of the Washington Metro line to Dulles Airport (**Figure 1.3**).

Most of the early mass transit tunnels were constructed by cut-and-cover methods. These typically involve temporary works for supporting the initial excavation (walls and cross-lot bracing), followed by construction of the permanent works. Cut-and-cover methods have been used for underground highway projects such as the Central Artery/Tunnel (CA/T) Project in Boston (Salvucci, 2003), and multi-model Projects such as VZB (Verkehrsanlagen im Zentralen Bereich) in Berlin (Savidis and Rackwitz, 2004). **Figure 1.4** illustrates a typical bottom up construction using cut-and-cover method. The Amsterdam Metro North-South Line (**Figure 1.5**) is a recent example of a subway project that is mainly constructed using the cut-and-cover method.

TBMs are suitable for conditions ranging from soft ground (i.e, cohesive and cohesionless soils) to hard rock. A TBM consists of a main body (shield) and additional elements that are used for cutting, steering, gripping, shielding, exploratory drilling, ground control and support, lining erection, spoil removal, ventilation and power supply (FHWA, 2011). The TBMs have different characteristics depending on the soil type (soft soil or hard rock) they are intended for (**Figure 1.6**) This thesis focuses on soft ground tunneling using an earth pressure balance (EPB) machine (**Figure 1.7-Figure 1.8**). The front shield is filled with the excavated debris that is then extracted through a screw conveyor and deposited onto a belt conveyor. This screw conveyor controls mechanically the applied face pressure by matching the volume of the soil extracted from the excavation face with the volume of the soil displaced by the forward movement of the shield.

Inside the tail of the shield precast concrete units are erected to form a segmental lining system. The steering of the EPB is accomplished by hydraulic jacks that push against the previously constructed concrete lining rings. In order to reduce the displacements associated with the volume loss, grout is injected in the gap (tail void) formed between the excavated soil and the lining as the shield advances forward. The Crossrail project, a major new railway underneath central London that is currently under construction is an example of the current use of an EPB machine in urban environment (**Figure 1.9**), stations for the Crossrail project will be mined out after the main tunnel is completed.

Tunneling design requires an accurate calculation the deformations in the overlying ground as well as structural forces developed in the lining system. There are two main factors that produce surface settlements in soft ground tunneling. The first and most important are short-term deformations (i.e., ground losses associated with conditions at the face, tail void etc.) and the second are the long-term deformations due to consolidation and creep around the completed tunnel. This thesis focuses on the effects of ground loss due to tunnel construction. **Figure 1.10** illustrates the main sources of settlements for open face and closed face tunneling. For open-face tunneling the stress changes around the tunnel face and the unsupported round length are primary sources of ground movements. Whereas for the closed face systems, movements are associated with stress relief at the face overcutting and ploughing of the shield and poor control of grouting in the tail void. There are three main methods used to estimate the tunnel-induced ground deformations: a) empirical methods based on measured data from case studies, b) analytical solutions based on simplified models of soil behavior and representation of excavation process, and c) numerical analyses using finite element methods.

Although, empirical and analytical methods are valuable tools for design, numerical simulations are becoming increasingly popular as the computational time decreases and the accuracy and capabilities of the analyses increase. Two-dimensional analyses are widely used in practice, but 3D analyses are needed to represent tunneling processes (Clough and Leca, 1989).

The goal of this research is to develop, validate and interpret results from three dimensional finite element model for predicting ground movements in low permeability clays caused by closed face tunnel construction using an EPB tunnel boring machine (**Figure 1.8**). Although, finite element methods have been used to simulate tunnel construction since the early 1980s, there are still relatively few studies involving three-dimensional models of mechanized tunneling (e.g., Swoboda and Abu-Krishna, 1999) compared to conventional tunneling (i.e., open-face, sequential excavation and support) mainly due to the computational complexity associated with the simulation of TBM machine, as well and uncertainties associated with construction parameters ( face pressure, injected grout pressure, over-excavation etc ) and soil properties.

In this study, the effect of closed faced tunnel construction in soft ground is investigated by means of 2D and 3D finite element models simulating the excavation sequence associated with typical sections of Crossrail project (**Figure 1.9**) in London clay. The 118 km long new Crossrail line will connect Heathrow and Maidenhead in the West with Stratford and the Isle of Dogs in the East. The project involves the construction of two twin bored tunnels (Eastbound and Westbound) with a 7.1 m external diameter and 6.0 m internal diameter, excavated principally within the London clay unit. This highly demanding project offers a major opportunity to



advance the state of the art in predicting tunnel performance. The EPB tunneling method was selected to ensure minimum disruption of the ground surface, as the alignment passes beneath many critical structures including the existing underground transportation system. As expected the project is very well monitored providing an excellent opportunity to gain insight on the effectiveness of closed face tunneling procedures in soft ground. There are several examples of tunnels constructed in London area that have faced major problems during or after tunneling construction: i) the collapse of the concrete sprayed tunnels at Heathrow's Central Terminal Area (CTA), part of Heathrow express (HEX), a high-speed rail link from central London to Heathrow Airport, that was constructed by NATM method (Cooper et.al, 2002, Clayton et.al, 2006) and ii) the unexpectedly large movements, for open face construction, observed in St. James Park, part of the Jubilee Line Extension (JLE) Project (Nyren, 1998; Zymnis et.al., 2013). Given the uncertainties associated with prior tunnel construction in London clay there is great interest in the performance of the Crossrail EPB machine. EPB boring machines have recently been used with great success for the Channel Tunnel Rail Link CTRL (Selemetas, 2006; Woods et.al, 2007) that connects London with the Channel Tunnel, providing a good background for the Crossrail project.

This thesis contains the following:

**Chapter 2** gives a brief review on different tunneling methods focusing on closed face tunneling together with an overview of the available methods to predict ground movements due to tunneling including empirical, analytical and numerical analyses.

**Chapter 3** describes in detail the development and validation of 2D and 3D finite element models for representing tunnel construction in London clay. The computed surface displacements from 2D finite element models are compared and matched with available analytical solutions (Pinto and Whittle, 2012), while 3D analyses are compared to 2D analyses representing the unlined case.

**Chapter 4** presents the characteristics of the base case 3-D finite element model created using the Plaxis<sup>TM</sup> software. This model simulates closed face tunnel construction in London clay, using an Earth Pressure Balance (EPB) shield machine based on the geometry and soil properties at Paddington Station area of the Crossrail project. Using this model a 3-D parametric study of tunneling was carried out to measure the effect of soil properties on the settlement trough, the yielding zone and the effect of the soil properties as well as the structural stresses of the lining. Finally, parametric analyses were conducted to quantify the effects of the grout and face pressure in the resulting displacements and structural forces.

**Chapter 5** compares the results from the 3-D base case model using Plaxis with a more sophisticated 3-D model using Kratos-Ekate software developed by Kasper and Meschke (2004).

**Chapter 6** summarizes the main conclusions of this research and gives recommendations for future advancement of this study.

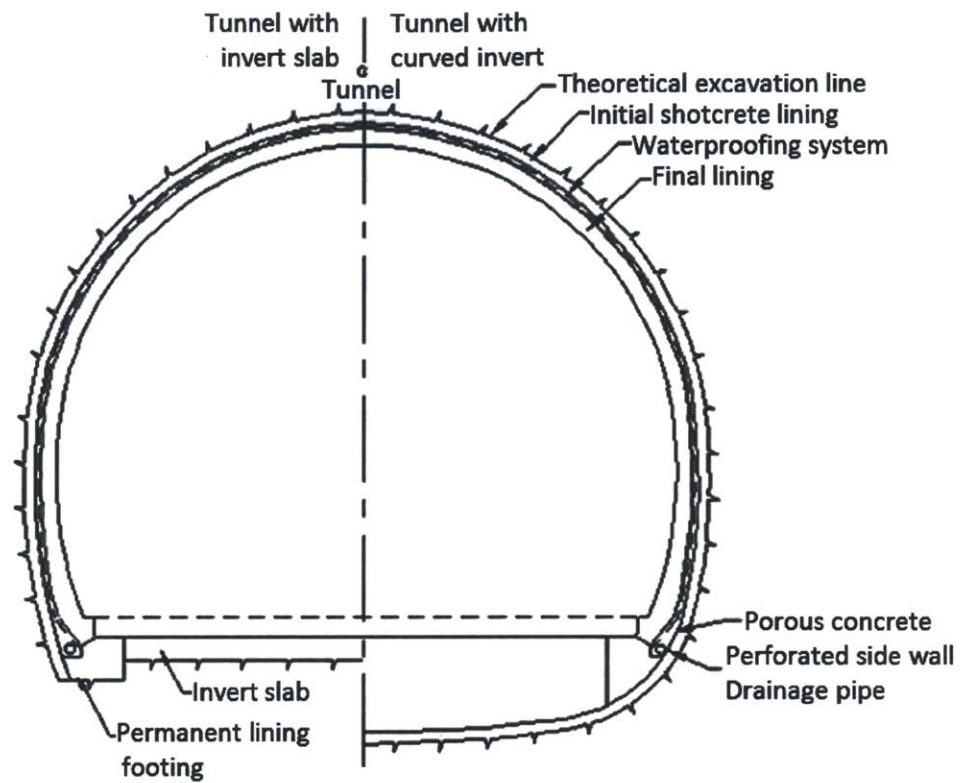


Figure 1.1 Regular Cross-section for NATM method (source: FHWA, 2011)

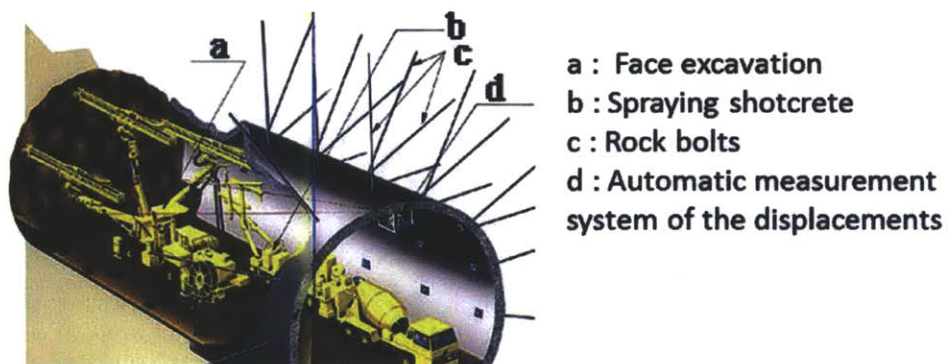


Figure 1.2 Excavation sequence of the NATM method ( Machi, 2004)

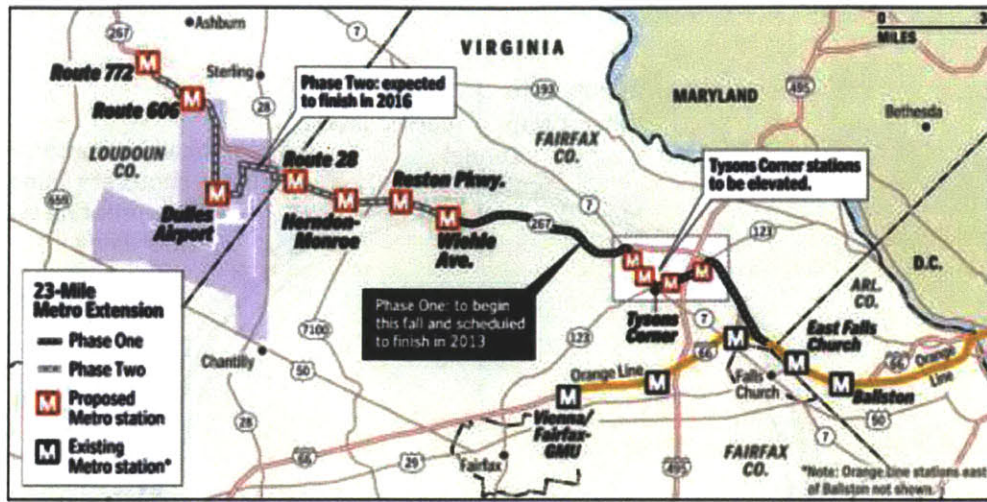


Figure 1.3 Routing map of extension of the Washington Metro line to Dulles Airport ( Layman, 2011)

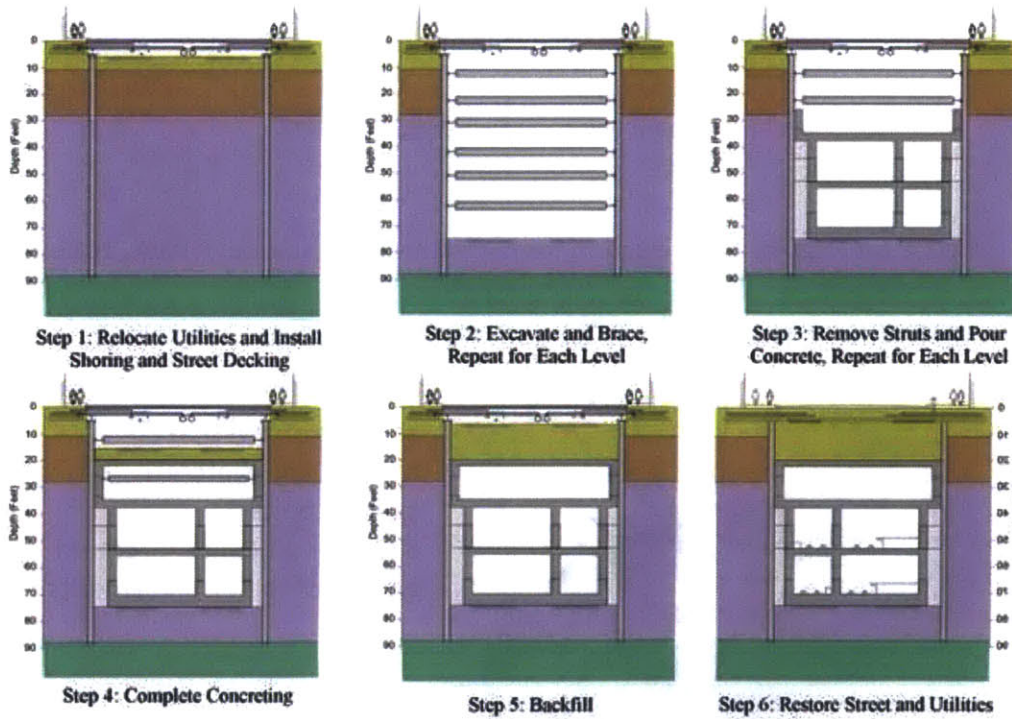


Figure 1.4 Cut-and-cover construction method ( Wong, 2004)



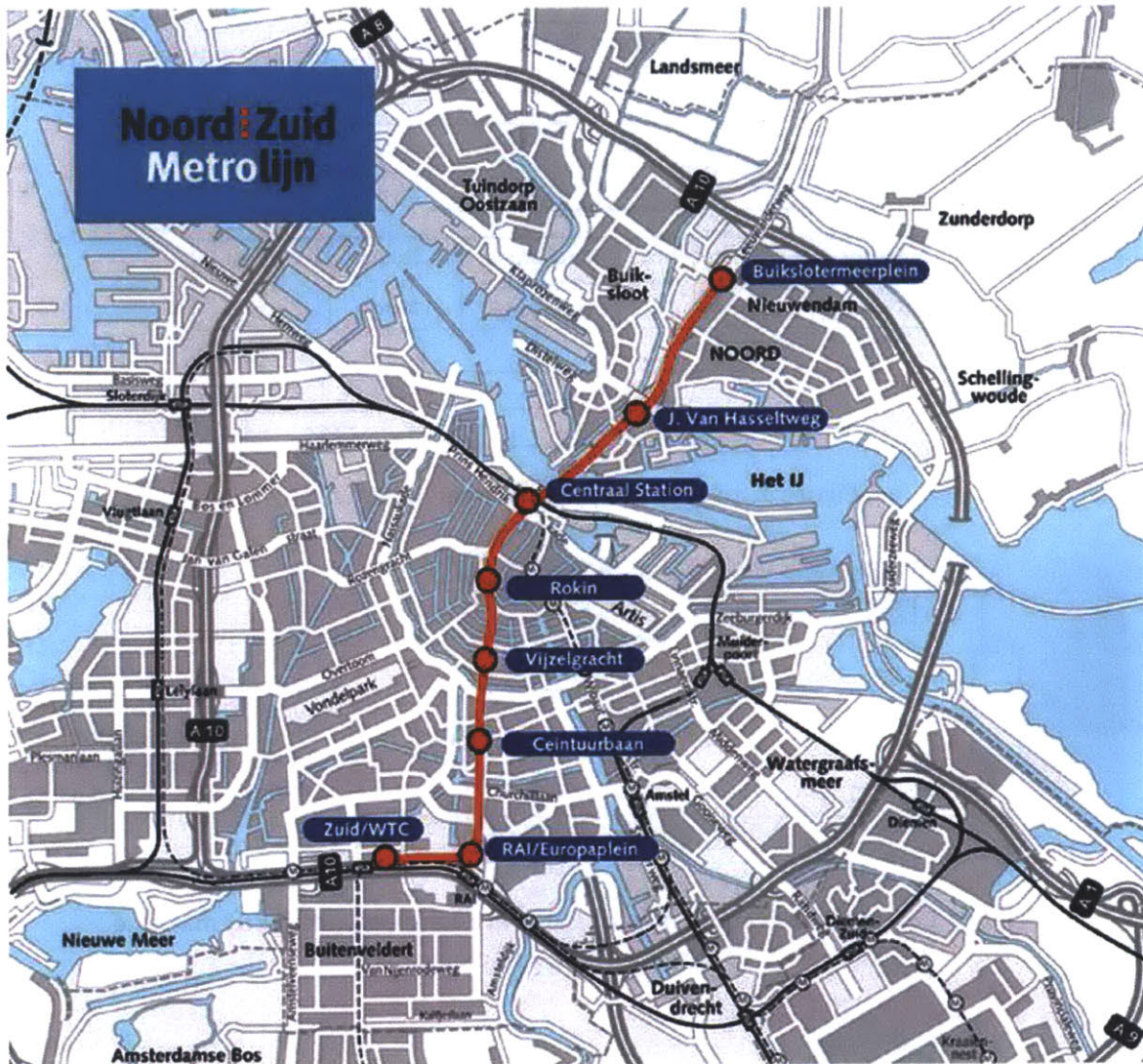


Figure 1.5 Amsterdam Metro North/South Line that will be mainly constructed using the cut-and-cover method (source: Net Resources International, 2012)

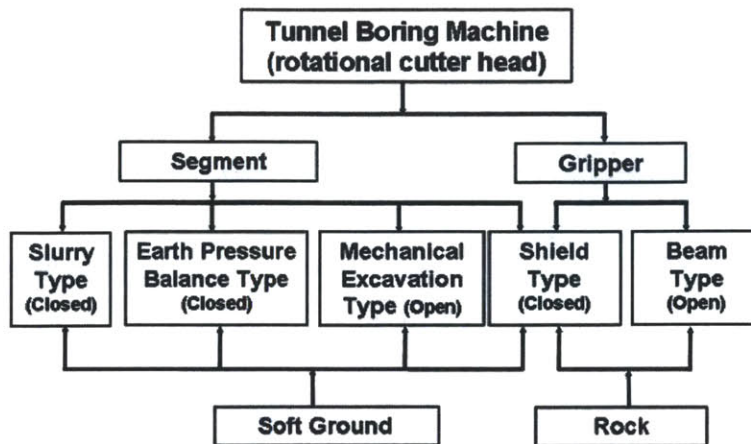


Figure 1.6 Types of TBMs (source: FHWA,2011)

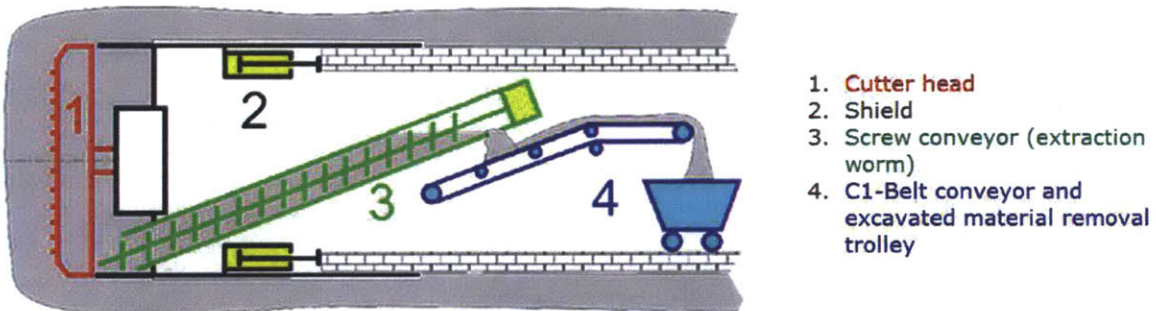


Figure 1.7 Excavation sequence for Earth Pressure balance (EPB) machine (source: NFM-Technologies)



Figure 1.8 Herrenknecht EPB machine used for Crossrail (London) (source: Crossrail Report, 2012)

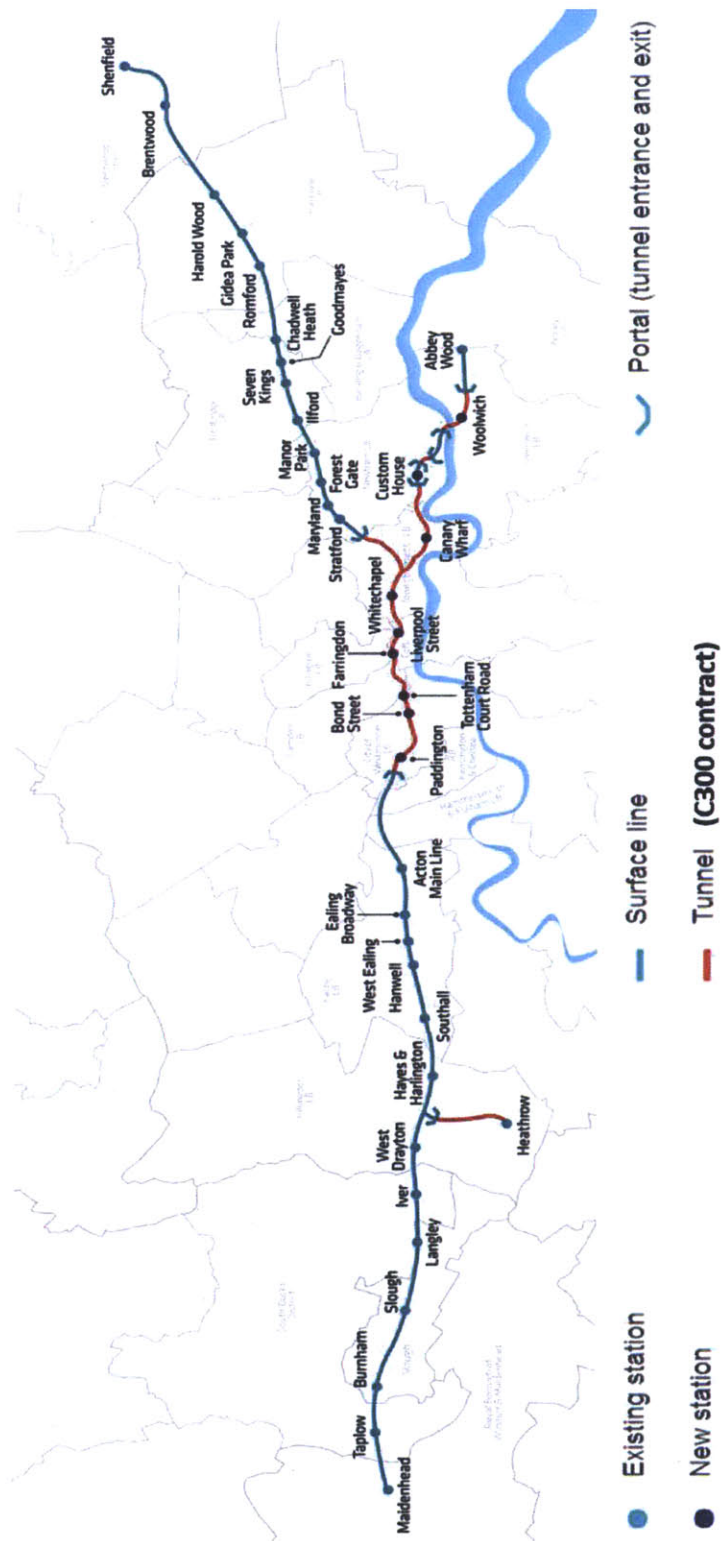
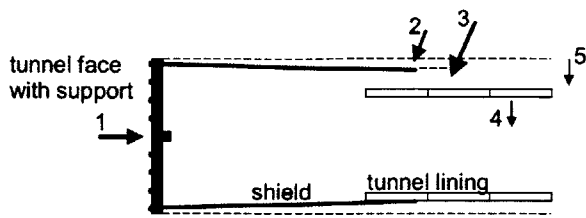
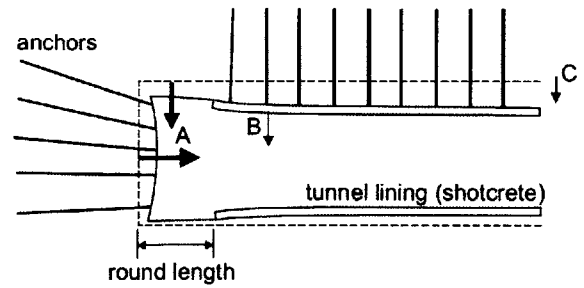


Figure 1.9. Regional map of Crossrail Project, new railway underneath central London (source Crossrail website : <http://www.crossrail.co.uk>)



1. Stress relief at excavation face
2. Overcutting, ploughing
3. Tail void
4. Lining deformation
5. Soil consolidation

a) Closed-face tunnel



- A. inward movement at the tunnel face
- B. Lining deformation
- C. Soil consolidation

b) Open-face tunnel

Figure 1.10 Sources of ground movements associated with tunneling (after Möller, 2006)



## **2 Background**

### **2.1 Introduction**

This chapter gives a brief review on different available bored tunnel construction methods used in practice and an overview of existing methods for predicting tunnel-induced ground movements.

### **2.2 Bored Tunneling methods**

Generally, bored tunnel construction methods can be classified into two main categories, open-faced and closed-face tunneling, depending on whether or not a continuous support system is used at the face of the excavation. This research focuses on soft ground tunneling using closed face tunnel methods, particularly the earth pressure balance control method (EPB). EPB tunneling method is suitable for soft ground conditions ranging from clayey to silty sand soils below the groundwater table (FHWA, 2011) and is currently be used for Crossrail tunnels (Figure 1.9).

#### **2.2.1 Conventional open-face tunneling**

Open face tunneling is usually preferred for firm ground<sup>1</sup> conditions where there is no need for continuous support at the face of the excavation, but can also be used for soft ground<sup>2</sup>

---

<sup>1</sup> Firm ground in tunneling refers to stable soils and rocks with no need of initial support

<sup>2</sup> Soft ground in tunneling refers to cohesive soils, cohesionless soils and silty sands with short stand-up time (time that the excavated face is stable) that usually require continuous support during excavation

conditions by applying extra supporting measures such as anchors, shotcrete etc. Nowadays, the method is widely used in urban areas even for soft ground tunneling, since the combined application jet grouting, anchors and nails, the pre-cutting technique has allowed the reinforcement and stabilization of the soil ahead of the excavation face, reducing significantly the surface displacements. An advantage of conventional tunneling methods is that they allow the construction of tunnels with non-circular cross-section or divided tunnel face. Usually a temporary lining is applied by sprayed concrete and then an extra layer of shotcrete is applied as a permanent lining structure (**Figure 2.1**). Conventional tunneling is more commonly referred to as the Sequential Excavation Method (STM) and includes the New Austrian Tunneling Method (NATM), a method that uses an observational approach to adjust the design based on observed displacements and ground conditions.

### **2.2.2 Open-face shield tunneling**

The main advantage of the open-face shield tunneling is that it provides radial support for the excavated tunnel cavity, while at the same time the tunnel face remains accessible. In this way the soil stratigraphy ahead of the tunnel can be observed directly, allowing for a quick adjustment of the excavation sequence when needed. Additionally an open face excavation can achieve tunneling through a variety of different ground conditions (soft grounds with boulders etc.) that would be almost impossible with a single closed face TBM (Maidl et.al, 1996). The excavation sequence for an open face shield tunnel is depicted in **Figure 2.2**. The steel shield (can be found in a range of cross-sectional shapes) advances into the soil with the help of hydraulic jacks that push against the permanent lining. The inner diameter of the shield has to

be bigger than the lining, as the lining is constructed inside the shield. In this way the construction process can be significantly faster as the lining is already in place to stabilize the excavated ground when the shield advances forward. In order to reduce the radial deformations due to the gap formed between the lining and the soil, grout is injected at the tail of the shield. The Jubilee Line Extension (JLE) Project is an example of a tunnel constructed using the opened-face shield tunneling method that generated unexpectedly large ground movements due in part to the unsupported heading (Standing and Burland, 2006).

### **2.2.3 Closed-face shield tunneling**

Closed face tunneling is an established and flexible technology for the construction of tunnels in urban areas. The method involves continuous support of the face of the excavation in order to minimize ground deformations in urban environments. There are many advantages that make closed shield face excavation so increasingly popular: it provides a safer working environment, faster construction, lower cost for long tunnels, improved continuous updating of the steering control parameters, capability for excavation beneath the water table etc. The closed excavation face usually consists of the cutting wheel of the tunnel boring machine (TBM) that provides a continuous support for unstable soils at the excavation face by mechanical support, compressed air, slurry pressure or earth pressure balance (**Figure 2.3**). Closed-face mechanized tunneling uses a cylindrical steel shield to carry the earth pressures and provide continuous radial support as the tunnel boring machine (TBM) advances forward. The TBM machine moves forward with the help hydraulic jacks that push against the already installed lining to slide the shield against the already excavated ground. As a result a gap is formed between the excavated

soil and the lining that is filled with grout to reduce the radial displacements of the surrounding soil. In order to avoid the flow of the grout inside the TBM a sealing between the shield and the last lining ring is applied (**Figure 2.4**). The available closed faced shield tunneling methods can be divided in five general categories: Blind shield, mechanized, slurry face machine and earth pressure balance machine (EPB) (FHWA, 2011). In the following chapter we will focus in the earth pressure balance method (EPB) that is the one that we consider for the 3-D model created for this study.

### **2.2.3.1 Earth pressure balance (EPB)**

The Earth pressure balance machine is suitable for tunneling in soft and unstable grounds, particularly below the groundwater table. A typical excavation procedure using an EPB (cf **Figure 1.7**) involves a face chamber that is filled with excavated debris that is then removed through a screw conveyor (with a controlled pressure from the head chamber) and deposited on the belt conveyor. Additives such as foam are injected into the head chamber to break up pieces of soil and ensure flowability through the screw conveyor. The rate that the screw conveyor extracts the soil from the chamber behind the cutting wheel and the pressure drop along the screw conveyor control mechanically the applied face pressure by matching the volume of the extracted soil with the volume of the soil displaced by the forward movement of the shield. Both the rate of the soil discharge and the pressure gradient are influenced by the rotational speed of the screw conveyor, the discharge outlet and the geometry of the screw conveyor. There are many theoretical models available describing the operation of a screw conveyor relating the operational parameters to the face pressure (Talmon and Bezuijen, 2002;

Merritt and Mair, 2008). As the machine advances forward, the permanent support is applied using precast segmental linings (**Figure 2.5**) consisting of curved precast concrete segments that are assembled inside the tail of the EPB machine to form a complete circular ring. The erected lining rings emerging from the tail of the shield behave as initial and permanent support at the same time allowing the construction of the tunnel in "one-pass". In this way continuous radial support is provided at the excavated sections as the EPB advances forward reducing the ground displacements and accelerating significantly the construction procedure. In order to reduce the displacements and the volume loss, grout is injected in the gap (tail void) formed between the excavated soil and the lining as the shield advances forward (**Figure 2.4**). The advance of the EPB is accomplished by hydraulic jacks that push against the last installed lining ring. The hydraulic jacks are controlled to steer the cutting wheel and shield along a pre-defined trajectory. In practice the steering control and distribution of weight within the shield can cause the machine to plough through the soil (i.e., the shield is no longer aligned with the trajectory of the cutting wheel).

### **2.3 Methods for predicting ground movements**

As the number and the complexity of urban tunnel projects increase, there is a pressing need for reliable methods that can accurately predict the ground movements induced by tunneling processes. Empirical data are available for a relatively small number of instrumented sites, and most available prediction methods focus on free field conditions where there are no interactions with overlying structures. The tunnel-induced movements in soft ground tunneling can be divided in two categories: 1) short-term deformations associated with tunnel

construction, and 2) long-term (post-construction) deformations associated with changes in ground stresses and pore water conditions (empirical and analytical solutions generally consider only the construction-related movements). One of the advantages of numerical methods is that by using appropriate soil models, it is possible to consider time dependent processes associated with consolidation and creep around the tunnel both during and after the construction. In principle the analyses can decouple sources of short-term and long-term deformations and estimate the time frame over which they occur. This research considers the short-term response and assumes undrained conditions in low permeability clay and hence, focuses on the effects of ground losses during construction. However it should be noted that the long term response of soil can be significant even years after construction. For example Mair (1999) reports unexpectedly large long-term movements for the JLE tunnels in St. James Park. This long-term response depends on various parameters such as soil properties (permeability and compressibility), boundary conditions (e.g. lining permeability), initial pore pressures, magnitude and distribution of generated pore pressures. On the other hand, the main sources of short term displacements are the stress changes around the tunnel face and the unsupported round length; insufficient grouting of the tail void, the radial ground movement due to overcutting etc. (as indicated in **Figure 1.10**).

### **2.3.1 Empirical methods for ground movements**

Empirical methods for tunnel-induced ground movements were first proposed by Peck (1969) and Schmidt (1969) and are still widely used in geotechnical practice. The following paragraphs survey the current state of empirical methods

### 2.3.1.1 Vertical surface displacements

Peck 1969 and Schmidt 1969 proposed a Gaussian function to describe the transversal surface settlement trough (Figure 2.6):

$$u_z(x, y) = u_z^0 \exp\left(-\frac{x^2}{2x_i^2}\right) \quad (2.1)$$

where

$x$  is the horizontal distance from tunnel centerline,

$u_z^0$  is the surface settlement at the tunnel centerline,

and  $x_i$  the location of the inflexion point in the settlement trough.

The volume of the surface settlement trough  $\Delta V_s$  per unit length of the tunnel can be found by integrating equation (2.1):

$$\Delta V_s = \sqrt{2\pi} u_z^0 x_i \quad (2.2)$$

The volume loss  $\Delta V_L$  in the region close to the tunnel is equal to:

$$\Delta V_L = \Delta V_s + \Delta V_g \quad (2.3)$$

where  $\Delta V_g$  is the volume change in ground.

For tunnel construction in drained conditions (i.e sands),  $\Delta V_L$  differs from  $\Delta V_s$  due to dilation or contraction in the soil mass ( $\Delta V_g \neq 0$ ). However for tunneling under undrained conditions  $\Delta V_g = 0$ , so  $\Delta V_L = \Delta V_s$ .

Mair and Taylor (1997) proposed a linear relationship between the location of the inflexion point  $x_i$  and tunnel depth  $H$ :

$$\frac{x_i}{H} = K \quad (2.4)$$

where  $K$  is the trough width parameter estimated using measured data from various tunnels all over the world. Mair and Taylor (1997) reported a mean value  $K=0.5$  for tunnels in clays and  $K=0.35$  for sands, **Figure 2.7**.

### **2.3.1.2 Horizontal surface displacements**

The most commonly used expression for estimating horizontal surface displacements was the one proposed by Attewell 1978 and O'Reilly & New 1982 and relates horizontal and vertical displacement components (based on a more limited dataset).

$$u_x \approx \frac{x}{H} u_z \quad (2.5)$$

This result (**Figure 2.8**) assumes that the vectors of the transverse surface displacements are directed to a point at or close to the center of the tunnel (**Figure 2.9**).

### **2.3.1.3 Subsurface displacements**

Mair and Taylor (1997) showed that the width of the subsurface settlement trough is also well correlated with the depth of the tunnel,  $H$ , and to characteristics of the overlying soil. The Gaussian trough extended by varying the trough width parameter:

$$x_i = K(H - z) \quad (2.6)$$



where  $K$  increases non-linearly with depth (**Figure 2.10**). For tunnels in clay Mair et. al (1993) proposed the following equation :

$$K = \frac{0.175 + 0.325 \left(1 - \frac{z}{H}\right)}{1 - \frac{z}{H}} \quad (2.7)$$

For tunnels in sand Jacobz (2002) proposed a modified equation:

$$K = \frac{0.09 + 0.26 \left(1 - \frac{z}{H}\right)}{1 - \frac{z}{H}} \quad (2.8)$$

#### 2.3.1.4 Longitudinal displacements

Attewell and Woodman (1982) proposed a method for estimating the longitudinal settlement trough. Following the assumption that the settlement trough can be described by a Gaussian function (2.1), they derived the longitudinal settlement trough as a superposition of the Gaussian settlement curves for infinite points along the tunnel axis. As a result the longitudinal settlement trough is given by the cumulative function of the Gaussian distributions:

$$u_z(y) = u_{z,max} \frac{1}{i\sqrt{2\pi}} \int_{-\infty}^y e^{-\frac{t^2}{2i^2}} dt \quad (2.9)$$

where  $y$  is the longitudinal location of the examined point relatively to the face of the excavation and  $u_z$  is the longitudinal settlement.

Several field studies were used to validate these results (Attewell and Woodman 1982). For open face tunneling the longitudinal displacement directly above the face of the excavation ( $y=0$ ) is half the maximum longitudinal displacement coinciding with the solution from (2.9)

equation (Attewell, 1986). However for closed face tunneling the longitudinal displacement for  $y=0$  is about  $0.25 \cdot u_{y,max}$ , significantly lower, so the empirical model has to be modified for this case (Mair and Taylor, 1997) (See **Figure 2.11**)

### **2.3.2 Analytical solutions for ground movements**

Analytical solutions have also been proposed for estimating tunnel-induced ground deformations. These solutions are based on simplifications of soil behavior (e.g., assuming soil is a linearly elastic material) but otherwise satisfy the principles of continuum mechanics. They use only a small number of input parameters that can be easily calibrated from field data and therefore offer a semi-empirical approach with greater predictive range than existing empirical methods. The analytical solutions also provide a useful tool for checking the accuracy of numerical solutions.

**Figure 2.12** shows the framework proposed by Sagaseta (1987) in which ground deformations around shallow tunnels are represented by the superposition of solutions of uniform convergence,  $u_e$ , and ovalization,  $u_\delta$ , deformation modes occurring at the tunnel cavity.

Pinto and Whittle (2013) compared closed-form solutions obtained by superposition for singularity solutions (after Sagaseta, 1987) with more 'exact' solutions obtained by representing the finite dimensions of a shallow tunnel in elastic soil (Verruijt, 1997). **Table 1** summarizes the analytical solutions proposed by Pinto and Whittle (2012) for describing the transverse field of ground deformations around a shallow tunnel based on displacement modes shown on **Figure 2.12a**. The solutions allow the estimation of both vertical and horizontal displacements at any

depth. The tunnel cavity deformation modes: uniform convergence  $u_\varepsilon$ , ovalization  $u_\delta$  are used as input parameters, while the vertical translation  $\Delta u_z$  is calculated to satisfy the boundary condition of zero vertical displacements at the far-field. **Figure 2.12b** presents separately the settlement trough induced only by uniform convergence,  $u_\varepsilon$ , and the one induced by ovalization,  $u_\delta$ , as well as their combination. **Figure 2.13** depicts the effect of the relative distortion,  $\rho = -\frac{u_\delta}{u_\varepsilon}$  on the estimated settlement troughs.

Pinto et al. (2013) found a good agreement between the approximate analytical solutions and measured data from tunnels excavated through different ground conditions using a variety of closed and open-face construction methods. However, they noted significant discrepancies between predicted and measured settlements for the case of the Heathrow Express trial tunnel (Deane & Bassett, 1995) that were attributed to anisotropic stiffness properties of the heavily overconsolidated London Clay. Zymnis et al. (2013) extended the analytical solutions to account for cross-anisotropic behavior of clay and used these results to interpret ground movements for open face construction of the Jubilee Line Extension (JLE) tunnels in St. James Park. **Figure 2.13** compares the displacement components computed with the analytical solutions for isotropic and cross-anisotropic soil properties to measured data from the WB JLE tunnel. Apparently, there is a good agreement between the predicted surface displacements using the analytical solutions and the real data.

### 2.3.3 Numerical simulations of tunnel construction

Although, empirical and analytical methods are still a valuable tool for design, mainly due to the simplicity and the experience they reflect, numerical simulations are becoming increasingly

popular as the computational time for 3D models decreases making it practical to simulate details of the construction. Numerical simulations also allow for the use of complex constitutive models, calibrated appropriately for the specific soil behavior for different tunnel projects, and offer the possibility to model coupled flow and deformation in the surrounding soil.

Current engineering practice uses 2D simulations for tunnel construction in order to estimate ground displacements. However it is well known that the solutions are strongly dependent on the constitutive soil model. Sophisticated soil models are needed in order to achieve realistic predictions of the settlement troughs, especially in heavily overconsolidated clays (Mair et al., 1981). Another drawback of the 2D models is that they don't represent details of the tunneling procedure (e.g. Clough and Leca, 1989), especially for closed face tunneling. Therefore, 3-D models are needed to model construction process parameters (such as the advance rate, grout, face pressure etc.). Although, finite element methods have been used to simulate tunnel construction since the early 1980s, there are still relatively few studies involving three-dimensional modeling of mechanized tunneling (e.g. Swoboda and Abu-Krishna, 1999) compared to conventional tunneling (i.e., open-face, sequential excavation and support) mainly due to the computational complexity associated with the simulation of a TBM, as well as the uncertainty associated with all the construction parameters i.e face pressure, injected grout pressure, over-excavation etc . The 3D models simulating the soft ground<sup>3</sup> tunneling construction process in steps that take into account the disturbance of the in situ stress state of the soil and pore pressures due to the heading face support, radial ground movement due to overcutting, the

---

<sup>3</sup> Soft ground in tunneling refers to cohesive soils, cohesionless soils and silty sands with short stand-up time ( time that the excavated face is stable) that usually require continuous support during excavation

consolidation of the surrounding soil and the tail void grouting (see **Figure 1.10**) in order to estimate accurately the ground displacement.

### **2.3.3.1 Examples of Finite Element modeling approaches**

Möller (2006) compared 2D to 3D simulations using the general purpose geotechnical software Plaxis in order to highlight the different simulation approaches. For simulating conventional tunneling using a 2D model, Möller (2006) uses the stress reduction method, often referred to as the  $\beta$ -method or  $\lambda$ -method (**Figure 2.15**), which assumes that the initial geostatic stresses at the tunnel cavity  $p_0$  are reduced to  $\beta \cdot p_0$ , where  $\beta$  is an unloading factor ranging from 0 to 1 (a typical value for  $\beta \approx 0.4-0.6$ ). Möller, (2006) used step-by-step methods to simulate in 3D the excavation procedures for open-face NATM tunnels (**Figure 2.16**) and closed-face shield tunnels (**Figure 2.20**). As illustrated in **Figure 2.16**, the NATM procedure is simulated in steps. After the initial geostatic stress condition is generated, at each step one soil element is removed, simulating the unsupported excavation sequence. Each soil element has a circular cross-section and standard width that corresponds to the selected round length for the tunnel. So at each step  $i$ , the soil element  $i$  is deactivated and the lining element  $i-1$  is activated to provide support to the soil slice excavated in the previous step. The simulation continues until steady solutions are achieved (e.g. the surface displacement above the centerline converges to a constant value,  $u_{y,max}$ , **Figure 2.11**).

In order to gain insight on the influence of the earth pressure coefficient  $K_o$  on the surface settlements, Möller (2006) compared simple 2D and 3D analyses (**Figure 2.17**) for conventional

tunneling. The non-linear elasto-plastic Hardening soil (HS) model<sup>4</sup> was used. **Figure 2.18** compares the computed surface settlements troughs for selected values of  $K_0$ . The 3D analyses were conducted using the step-by-step method illustrated in **Figure 2.16**, while the 2D analyses were carried out using an appropriate unloading factor  $\beta$  to achieve matching of the centerline settlements between 2D and 3D analyses. It is quite interesting that for  $K_0 \geq 1.5$ , heave is observed at the surface above the tunnel centerline.

For simulating shield tunneling using a 2D model, Möller (2006) suggested the grout pressure method, which assumes that tunnel lining is surrounded by a thin grout layer with a known grout pressure  $\sigma_g$  (**Figure 2.19**). During excavation, the initial tunnel interface stresses  $\sigma_0$  are reduced to  $\sigma_g$  by a pseudo-time parameter  $\lambda$  that increases from 0 to 1:

$$\sigma = (1 - \lambda) \cdot \sigma_0 + \lambda \cdot \sigma_g \quad (2.10)$$

For simulating slurry shield tunneling in 3D, a step-by-step pressure method is used, presented in **Figure 2.20**. High magnitude axial pressure is used to simulate the slurry pressure at the face of the tunnel, while lower magnitude radial pressure is applied to simulate the shield and the fresh grout pressure in the tail void. So instead of representing the actual shield using stiff shell elements, a pressure boundary condition is used to simulate the support effect. All the prescribed pressures increase hydrostatically with depth. The grout pressure is radially applied to the excavated soil surface for two rings behind the shield, while the soil is allowed to freely deform until it comes into contact with the lining (representing the formed tail void). For the

---

<sup>4</sup> Hardening Soil model is an advanced soil model (compared to simple elasto-plastic models like Mohr-Coulomb) that describes pre-failure states of soil behavior and the soil stiffness is stress dependent.

subsequent steps, solid elements representing the hardened grout are activated and the radial pressure is switched off. Möller (2006) suggests that a similar sequence can be applied also for the for the EPB tunneling method, with the use of a modified pressure boundary (debatable) or a contraction boundary (better) to simulate the overcutting and the conical shape of the EPB shield.

$\text{Convergence: } \begin{cases} u_x^c = 4 \cdot u_\epsilon \cdot R \cdot \left\{ \frac{(1-\nu) \cdot x}{x^2 + (y-H)^2} - \frac{(y-H) \cdot x \cdot y}{[x^2 + (y-H)^2]^2} \right\} \\ u_z^c = 2 \cdot u_\epsilon \cdot R \cdot \left\{ \frac{2 \cdot (y-H) \cdot x^2 + H \cdot [x^2 - (y-H)^2]}{[x^2 + (y-H)^2]^2} - \frac{2 \cdot (1-\nu) \cdot (y-H)}{x^2 + (y-H)^2} \right\} \end{cases}$
$\text{Ovalization: } \begin{cases} u_x^c = \frac{8 \cdot u_\delta \cdot R}{3-4 \cdot \nu} \cdot \left\{ \begin{aligned} & x \cdot \frac{x^2 + y^2 - H^2}{[x^2 + (y-H)^2]^2} \cdot (1-\nu) - \dots \\ & \dots - x \cdot y \cdot \frac{y \cdot (x^2 + y^2) + 2 \cdot H \cdot (H^2 - x^2) - 3 \cdot y \cdot H^2}{[x^2 + (y-H)^2]^3} \end{aligned} \right\} \\ u_z^c = \frac{8 \cdot u_\delta \cdot R}{3-4 \cdot \nu} \cdot \left\{ \begin{aligned} & \frac{x^2 \cdot (2 \cdot H - y) - y \cdot (y-H)^2}{[x^2 + (y-H)^2]^2} \cdot (1-\nu) - \dots \\ & \dots - \frac{(y-H) \cdot \{ H \cdot y \cdot (y-H)^2 - x^2 \cdot [(x^2 + y^2) + H \cdot (y+H)] \}}{[x^2 + (y-H)^2]^3} \end{aligned} \right\} \end{cases}$
$\text{Ovalization: } \frac{\Delta u_z}{u_\delta} = \frac{2}{3-4 \cdot \nu} \cdot \frac{R}{H} \cdot \frac{(1-8 \cdot \nu) \cdot \left(\frac{R}{H}\right)^4 + (11-8 \cdot \nu) \cdot 4 \cdot \left(\frac{R}{H}\right)^2 - 32}{\left[4 + \left(\frac{R}{H}\right)^2\right]^3}$
$\text{Convergence: } \frac{\Delta u_z}{u_\epsilon} = 4 \cdot \frac{R}{H} \cdot \frac{8 \cdot (1-\nu) - (1-2 \cdot \nu) \cdot \left(\frac{R}{H}\right)^2}{\left[4 + \left(\frac{R}{H}\right)^2\right]^2}$

**Table 2.1 Analytical solutions for ground deformations around a shallow tunnel (Pinto and Whittle, 2011)**



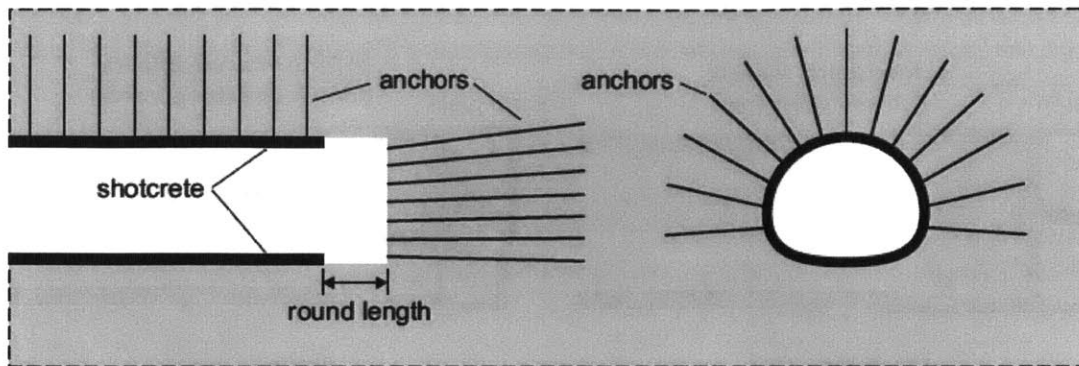


Figure 2.1 Support elements for sequential excavation, NATM method ( Moller,2006)

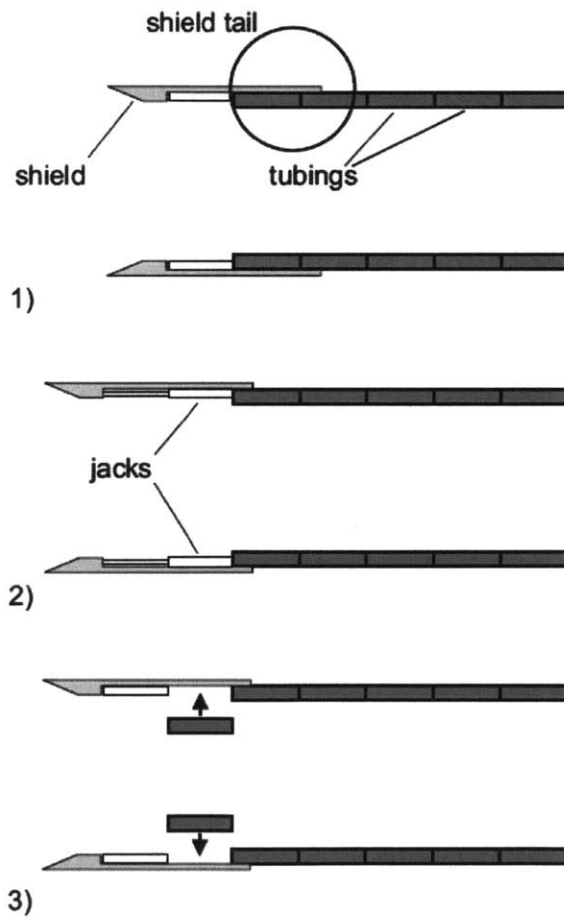


Figure 2.2 Excavation sequence for open face shield tunneling ( Moller, 2006)

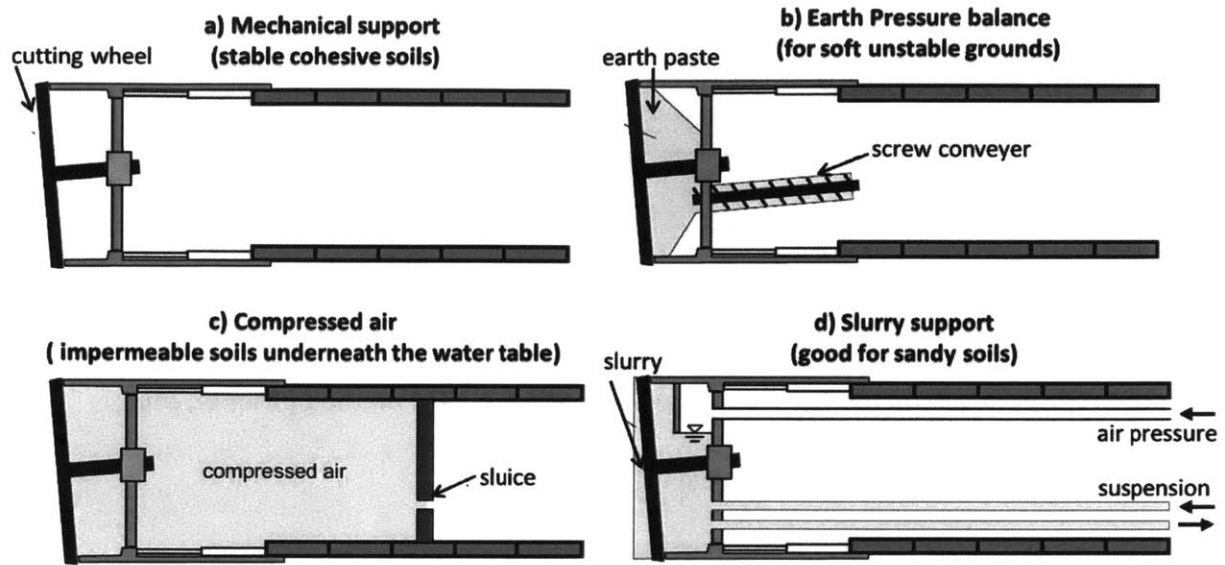


Figure 2.3 Closed face shield tunneling methods ( Moller, 2006)

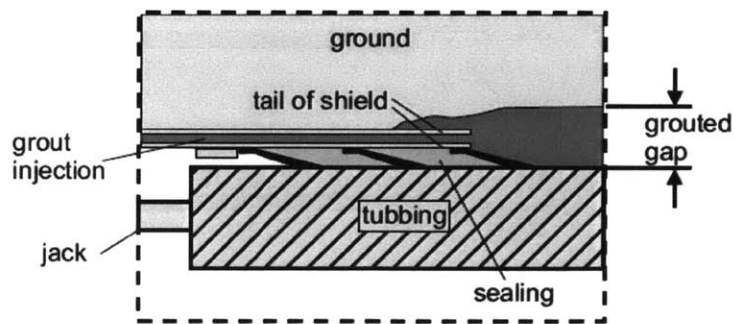


Figure 2.4 Schematic figure of grout injection in the tail void ( Moller, 2006)

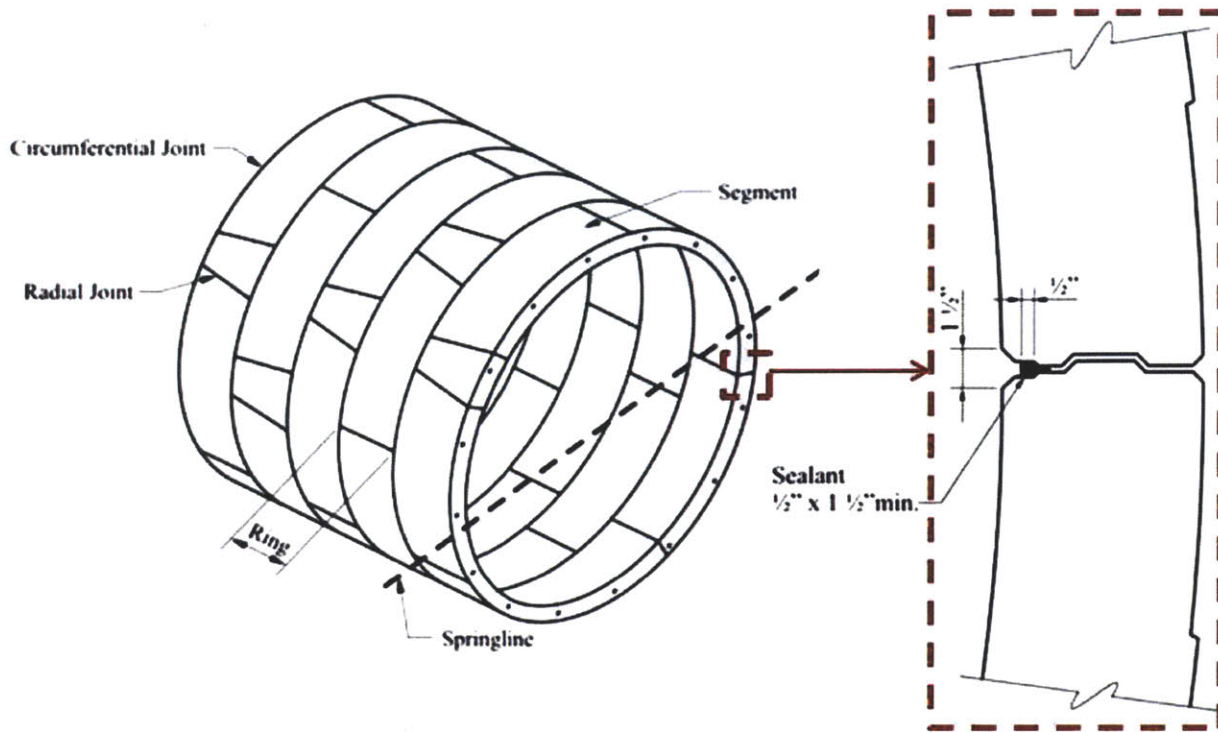


Figure 2.5 Schematic figure of the assembled precast segmental lining (source: FHWA,2011)

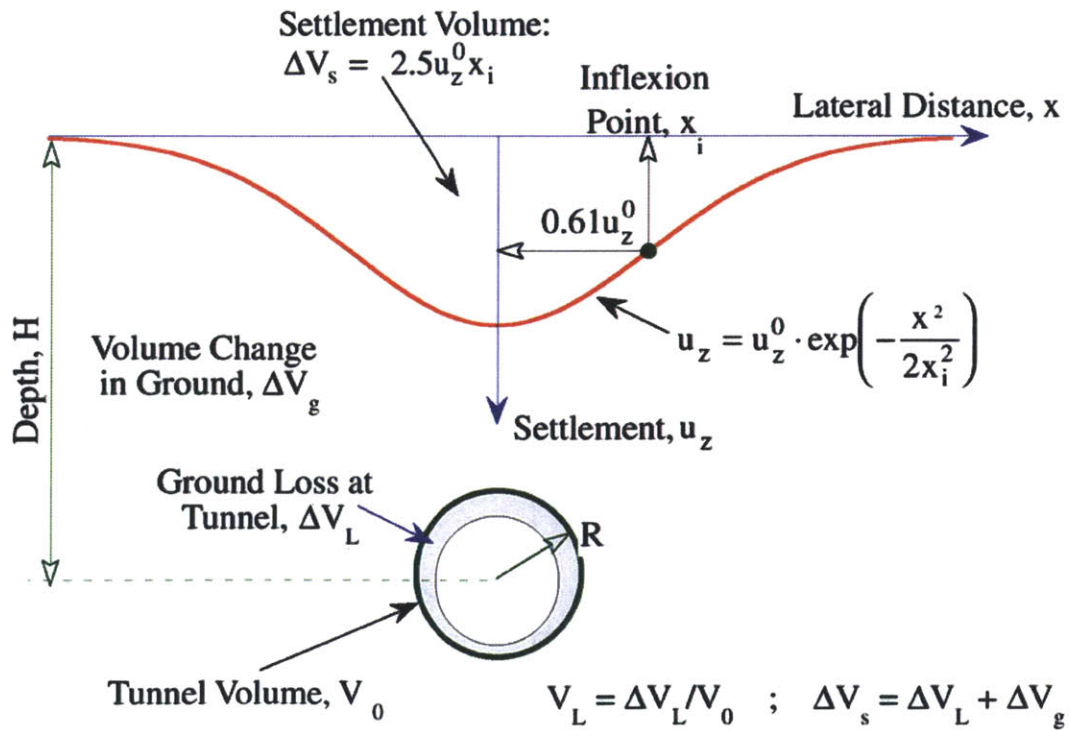


Figure 2.6 Empirical function for transversal settlement trough

(after Peck, 1969 and Schmidt 1969)

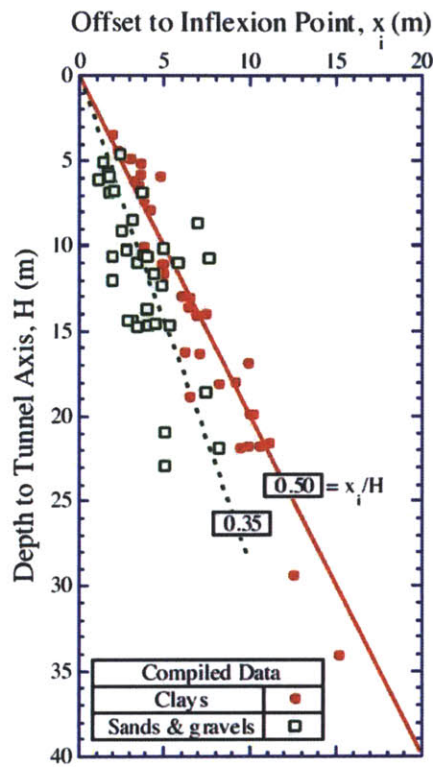


Figure 2.7 Empirical estimation of inflexion point ( after Mair and Taylor, 1997)

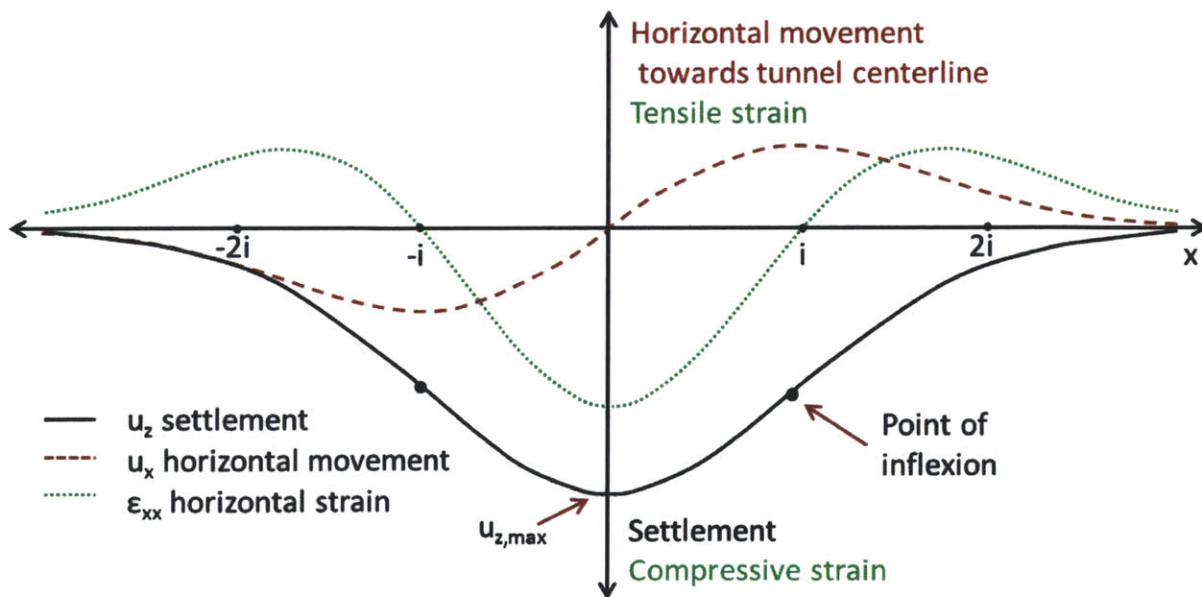


Figure 2.8 Horizontal ground movement and strain (Mair et.al 1996)

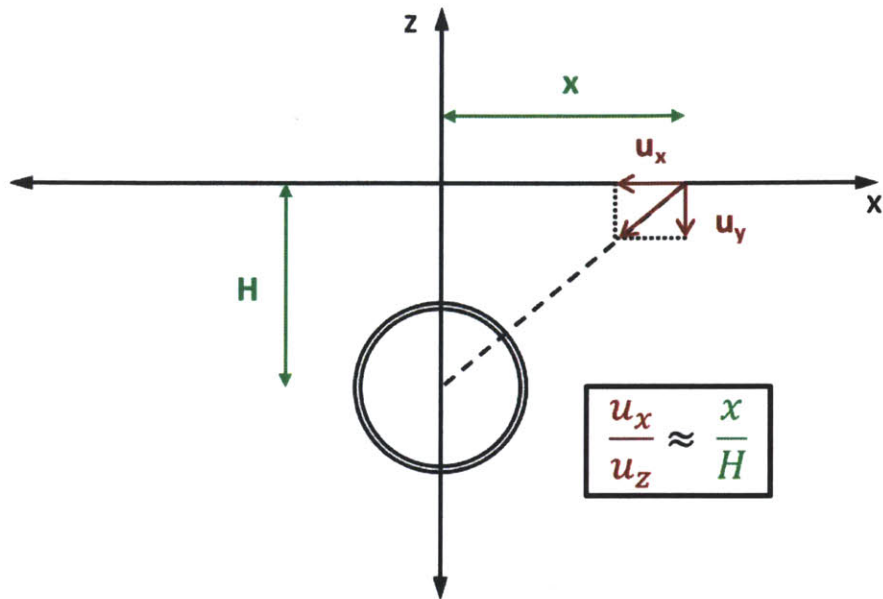


Figure 2.9 Under the assumption of equation (2.5) the vectors of the transverse surface displacements are directed to the center of the tunnel.

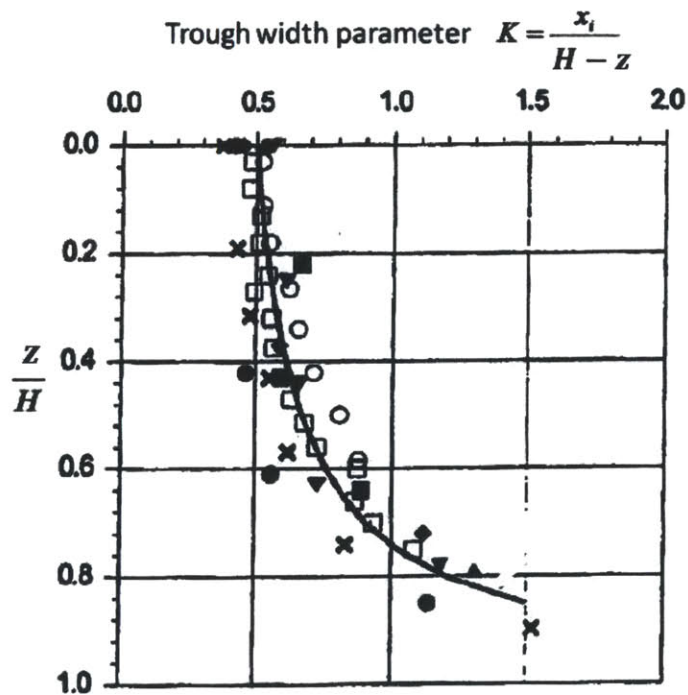


Figure 2.10 Variation of trough width parameter  $K$  with normalized depth ( $y/H$ ) for tunnels in clay (Mair et.al, 1993)

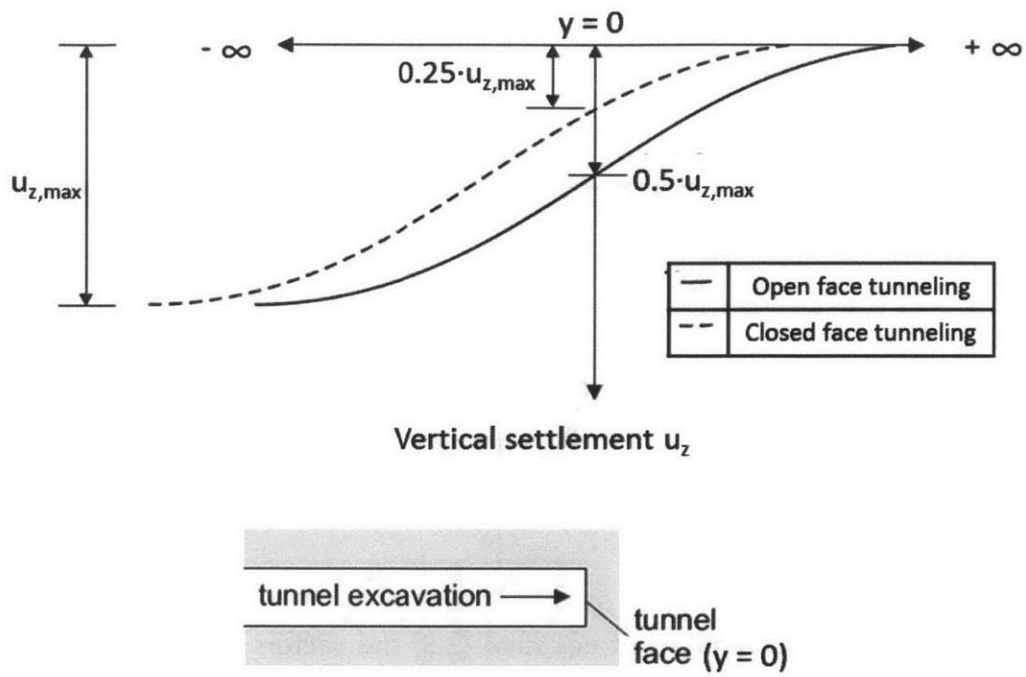
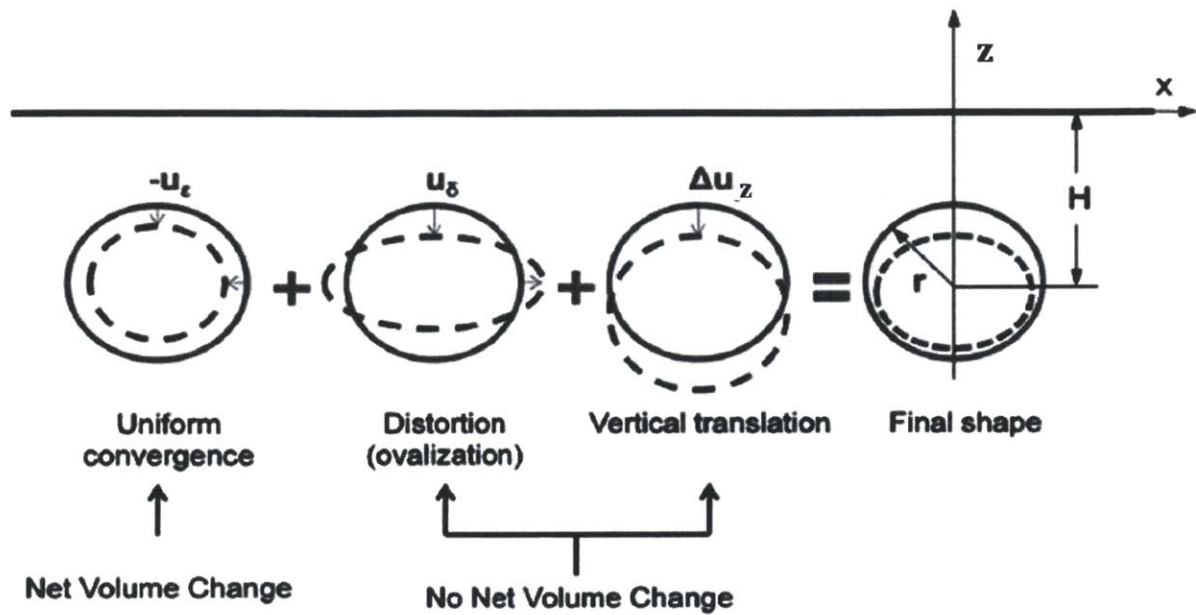
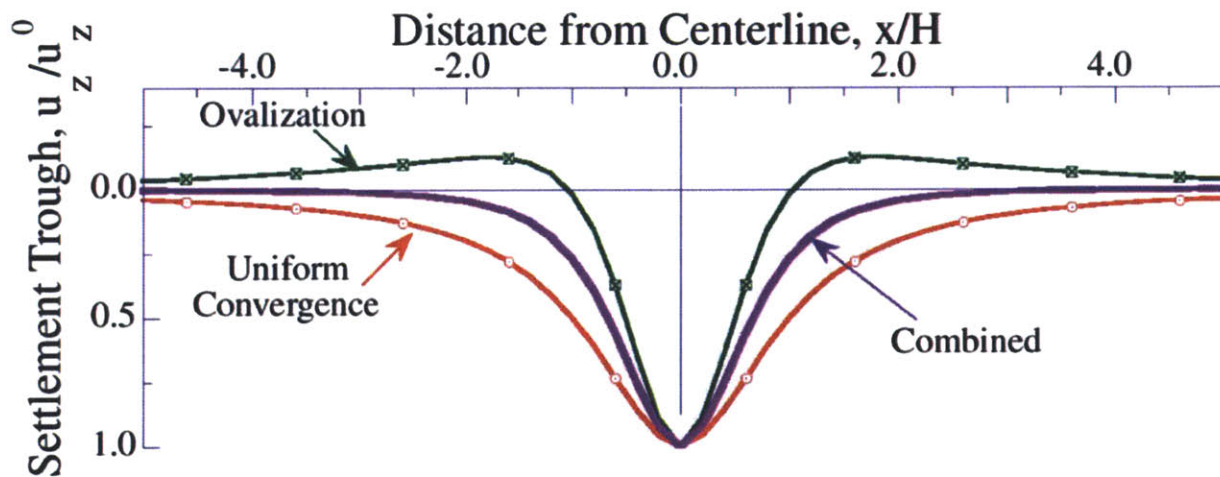


Figure 2.11 Longitudinal surface displacement above tunnel centerline (after Attewell et.al 1986)



(a) Notation and sign convention



(b) Component contributions to surface settlement trough

Figure 2.12 Deformation modes around tunnel cavity  
(source Whittle and Sagaseta, 2003, Pinto and Whittle, 2013)



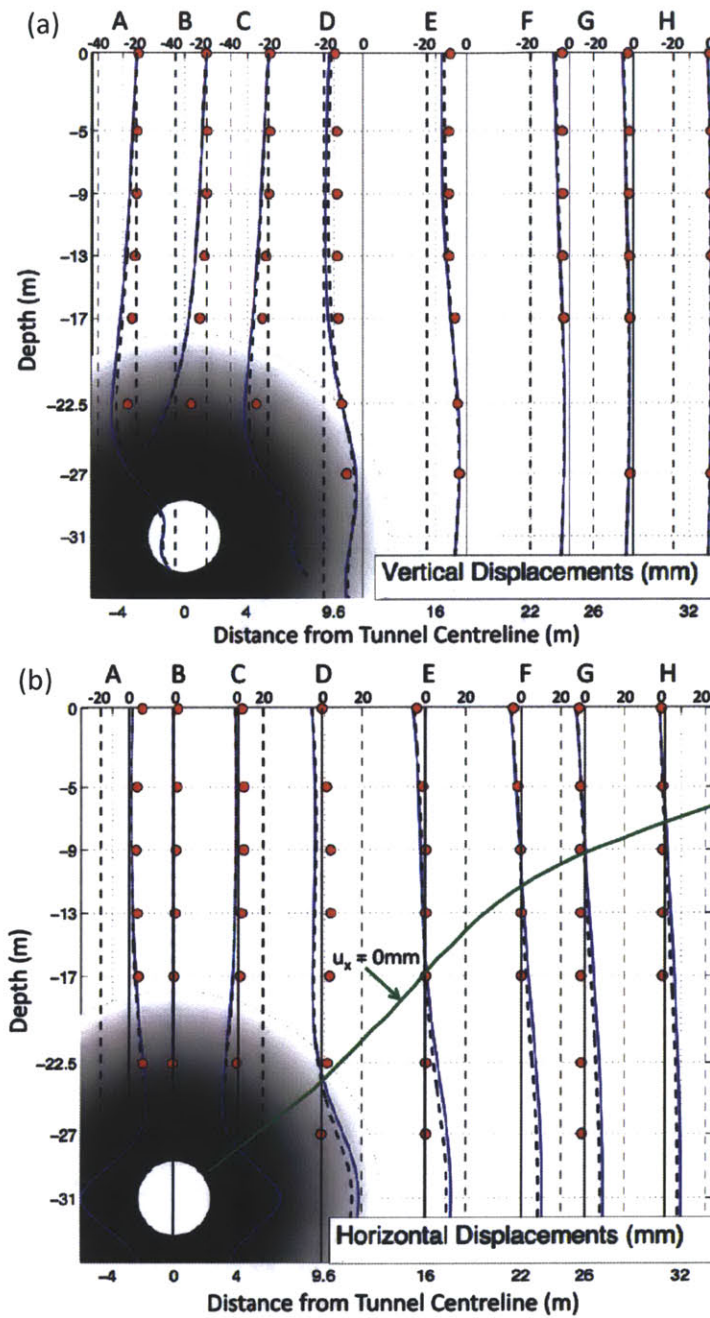


Figure 2.13 Comparison of computed and measured subsurface ground movements for WB JLE tunnel: (a) vertical displacements; (b) horizontal displacements (Zymnis et.al, 2013)



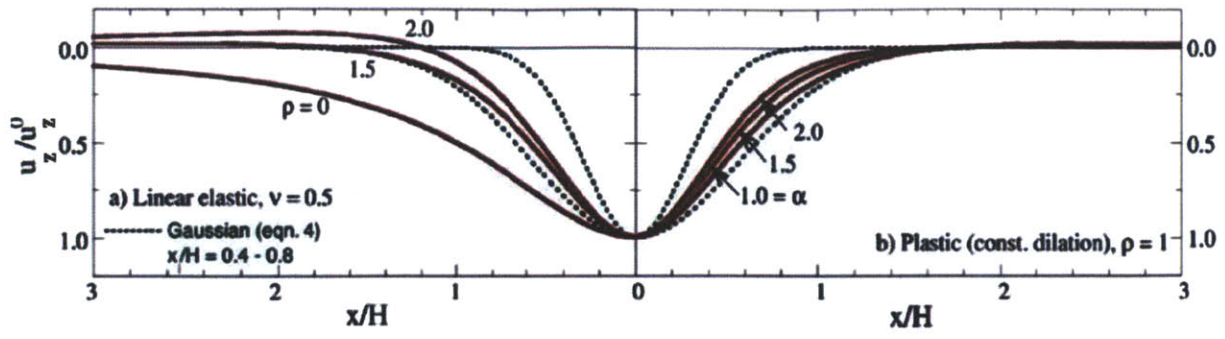


Figure 2.14 Effect of input parameters on surface settlement distribution ( Whittle and Sagaseta, 2003)

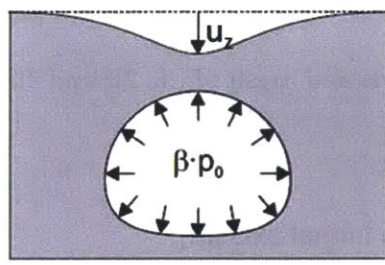


Figure 2.15 Stress reduction method ( Möller, 2006)

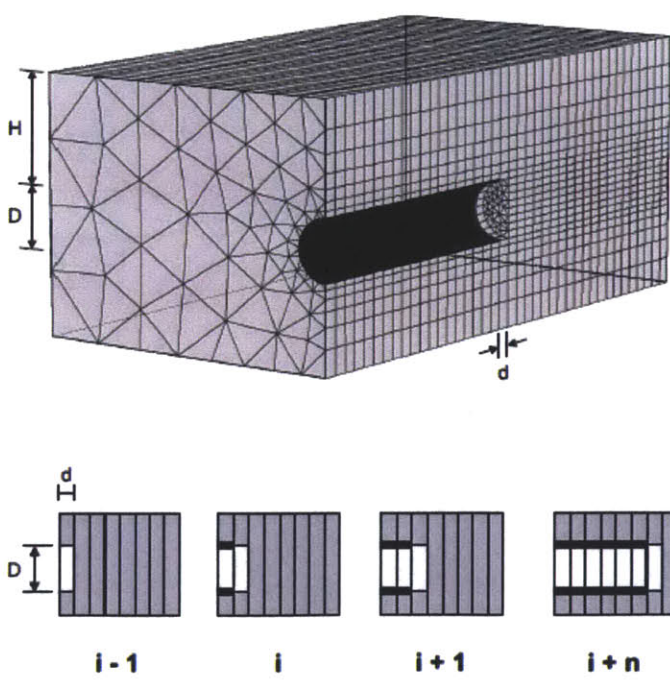


Figure 2.16 Step-by-step simulating of open face, NATM tunneling ( Möller, 2006)

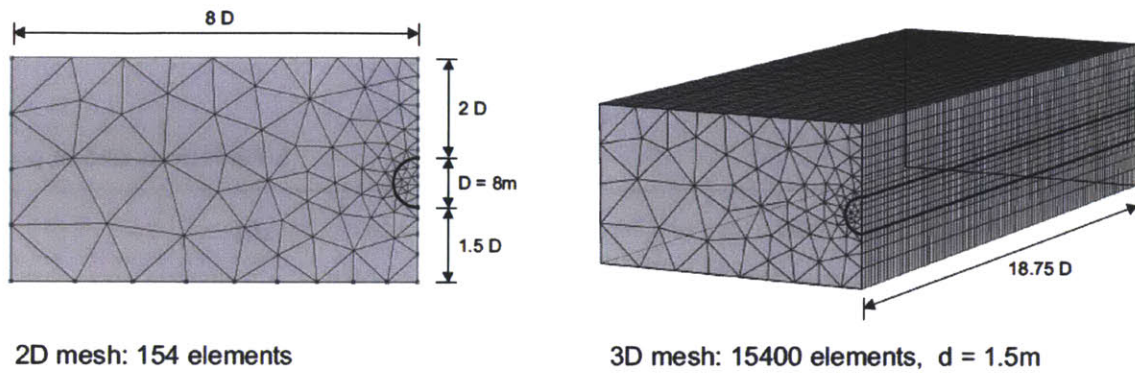


Figure 2.17 Dimensions and mesh of the 2D and 3D models ( Möller, 2006)

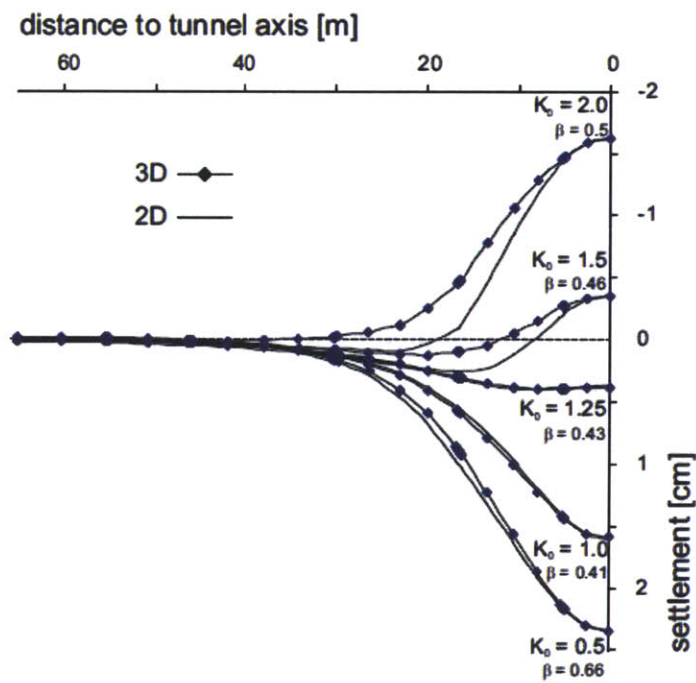


Figure 2.18 Transverse settlement troughs for 3D and 2D analyses for different  $K_0$  values ( Möller, 2006)

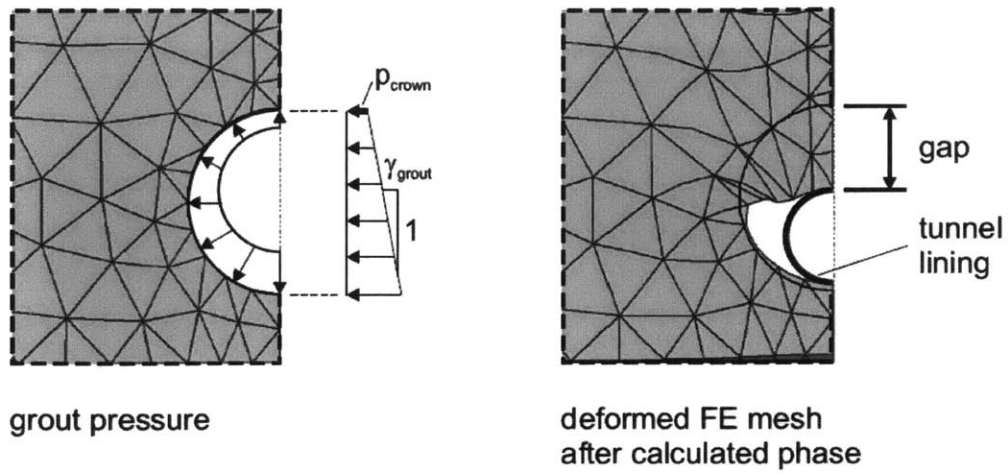


Figure 2.19 Display of grout pressure method (Möller, 2006)

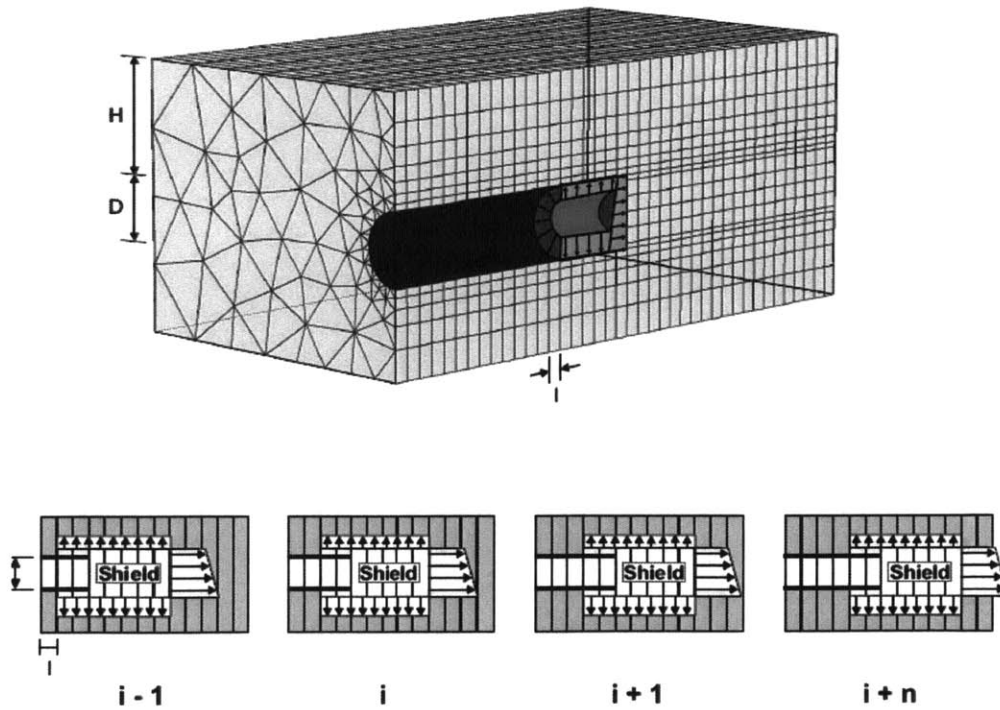


Figure 2.20 Step-by-step simulating of closed face, shield tunneling (Möller, 2006)



## 3 Development and Validation of FE Model for Tunneling

### 3.1 Introduction

This chapter describes the development and validation of numerical models for describing ground movements caused by tunneling in low permeability clay. The analyses consider short-term undrained deformations due to tunnel construction but do not address longer term movements due to consolidation or creep. Sections 3.2 and 3.3 evaluate 2D methods of analysis that are routinely used to describe the transverse settlement trough, while section 3.4 describes 3D simulations of the advancing tunnel heading.

### 3.2 Evaluation of 2D numerical solutions

The first stage in this study was to compare and validate 2D finite element numerical predictions with available analytical solutions for ground deformation around a shallow tunnel cavity, ensuring accurate representation of far field ground movements. The analytical solutions relate ground deformations to three displacement modes at the tunnel cavity: uniform convergence  $u_e$ , ovalization  $u_\delta$  and uniform vertical translation  $\Delta u_z$  (cf., **Figure 2.12**). The tunnel excavation is represented by applying a set of prescribed deformations around the tunnel cavity to emulate analytical solutions (**Table 2.1**) for uniform convergence and ovalization modes (the development of these solutions for linear isotropic soil is fully documented in Pinto & Whittle 2013). This validation exercise (Javascript code is given in Appendix C) aims to compute the

displacements given by the analytical solutions and proved useful in defining key parameters including model dimensions and mesh density.

The simulations consider a 3.5 m radius tunnel to located at a depth  $H=16$  m (i.e.  $R/H=0.22$ )<sup>5</sup> in a deep clay layer. Initially the ground is modeled as an isotropic, linearly-elastic material with constant Young's modulus,  $E = 120$  GPa and Poisson's ratio  $\nu' = 0.25$  (drained case) and ( $\nu_u = 0.49$  ; undrained case). The analyses compare the effect of soil weight on the computed settlement trough.

**Figure 3.1** shows the half-section 2D finite element model. The geometry of the initial 2D model was extended to a depth of 300 m and laterally to a distance  $x=300$  m ( $x/H =19$ ) in order to emulate the infinite half-space assumptions. The model assumes no lateral displacements along the vertical boundaries of the model, and zero displacements at the base boundary. The soil mass is represented by 15-noded solid triangular elements (cubic strain elements, Sloan and Randolph, 1982) with fourth order interpolation of displacements, **Figure 3.2**.

The tunnel excavation is represented by applying a typical set of prescribed deformations  $u_e$  and  $u_o$  around the tunnel cavity to emulate analytical solutions for uniform convergence and ovalization modes. The analytical solutions were used to validate the numerical results. **Figure 3.3** shows a perfect match was achieved between the resulting ground surface deformations and the analytical solutions, for both the drained ( $\nu = 0.25$ ) and the undrained case ( $\nu = 0.49$ ).

---

<sup>5</sup> These parameters emulate initial phases of the tunnel bore for the Crossrail project (West of Paddington Station in London)

### 3.3 Comparison with conventional stress reduction method

The 2D finite element model was modified to simulate the excavation procedure by using conventional stress reduction method (**Figure 2.15**), often referred to as the  $\beta$ -method or  $\lambda$ -method. The method reduces the initial geostatic stresses inside the tunnel cavity ( $p_0$ ) by a reduction factor  $\beta$  ranging from 0 to 1. The case,  $\beta=0$  corresponds to the unlined tunnel case (i.e full stress release in the tunnel cavity) while  $\beta=1$  corresponds to the initial condition (no stress release in the tunnel cavity).

For the initial 2D simulations the ground is modeled as an isotropic, linearly-elastic material with constant Young's modulus,  $E = 120 \text{ GPa}$ , Poisson's ratio  $\nu_u = 0.49$  (undrained case, unit weight  $\gamma=20 \text{ kN/m}^3$  and earth pressure coefficient  $K_0 = 1.0$ ). The computed results using the stress reduction method ( $\beta$ -method) for  $\beta=0$  were compared to the analytical solutions. The computed tunnel cavity deformations (for  $\beta=0$ ) were fitted by  $u_\epsilon$  and  $u_\delta$  mode shape parameters using the least square method ( see Appendix B). However, the analytical solutions couldn't reproduce the computed settlement trough as shown in **Figure 3.4**. The mismatch between the analytical solutions and the numerical simulation can be explained by the buoyancy effect (see **Figure 3.5**) associated with deactivation of the soil volume. If we uncouple the weight relief and the volume loss, then the analytical solutions can accurately predict the settlement trough induced by the volume loss (**Figure 3.6**).

Then 2D simulations using the stress reduction method ( $\beta$ -method) were conducted for various  $\beta$  values. The analyses took into consideration both linear-elastic and elasto-plastic soil models (M-C). The selected input soil parameters are presented in **Table 3.1** and are based on the

strength and stiffness soil profiles recommended for London clay and consider a 60 m deep clay profile.

**Figure 3.7** compares the components of surface displacements (using the stress reduction method for  $\beta=0$ ) for each of the three soil profiles (upper bound, design and lower bound, see **Table 3.1**) for both elastic and elastoplastic (M-C) cases. As expected, the upper bound (the stiffer soil profile) produces the smallest surface displacements. There are large effects of soil plasticity particularly for the design profile, and the unsupported tunnel is unstable for the lower bound elastoplastic case. **Figure 3.8** shows the plastic yield zones for the three profiles. The lower bound profile generates a failure mechanism with the plastic zone extending to the ground surface.

**Figure 3.9** compares results of surface deformations for the “design line” soil profile for different  $\beta$  varying between 0 and 0.5. The results show decrease in the movements with  $\beta$  increasing. That’s a reasonable result as for smaller applied stresses (i.e. smaller  $\beta$ ) at the boundary of the tunnel cavity, the soil displacements will be larger. In the same manner, as the  $\beta$ - value decreases, the thickness of the plastic zone becomes larger (**Figure 3.10**).

### **3.4 3D model of Unlined Tunnel**

This section describes the development and validation of a simple 3-D finite element model for simulating an unsupported/unlined tunnel construction. The numerical results of the 3D model are compared with the 2D unlined case described in section 3.3 (i.e, full stress release at the tunnel cavity). This simple 3D finite element model was created to validate that the locations of



lateral boundaries and the mesh density were capable of numerically accurate calculations of soil deformations.

Simulation of unlined tunnel construction requires full stress release inside the tunnel cavity (i.e. stress free tunnel cavity). The analyses use an elastoplastic soil model (i.e., Mohr-Coulomb). The selected soil parameters, presented in **Table 3.2**, correspond to the selected design cross-section (**Figure 4.1**) and will be explained in the following paragraph.

The analyses consider an idealized 100m long straight horizontal tunnel within a uniform 60 m deep clay layer (**Figure 3.12**). The FE model assumes a lateral boundary located 300 m from the tunnel centerline (to ensure accurate representation of far field ground movements), with symmetry in the longitudinal plane such that only a half-section of the tunnel (and EPB machine) is represented. The model assumes no lateral displacements along the exterior vertical boundaries of the mesh. This simple model considers the advance of an unsupported tunnel excavation (i.e., full release of initial stresses at the tunnel cavity) with  $K_0 = 1.0$  and is represented by 66 steps with each step representing the removal of a 1.5m round length of soil excavation (**Figure 3.13**).

The clay is modeled as an elastic-perfectly plastic material model (referred to as Mohr-Coulomb; MC) that is subject to undrained shearing (i.e., the model assumes there is no migration of pore water within the clay mass over the time frame of the tunnel construction). **Table 3.2** lists the input parameters used to represent the London Clay profile using the MC model. The analyses assume that the groundwater table is coincident with the ground surface and pore pressures are hydrostatic. **Figure 3.12** shows the finite element mesh developed using

Plaxis 3D. The soil mass is represented by 10-noded solid tetrahedral elements with quadratic interpolation of displacements, while the tunnel lining is simulated using 6-noded plate elements (Figure 3.11a and b).

### 3.4.1 Comparison of Plaxis 2D with Plaxis 3D for the unlined case

Figure 3.15 summarizes the components of ground surface deformations (vertical,  $u_z$  and transverse,  $u_x$ ) computed at the central plane of the 3D FE model three reference locations of the excavation face,  $y'/D = 7.1, 0.7$  and  $-6.8$  (where  $y'$  is the longitudinal distance from the center of the FE model and  $D$  the nominal lining diameter).

As shown in Figure 3.14, for the first location the excavation face is close to the front face of the FE model, for the second location the face approaches the central-plane of the model, while for the third the face approaches the rear face of the model. It should be noted that, when the tunnel excavation has progressed far beyond the central section of the model (i.e.,  $y'/D = -6.8$ ), the deformations at the central plane match exactly the results from 2D simulations.

The results show that most of the ground deformations occur once the excavation has progressed past the central plane (i.e., between  $y'/D = 0.7$  to  $-6.8$ ; Figure 3.15a, b). The settlement and transverse deformation mode shapes ( $u_z/u_{zmax}$ ,  $u_x/u_{xmax}$ ; Figure 3.15 c, d) vary significantly with the location of the excavated face. Initially, there is a small heave near to the centerline of the tunnel ( $y'/D = 7.1$ ) associated with the buoyancy of the excavated cavity resulting in a maximum settlement at an offset location ( $x \approx 40$  m).

**Figure 3.16** compares the vertical displacements at the centerline of the tunnel as a function of the longitudinal position of the excavation face to the empirical method proposed by Attewell and Woodman, 1982 (described in section 2.3.1.4) for estimating longitudinal settlements (with  $K=0.5$  for clay). The empirical method gives a pretty good prediction of the computed settlements. The computed settlement for  $y=0$  is less than  $0.5u_{y,max}$ , so the computed trough appears to be slightly shifted compared to the empirical solution.

**Figure 3.17** illustrates the yield zone around the tunnel. The plastic deformations occur locally around the tunnel cavity (the thickness of the plastic zone is about 2.5 m) and it extends up to 50m behind the face of the excavation. As we already mentioned in section 3.3, for unlined tunnels (i.e. full stress release at the tunnel cavity) the plastic zone is interrelated with the observed displacements. This observation is supported by the fact that large displacements start to develop only after the face of the excavation reaches the examined middle cross-section ( $y'/D < 0.7$ ), which coincides with the propagation of the yield zone up to the examined cross-section.

Reference Properties – MC Model			
Total unit weight, $\gamma$ kN/m <sup>3</sup>	20.0		
Young's modulus E' MPa	Upper Bound	Design Line	Lower Bound
	20+2.0z	15+1.1z	8+0.7z
Undrained shear strength*, $s_u$ kPa	100+10z	75+5.5z	40+3.5z
Poisson's Ratio, $\nu'$	0.25		
In situ earth pressure ratio, $K_0$	1.0, 1.5, 2.0		

\*Note: the shear strength applies only to the elastoplastic analyses

**Table 3.1 Soil properties for the 2D FE model using the stress reduction method ( $\beta$ -method)**

MC Model	
Total unit weight, $\gamma$ kN/m <sup>3</sup>	20.0
Young's modulus E' MPa	15+1.1z
Undrained shear strength, $s_u$ kPa	75+5.5z
Poisson's Ratio, $\nu'$	0.25
In situ earth pressure ratio, $K_0$	1.0

\*Note: Calculations in this report assume undrained conditions in the clay

**Table 3.2 Input parameters for MC model of London Clay based on C300 design profile**

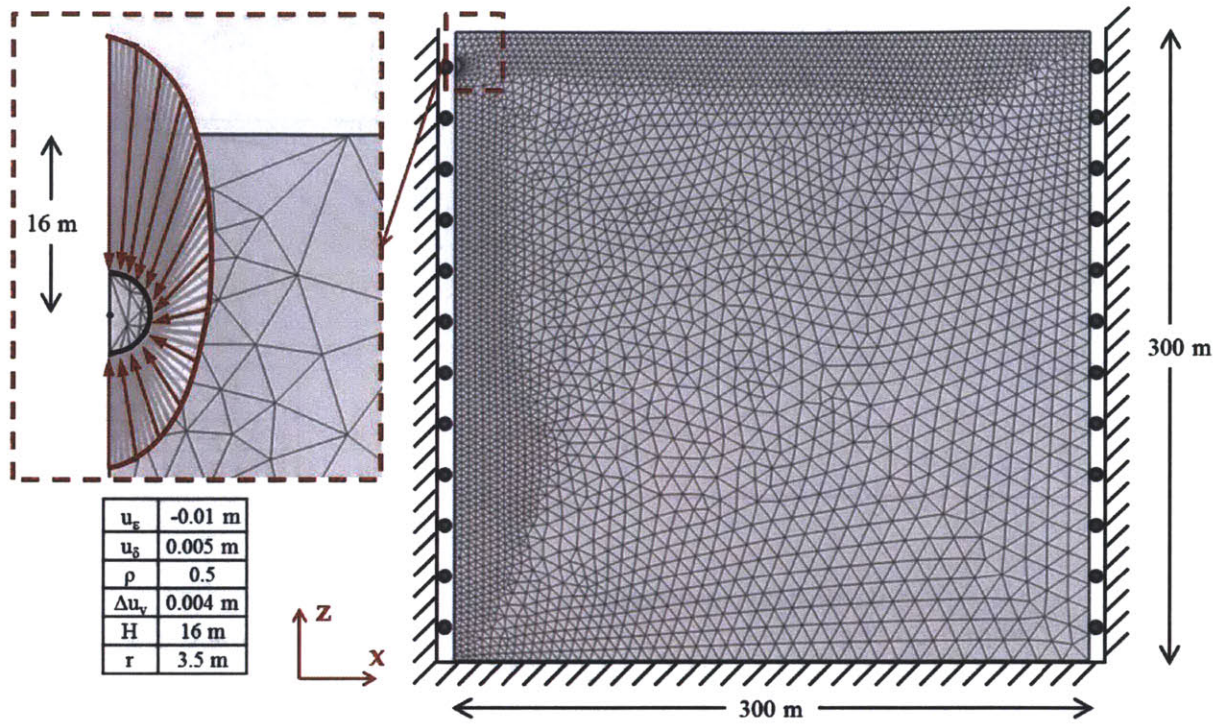


Figure 3.1. 2D Finite element model and imposed boundary conditions

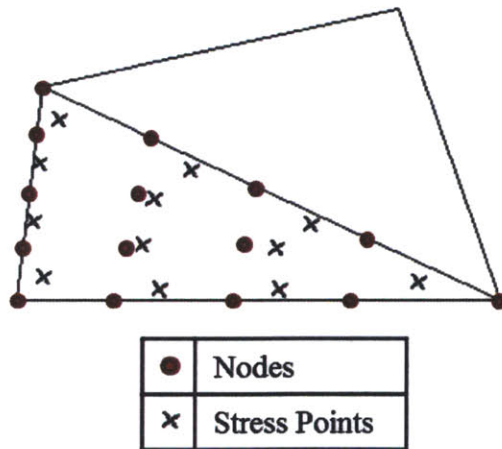
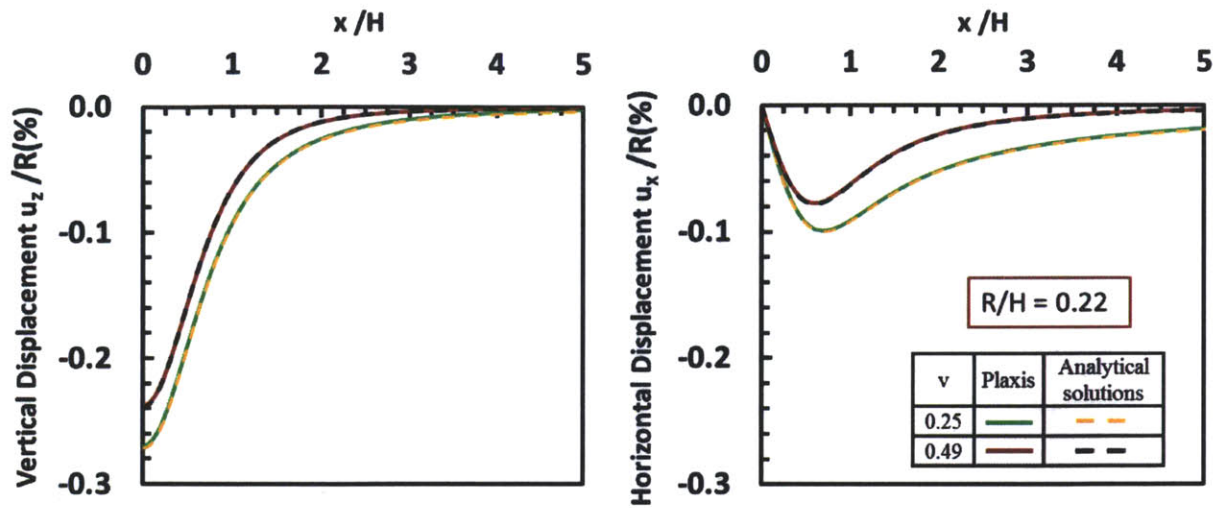
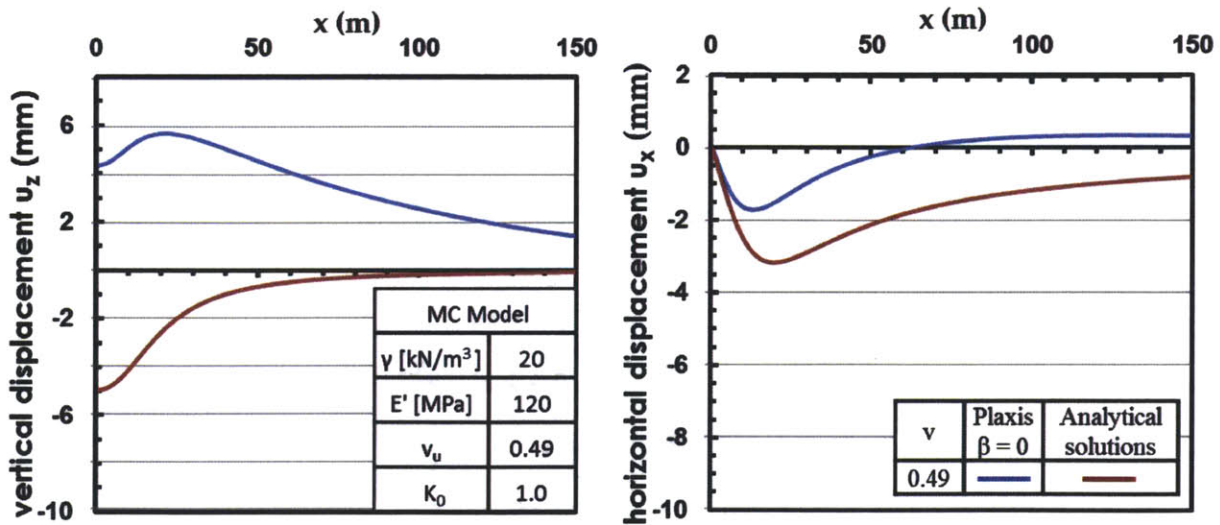


Figure 3.2. 15-node triangular elements used in Plaxis 2D FE model  
(Plaxis Manual: <http://www.plaxis.nl/files/files/2D2011-4-Scientific.pdf>)



a) Vertical displacements      b) Lateral displacements

Figure 3.3. Comparison of ground surface deformations for Plaxis 2D and analytical solutions (Verruijt, 1997)



a) Vertical displacements      b) Lateral displacements

Figure 3.4 . Comparison of ground surface deformations for Plaxis 2D unlined elastic undrained case to the approximate analytical solutions (Pinto and Whittle, 2012)



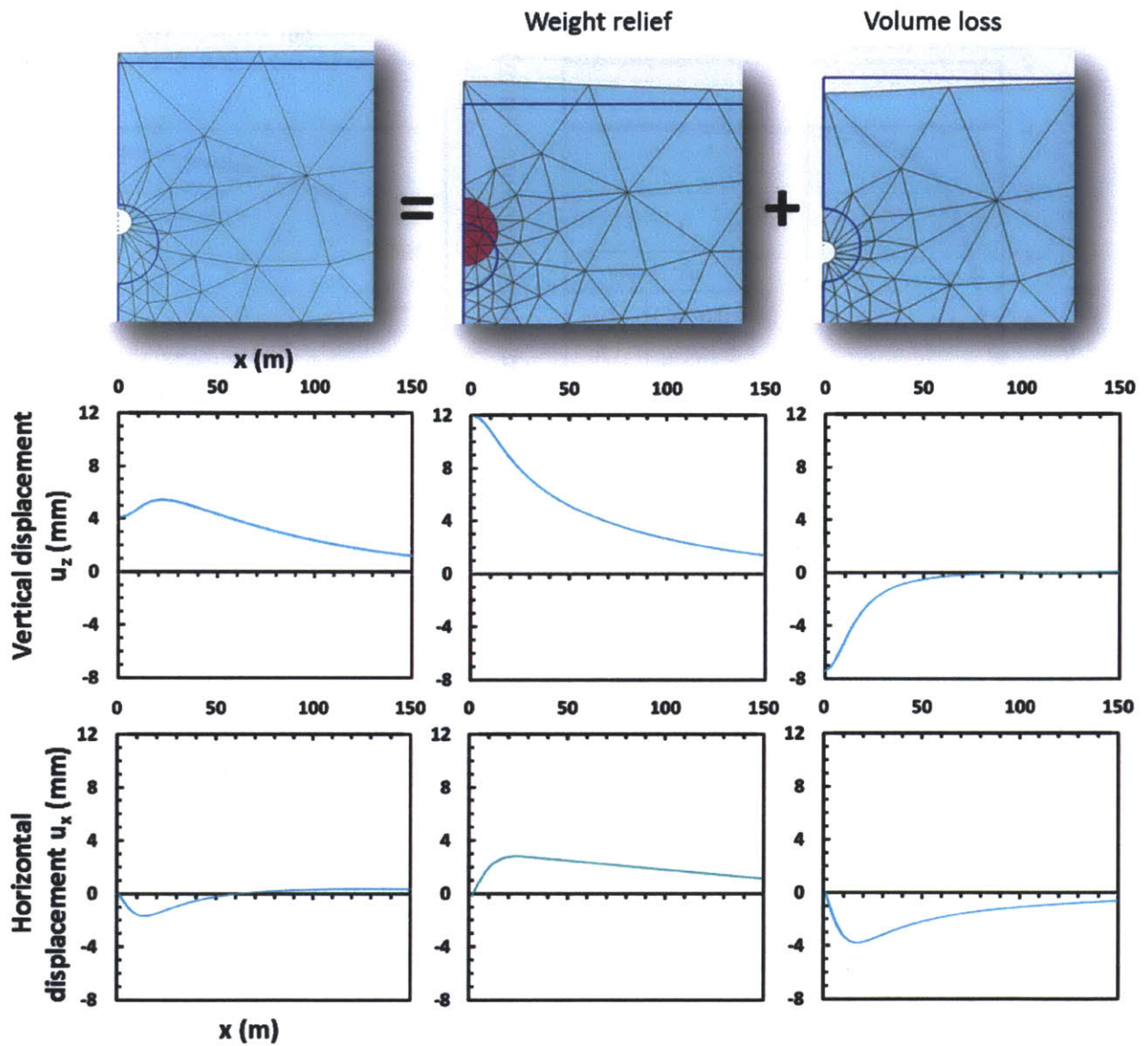


Figure 3.5 Buoyancy effect for the undrained unlined elastic 2D FE model (Elastic analysis)

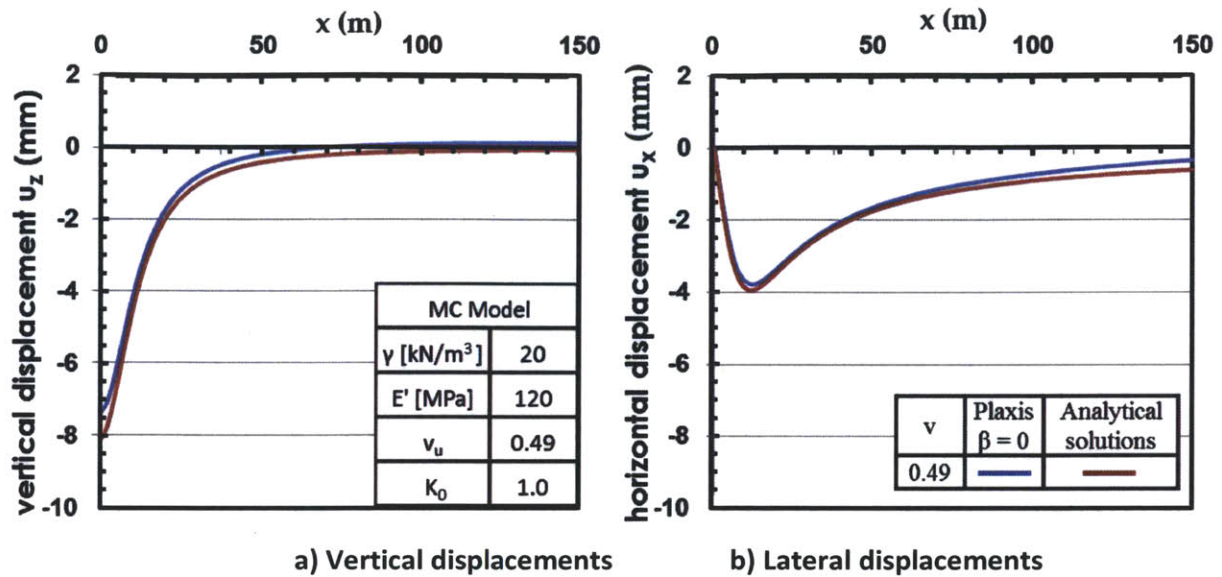


Figure 3.6 The ground surface deformations induced by volume loss computed by Plaxis 2D unlined elastic undrained model are compared to the approximate analytical solutions.

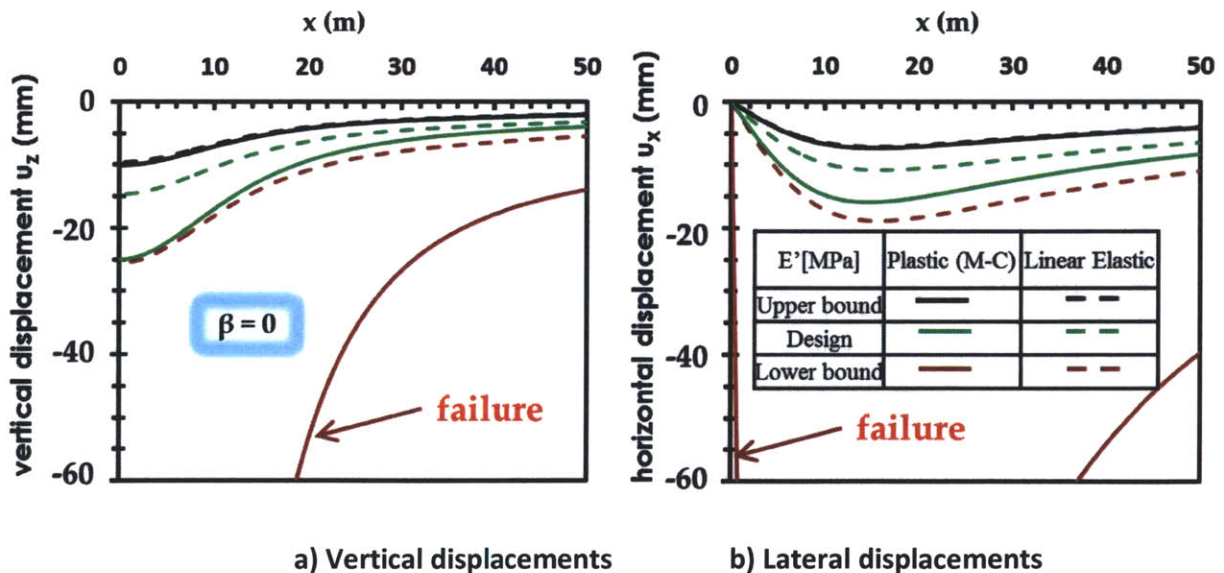


Figure 3.7 Comparison of ground surface deformations for Plaxis 2D unlined undrained model, for the three different three different strength and stiffness soil profiles for elastic and plastic case.



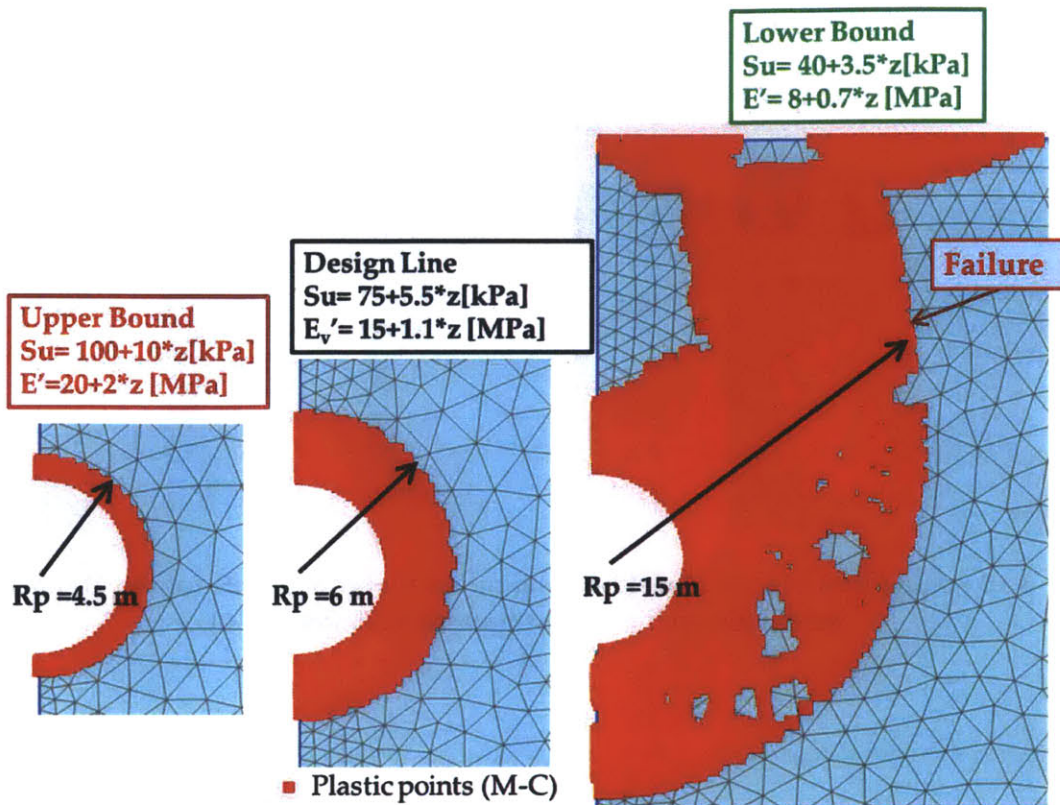


Figure 3.8 Comparison of zone of yield around tunnel for three different strength and stiffness soil profiles, for the 2D unlined FE model (elasto-plastic soil model M-C)

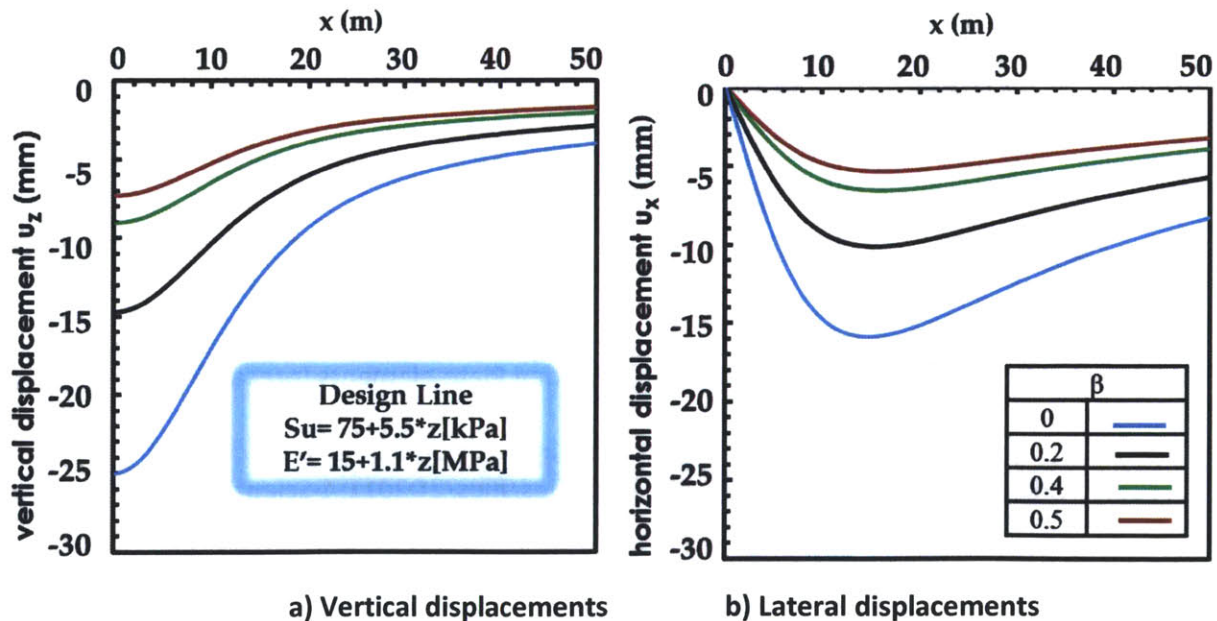


Figure 3.9 Comparison of ground surface deformations for Plaxis 2D unlined undrained model, for the design line (plastic soil model M-C) for  $\beta$ -value varying from 0-0.5

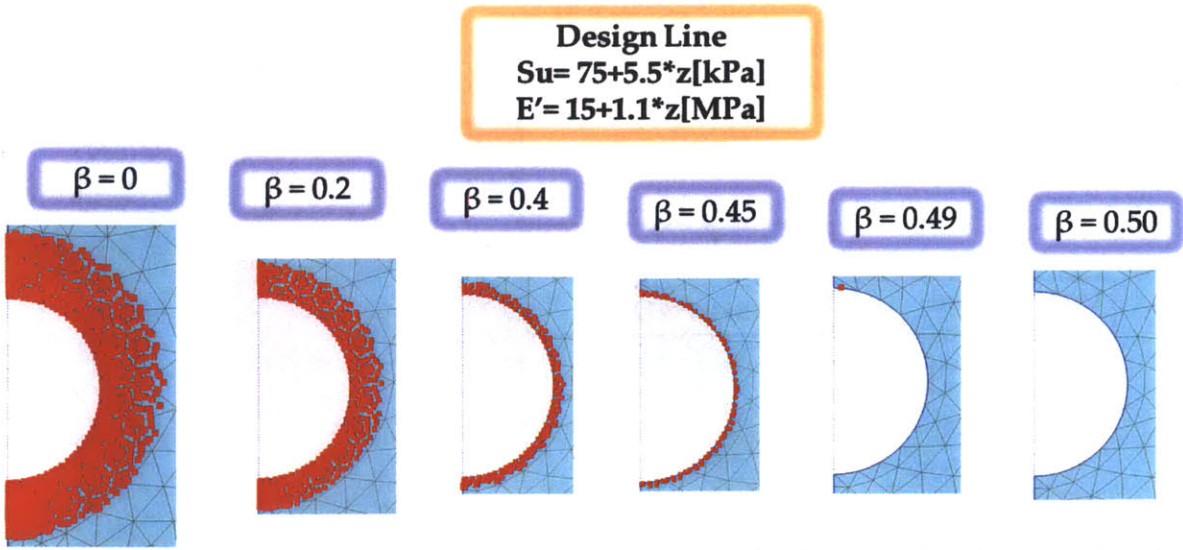


Figure 3.10 Comparison of zone of yield around tunnel for for  $\beta=0 - 0.5$ , for the 2D unlined FE model (design line , elasto-plastic soil model M-C)

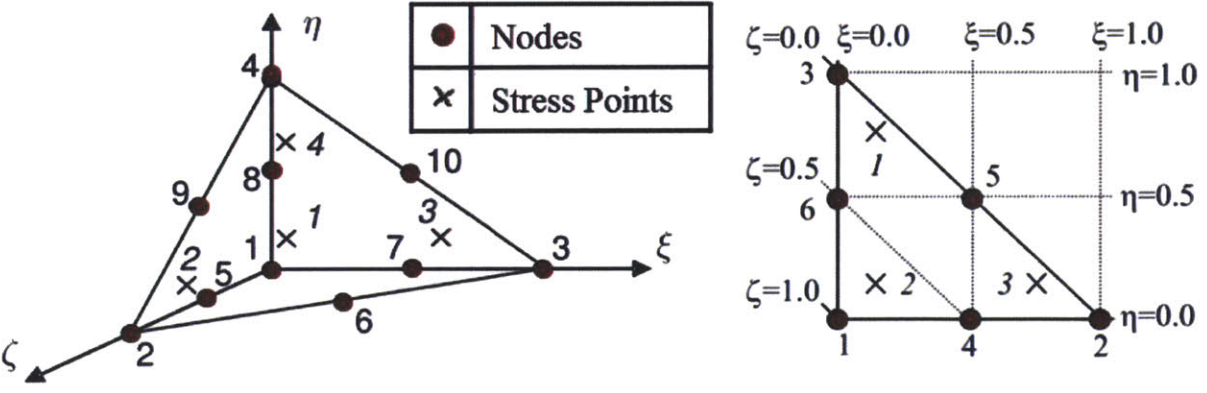


Figure 3.11. Elements used in Plaxis 3D FE model  
 (Plaxis Manual: <http://www.plaxis.nl/files/files/2D2011-4-Scientific.pdf>)



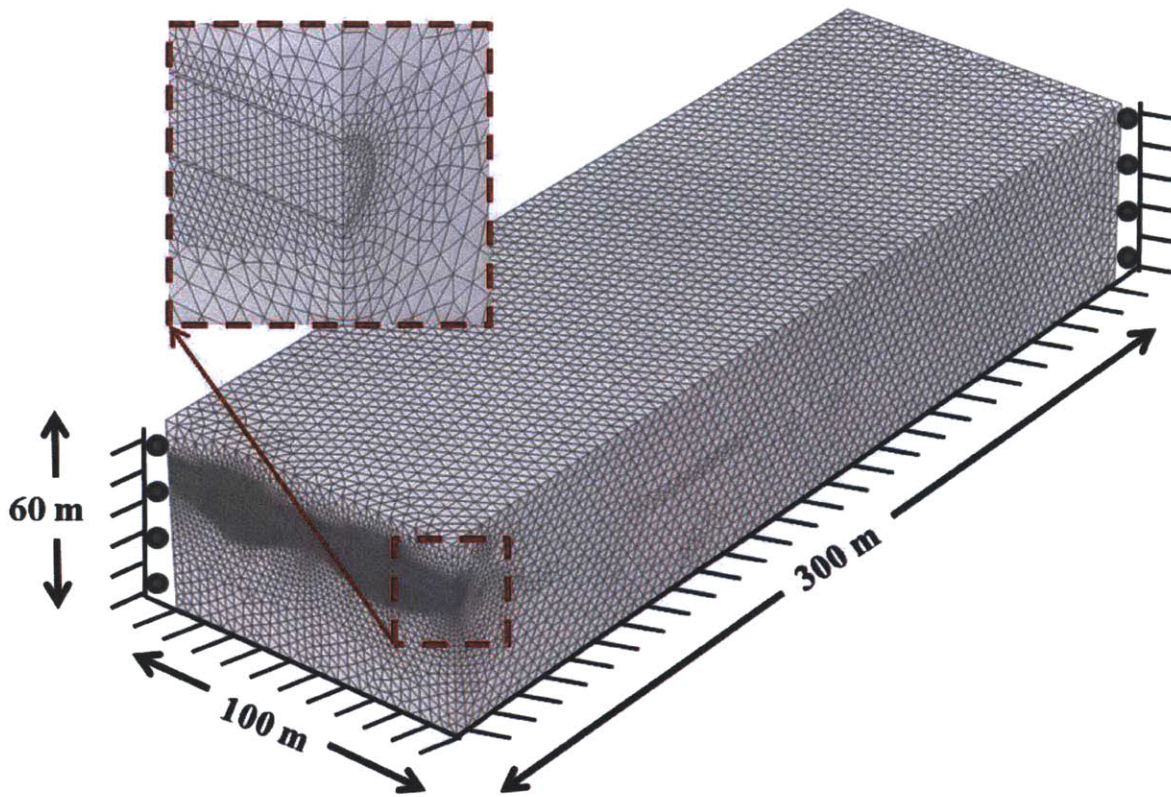


Figure 3.12 Mesh and dimensions for 3D Finite element model

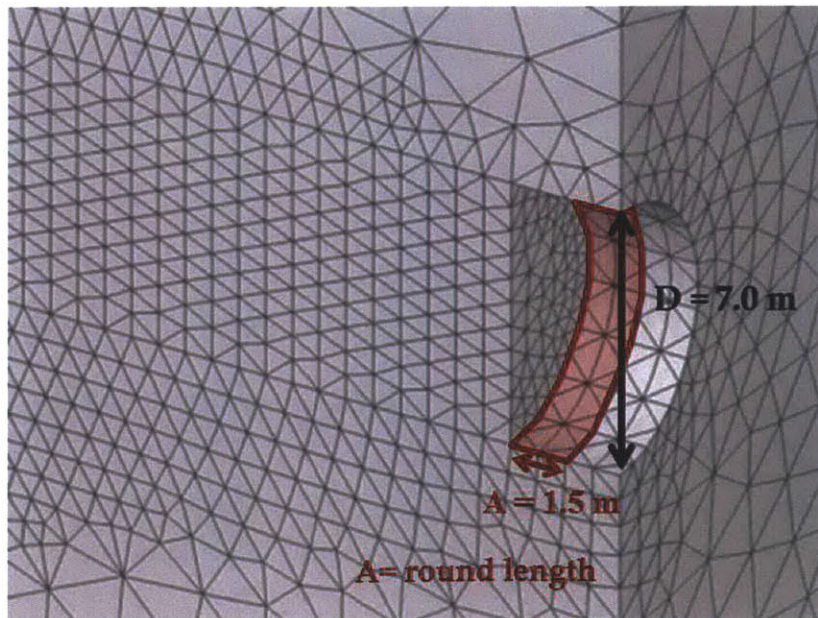


Figure 3.13 Excavation procedure for unlined tunnel

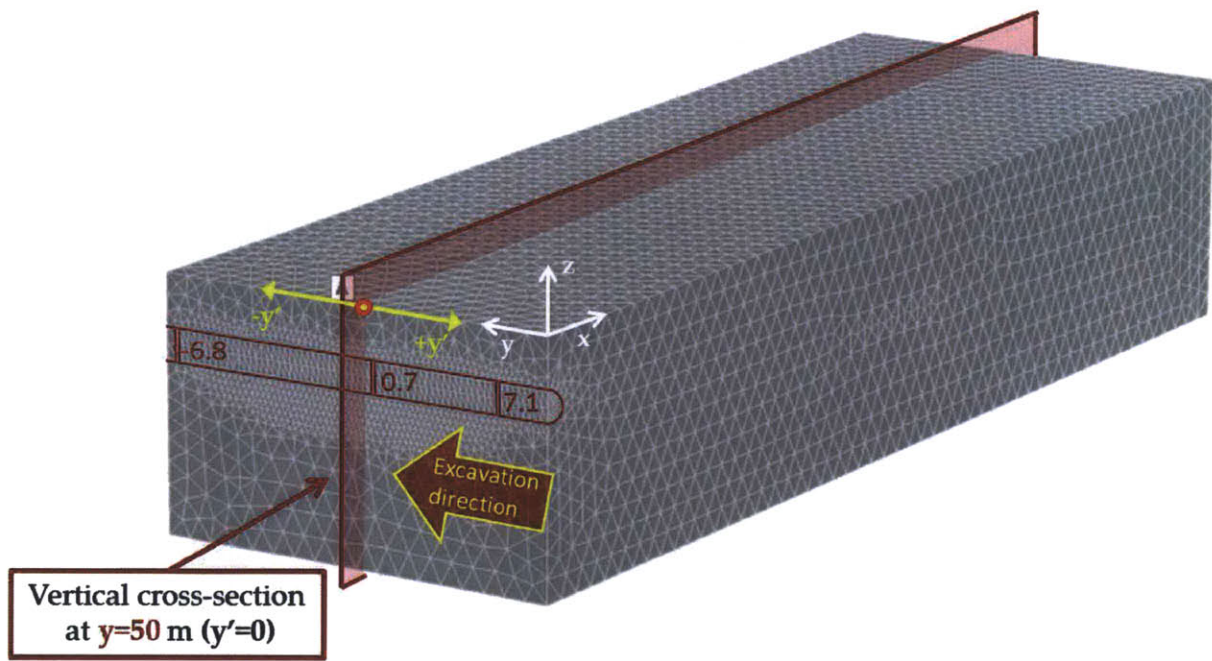
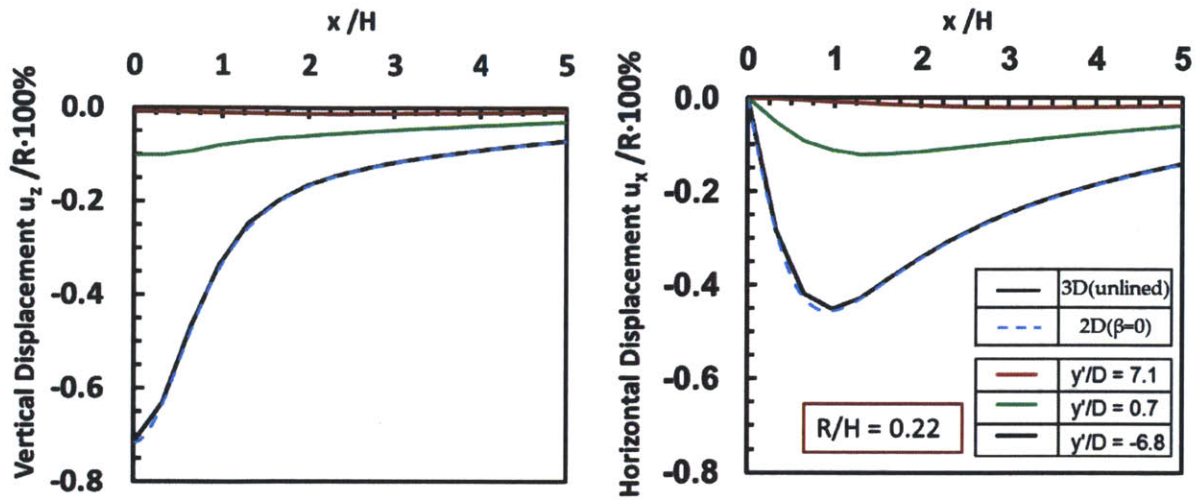
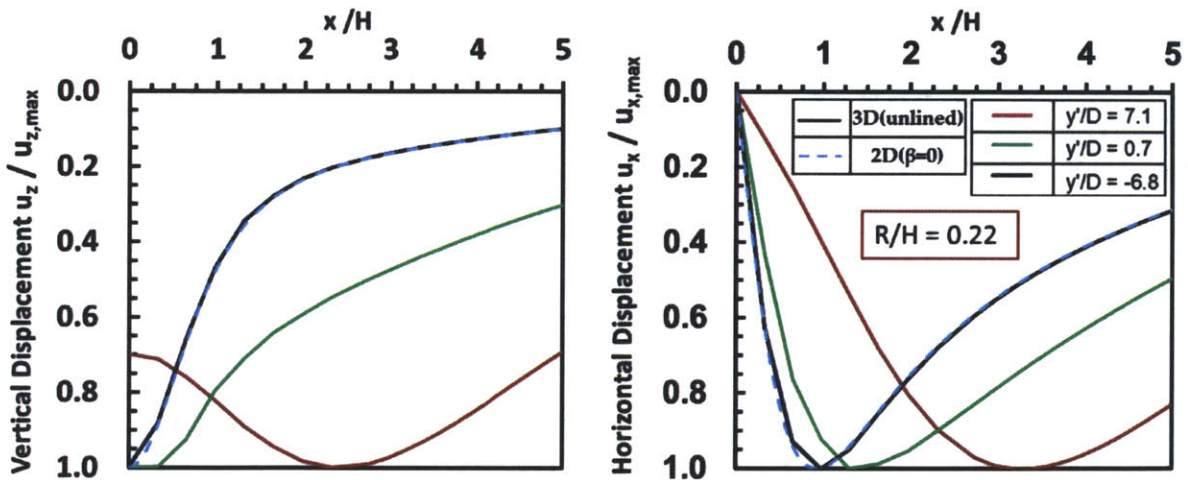


Figure 3.14 Examined central cross-section of the FE model and the three different positions of the face of the excavation



a) Vertical displacements

b) Lateral displacements



c) Normalized vertical displacements

d) Normalized lateral displacements

Figure 3.15 Comparison of ground surface deformations at central section of FE model ( $y' = 0$ ) for 3D and 2D FE models for the unlined case with a Mohr-Coulomb soil model

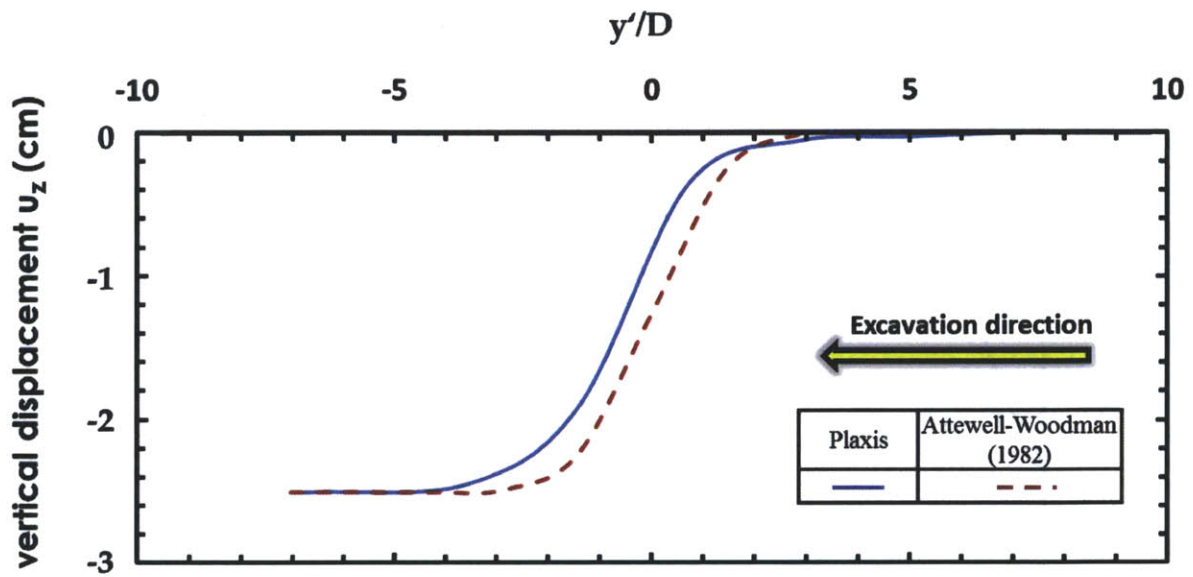
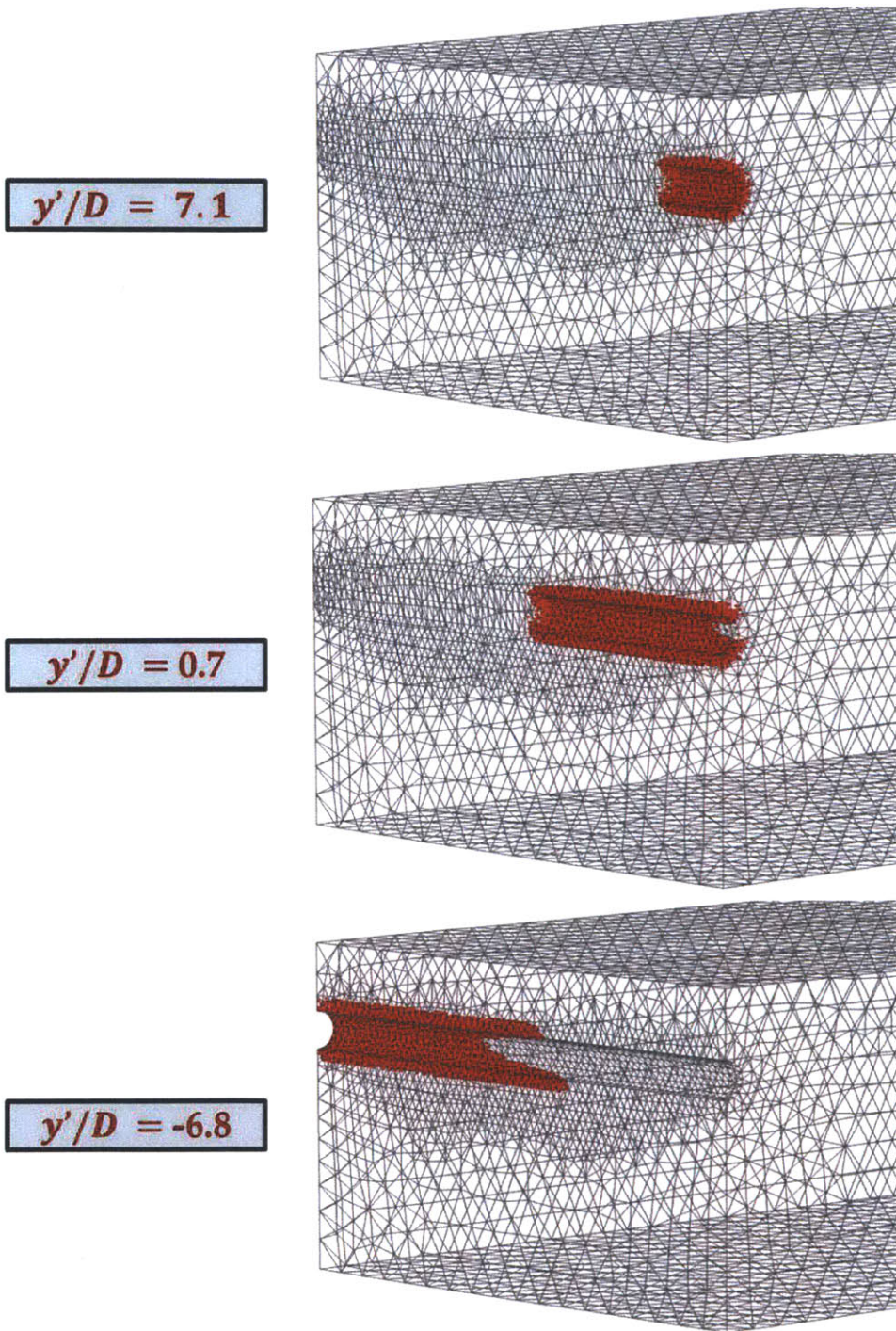


Figure 3.16 Comparison of ground surface deformations as a function of the position of the excavation face at the centerline ( $x=0$ ) of the central section of FE model ( $y'=0$ ) for 3D unlined case with the empirical method proposed by Attewell and Woodman (1982).





■ Plastic points (M-C)

Figure 3.17 Zone of yield around tunnel for unlined case for the three different positions of the face of the excavation





## 4 Finite element model for EPB Tunneling

This section describes the development of a 3-D finite element model for simulating mechanized tunnel construction using an Earth Pressure Balance (EPB) shield machine. The model is based on the geometry of the Herrenknecht EPB machine (**Figure 1.8**) currently being used to bore tunnels for Crossrail C300, with a 7.1m diameter cutting wheel and 12m tapered steel shield (**Figure 1.7 and Figure 4.4**). The analyses consider ground conditions typically associated with the C300 tunnel design section Q (Westbourne Bridge to Paddington Station) depicted in **Figure 4.1**. At this location the tunnel has a cover depth of 12.45m (16m to springline) below ground surface, and is excavated within the London Clay (unit B).

### 4.1 Model Description

After the dimensions and mesh density were selected (using the first simple 3D model), a new more detailed 3D model (**Figure 4.2**) of the mechanized tunnel construction process was created. For this 3D base case model the clay is modelled as an elastic-perfectly plastic material with a Mohr-Coulomb yield criterion [MC] that is subject to undrained shearing. The input parameters used, are listed in **Table 3.2**, represent the London Clay profile. The model assumes undrained shear conditions within the clay (i.e., the model assumes there is no migration of pore water within the clay mass over the time frame of the tunnel construction), and represent a profile where undrained shear strength varies linearly with depth(see **Figure 4.1**). The analyses assume that the groundwater table is coincident with the ground surface and pore

pressures are hydrostatic. Calculations have been performed for two different in situ stress conditions,  $K_0 = 1.0$  and  $1.5$ .

**Figure 4.2** shows a schematic figure of the boundary conditions used to represent the EPB tunnel-boring machine in the Plaxis 3D FE model. The 12 m long shield is represented by a set of 8 x 1.5 m long segments with uniform radial displacement-defined boundaries that match the unstressed dimensions of the conical surface of the shield (**Figure 4.4**). The face conditions are represented through a uniform face pressure, the current base case assumes  $p_g = 150$  kPa.

The simulation of the grout was an essential parameter for a realistic representation of the EPB construction process. The use of grout to fill in the formed gap between the tail of the shield and the lining is crucial for controlling the observed deformations. As will be explained in the following chapter the grout parameters have a significant effect on the surface settlements. The grout activation consists of two faces: the liquid and the hardening state. The first is assumed to extend over one tunnel segment, and is represented through a uniform pressure to represent the liquid state of the grout. The second phase consists of the activation of solid elements to represent the hardened state of the grout. The assumption has been made that for one segment behind the EPB shield the freshly injected grout behaves as a liquid. As a result the expected stiffness of the grout is zero. In order to represent the behavior of a liquid, a uniform pressure grout pressure,  $p_g = 100$  kPa, was applied at the tunnel cavity (ignoring the increase of the hydrostatic pressure with depth), which extends over one tunnel segment (i.e., 1.5 m behind the shield). The plate element representing the lining (**Figure 4.3**) is then activated with

an initial external diameter, 6.8 m and a ring solid elements, representing the hardened grout is activated around the lining.

**Table 4.1** summarizes the elastic properties of the lining and grout. In order to account for the effects of grout set-up properties, a time hardening model proposed by Kasper and Meschke, (2006) was initially used to describe time dependent stiffness of the activated grout (**Figure A.1**). Subsequently a constant set of grout parameters were used based on real grout data collected at the Crossrail project (BFK, 2012). Since the EPB machine is assumed to advance forward in steps, the time parameter is introduced by assuming an average advance rate of 1 m/hr (Melis, 1997). As a result, each excavation step corresponds to a 1.5 h time step.

The simulation of the EPB shield was one of the more challenging parts the current numerical simulation. Plaxis 3D finite element program assumes infinitesimal strains and has no methodology of representing the EPB machine as a distinct structure, so various simplifications had to be made in order to approach the excavation procedure.

The FE model assumes that there is no gap between the surrounding soil boundaries and surface of the shield. The shield is conical with a very small taper angle such that the diameter reduces from 7.08 m at the face to 7.05 m at the tail of the shield (**Figure 4.4**). In comparison the tail void corresponds to a step change in diameter of 0.25 m (7.08 m to 6.80 m for the unstressed lining, **Figure 4.3**).

The current FE model has limited ability to accurately describe the volume loss at the face of the EPB machine as it does not account for soil deformations occurring ahead of the machine (small strain model assumption). As a result, the removed soil volume is underestimated due to

two factors that are not accounted for: relatively large displacements at the tunnel cavity and over-excavation at the face of the excavation. The first factor can be considered as a weakness of the numerical simulation, due to the small strain assumption. This happens because the nominal tunnel diameter (7.1 m), which determines the volume of soil to be removed during the excavation, is defined in the initial undeformed configuration. Ground deformations occur ahead of the face due to stress changes and hence, the model does not control accurately the volume of the soil subsequently excavated. The second factor is related to the over-excavation that can occur at the face of the shield (i.e., the cutting wheel has an overcut diameter) and can be addressed in the same way as the first factor. However, as the percentage of over-excavation is usually hard to determine, this parameter can be ignored. Although the majority of the researchers (Möller, 2006; Kasper and Meschke, 2004 ) don't address either of the two factors, their combined effect can be significant.

It was estimated that the effect of the machine self-weight is canceled out by the weight of the removed soil. As shown in **Figure 4.5** the buoyancy effect due to the removed soil is almost double the weight of the machine. So at the end we have a resulting upward force. This force is not considered in the current analysis. Similarly, as the EPB shield advances, shear stresses develop along the shield-clay interface (c.f., **Figure 4.2**). These shear forces are effectively ignored in the current Plaxis model, but could be included as boundary shear stresses applied at the shield, in a more refined solution.

The face of the EPM machine has the tendency to sink in to the clay due to its weight distribution (the shield is heavier at the face to support the cutter head). In practice, the

machine is steered by a set of hydraulic jacks that control displacement rate around the shield. The jacks are adjusted to compensate for the pitch of the machine and enable steering along prescribed arcs. The net effect is that the shield trajectory is defined but the machine plough through the soil as the centerline of the shield is not necessarily horizontal. In the current analysis the machine is assumed to follow a perfectly horizontal path/trajectory.

## 4.2 Results

The results obtained from the base case 3D finite element model are useful in understanding how EPB tunneling affects ground settlements, the zone of soil yielding and the structural stresses in the lining. Parametric studies show how these results are affected by the assumed soil properties and in situ stress conditions. The surface deformations are examined along the transverse mid-plane of the FE model ( $y' = 0$  m), where results are least affected by the proximity to boundaries of the model. As depicted in **Figure 3.14**, three reference locations of the EPB machine are considered ( $y'/D = 7.1, 0.7$  and  $-6.8$ ). The first location ( $y'/D = 7.1$ ) represents conditions where the EPB shield becomes fully embedded in the FE model, for the second ( $y'/D = 0.7$ ) is when the face approaches the central-plane of the model, and the third ( $y'/D = -6.8$ ) corresponds to the exit of the EPB machine from the rear face of the FE model.

### 4.2.1 Ground deformations

**Figure 4.6** compares the effect of the in situ  $K_0$  stress condition ( $K_0=1.0$  vs  $1.5$ ) on the computed distribution of ground movements (magnitudes of the displacement vector,  $|u|$ ) for the three aforementioned reference locations of the EPB machine ( $y'/D = 7.1, 0.7$  and  $-6.8$ ). For  $K_0=1.0$ ,

the maximum displacement  $|u| = 38$  mm occurs at the crown of the tunnel cavity immediately behind the shield (where grout pressure is applied), while for  $K_0=1.5$  the maximum displacement  $|u| = 42$  mm occurs at the springline of the tunnel cavity at the back of the shield. The model predicts maximum surface displacements, for  $K_0=1.0$   $|u| = 9$  mm along the centerline of the tunnel and for  $K_0=1.5$   $|u| = 10$  mm along the centerline of the tunnel. So, the case with  $K_0=1.5$  generally produces slightly larger displacements in both the far (i.e, surface) and the near fields, due to the release of higher initial horizontal stresses. The magnitude of the surface displacements and the extent of the influence zone (i.e., where  $|u| > 2$  mm) are larger for the  $K_0=1.5$  case. For  $K_0=1.0$  the influence zone extends up to 30 m ahead of the tunnel face and 100 m in the transverse direction, while for  $K_0=1.5$  the influence zone extends up to 35 m ahead of the tunnel face and 125 m in the transverse direction.

**Figure 4.7** depicts the deformed mesh (scaled up 50 times from the real scale so that the close field deformations can be visible) for the three reference locations of the EPB machine,  $y'/D = 7.1, 0.7$  and  $-6.8$ . As expected the larger displacements concentrate in the close field around the tunnel, resulting from the imposed displacement boundary conditions that define the conical shape of the shield. The deformed mesh looks exactly the same for both  $K_0$  values and the magnitudes of the close field displacements are almost the same. However the shape of the tunnel cavity differs, for  $K_0=1.0$ , the deformation mode correspond to uniform convergence (see **Figure 2.12**), whereas for  $K_0=1.5$  there is also ovalization at the tunnel cavity.

## 4.2.2 Comparison of surface settlements

**Figure 4.8** compares the vertical and horizontal components of surface deformations along the transverse mid-plane of the FE model ( $y' = 0$  m) for different  $K_0$  values at the three reference locations of the EPB machine,  $y'/D = 7.1, 0.7$  and  $-6.8$ .

In general, the analyses with  $K_0 = 1.5$  produce larger far field settlements ( $x > 15-20$ m) and smaller lateral deformations than the analyses with  $K_0 = 1.0$ . There is also an important switch in the shape of the settlement trough for  $K_0 = 1.5$  as the tunnel face passes the mid-plane ( $y'/D = 0.7$  to  $-6.8$ ; **Figure 4.8b and c**), such that the maximum settlement is offset from the centerline and much smaller settlements occur at locations close to the centerline ( $x < 15$ m).

The results for  $K_0 = 1.5$  show a slight increase in the magnitudes of computed displacements compared to  $K_0 = 1.0$  ahead of the advancing EPB machine ( $y'/D = 0.7$ ). However, as the shield moves past the central plane there is a marked change in the surface settlement mode shape for  $x \leq 10$ m and a small net increase in the centerline surface settlement for  $y'/D = 0.87$  to  $-6.8$ .

**Figure 4.11** and **Figure 4.10** show results for the three surface displacement components ( $u_x, u_y, u_z$ ) at five selected locations along the mid-plane section (**Figure 4.9**) as functions of the EPB face location ( $y'/D$ ) for  $K_0 = 1.0$  and  $K_0 = 1.5$  value. For  $K_0 = 1.0$  conditions, very small settlements ( $u_z \leq 2.5$ mm) occur as the EBP advances towards the mid-plane of the model ( $y'/D = 0.7$ ; **Figure 4.8a** and **Figure 4.11b**). The settlements increase significantly with the passage of the shield ( $y'/D = 0$  to  $-1.7$ ) and continue to develop around the lining rings until  $y'/D \approx 3.7$ . The transverse ( $u_x$ ) displacement components are of comparable magnitude to the vertical

settlements ( $u_z$ ; **Figure 4.8b vs Figure 4.8a**) with a maximum inward movement,  $u_x \approx 6.3$  mm occurring at an offset of 16m from the centerline compared with a maximum centerline settlement,  $u_z = 7.2$  mm. The central plane of the FE model is not affected by the boundaries of the FE model. It is therefore more surprising to find that the EPB base case model produces net longitudinal surface displacements at the mid-plane section. **Figure 4.11b** shows that surface centerline is moving towards the advancing EPB machine,  $u_y = 6.8$  mm (at  $y'/D = -1.3$ ) rebounding to 5.2 mm as the EPB machine approaches the rear boundary of the model ( $y'/D = -6.7$ ). This behavior is related to plastic soil deformations occurring around the tunnel shield. For  $K_0 = 1.5$  conditions, the longitudinal displacements increase to  $u_y = 8.0$ mm (**Figure 4.11**) since the initial horizontal stresses are higher and there is a larger change effect of stress changes at the face of the EPB machine.

**Figure 4.10a, b** show components of surface displacements vectors ( $u_x, u_y, u_z$ ) in longitudinal plane ( $u_y, u_z$ ) and transverse plane ( $u_x, u_z$ ), for the 5 points selected above. The vectors in the longitudinal planes (**Figure 4.10a**) follow a unique ratio as the tunnel advances towards the central plane. The results show small changes in  $u_y$  during passage of the shield (up to a maximum  $u_y$  at the tail of the shield) and then rebound as the EPB moves onwards. It is interesting to note that the ratios of  $u_x$  to  $u_z$  (**Figure 4.10b**) remain constant throughout the tunnel advance and are controlled by the initial offset locations.

### 4.2.3 Comparison of tunnel cavity deformations

**Figure 4.12** summarizes the interpreted tunnel cavity mode shape parameters ( $u_e, u_\delta, \Delta u_z$ ; cf. **Figure 2.12**) obtained from the computed deformations vectors in the clay, as a function of  $y'/D$



for the 3D base case EPB tunnel. The figure shows how the parameters are obtained by fitting the deformations at the crown, invert and springline of the cavity. **Figure 4.12** shows that uniform convergence ( $u_{\epsilon}$ ) is the dominant mode shape. This is not surprising given the fact that displacements are controlled primarily by the radial displacement boundary conditions at the shield. The results show that the ovalization mode ( $u_{\delta}$ ) is negligible for  $K_0 = 1.0$  and there is a small translational effect associated with buoyancy ( $\Delta u_z$ ). The results for  $K_0 = 1.5$  show a small change in the convergence and a small amount of ovalization ( $u_{\delta} < 0$  indicates inward movement at the springline). These results are not sufficient to explain the change in mode shape of settlements at the ground surface (see **Figure 4.8**).

One possible cause is the difference in displacement mode shapes at the tunnel cavity (as shown by Zymnis et al., 2013) Although similar results have been observed in published FE analyses (e.g., Möller, 2006; Franzius et al., 2005; Addenbrooke et al., 1997) there are no real data with similar settlement trough shapes, even for soil profiles with  $K_0$  significantly larger than 1. Hence, there is an aspect of tunnel performance that is not reliably modeled by the current FE models.

#### 4.2.4 Comparison of structural forces

**Figure 4.13 a** and **b** compare the mobilized shear strength ( $\tau_{rel} = \tau/\tau_f$ ; where  $\tau$  is the maximum shear stress<sup>6</sup> and  $\tau_f$  the undrained shear strength;  $\tau_{rel} = 1$  defines the plastic failure zone) for simulations with  $K_0 = 1.0$  and 1.5. As depicted in **Figure 4.13 a**, it is clear that the plastic zone is

<sup>6</sup> The maximum shear stress is defined as :

$$\tau = \sqrt{J_2} = \sqrt{\frac{1}{2} \left( (\sigma'_{xx} - \sigma'_{yy})^2 + (\sigma'_{yy} - \sigma'_{zz})^2 + (\sigma'_{zz} - \sigma'_{xx})^2 + 6(\sigma_{xy}^2 + \sigma_{yz}^2 + \sigma_{zx}^2) \right)}$$

larger for the  $K_0 = 1.5$ . Another difference between the two cases, is that for  $K_0 = 1.0$  the plastic zone boundary is a circle with  $R_p=4\text{m}$  around the tunnel (i.e. the radius of the plastic zone is  $R_p=4\text{ m}$ ), whereas for  $K_0 = 1.5$ , the yielding zone becomes an ellipse varying from  $R_p=5\text{ m}$  at the crown to  $R_p=4\text{ m}$  at the springline. Thus, for  $K_0 = 1.5$  the width of the plastic zone triples at the invert and the crown ( $\Delta r=1.45\text{ m}$  at the crown vs  $\Delta r=0.45\text{ m}$  at the springline). In **Figure 4.13 b** becomes obvious that the width of the plastic zone reaches its maximum width rather quickly, when the face of the excavation is 6 m ahead of the examined cross-section (i.e. half the length of the EPB machine) and remains almost constant afterwards.

**Figure 4.14** compares the variation of the computed axial compression,  $N_\theta$  (compression is negative) and the ring bending moment,  $M_y$  in the lining for  $K_0 = 1.0$  and 1.5 at the end of the tunnel construction. The structural forces were plotted for a reference lining ring located at the mid-plane of the finite element model. The plotted values correspond to values averaged over each node of the lining ring and then over the width of the ring. The limits of the maximum and minimum computed structural forces are also plotted, showing in a clear manner, the association between the fluctuation in structural forces and the selected dimension of the finite elements. As result, the computed structural forces had to be averaged first over the neighboring elements and then over the whole ring width, in order to eliminate local effects.

As expected, the bending moment is almost zero for  $K_0 = 1.0$  (uniform convergence, **Figure 4.14**), whereas for  $K_0 = 1.5$  maximum moment occurs at the springline, crown and invert (ovalization mode). For  $K_0 = 1.0$  the axial force is almost constant throughout the ring ( $N_\theta \approx 450\text{ kN/m}$ ), due to the fact that the uniform convergence is the main deformation mode. Whereas

for  $K_0 = 1.5$  the axial force increases towards the crown and invert. It should be noted that for both  $K_0 = 1.0$  and  $1.5$  cases, the axial force and the bending moment are within the allowable limits for segmental lining systems as shown in **Figure 4.17** (computed by Iftimie, 1996 for similar lining geometry i.e., precast segmental lining with plane-faced joints, and 0.3 m thick) as the one used in the base case model , (see **Figure 4.3**)

**Figure 4.15** compares the computed structural forces in the lining at first activation ( i.e, after passage of the TBM) and the end of the tunnel construction. As expected, for a constant grout stiffness, there is a negligible variation in the structural forces between the time when the ring was first activated and at the end of the construction. For  $K_0 = 1.0$  there is a small decrease in the axial force in the springline and an increase at the axial force in the crown at the end of the construction. As shown in **Figure 4.16** , although the axial force at the springline was initially greater than the one in the invert and the springline, when the EPB moves one machine length away (12m) all the forces converge to the same value -450 kN (compressive). This effect can be attributed to the fact that it takes some time for the forces to fully equilibrate in the activated lining ring.

### **4.3 Effects of face and grout pressure**

In order to understand the effect of key input parameters in the 3D finite element model parametric analyses are very helpful. There are many parameters affecting the displacements and structural forces, such as the soil model and properties (stiffness and strength profile), grout hardening model, lining properties etc. Initially we have focused on parameters relating to the control of the EPB machine, principally face and grout properties.

### 4.3.1 Grout pressure

The injected grout is assumed to fill the tail void as a liquid injected over one tunnel segment (i.e. uniform pressure is applied to represent this state) and for the next steps solid elements are activated representing the hardened state of the grout. In order to quantify the effect of the grout pressure (representing the liquid state of the grout), a typical range (for an EPB construction method) was selected, varying from 50 to 200 kPa. The effect of the applied grout pressure was examined both in terms of surface displacements and structural forces.

**Figure 4.18** compares the ground surface deformations at central section of FE model ( $y' = 0$ ) for grout pressure,  $p_g = 50, 100, 150$  and  $200$  kPa for different  $K_0 = 1.0$  and  $1.5$  for the three reference locations of the EPB machine,  $y'/D = 7.1, 0.7$  and  $-6.8$ . As expected the grout pressure affects the resulting displacements in the middle plane only after the EPB moves past the examined section and the lining is activated. It can be seen that a variation of  $\Delta p_g = 150$  kPa in the grout pressure produces a maximum variation of 1 mm in the vertical displacement and 0.5 mm in the transverse horizontal direction. The effect of the grout pressure variation on the resulting surface displacements is surprisingly similar for both  $K_0 = 1.0$  and  $1.5$ .

**Figure 4.19** compares the computed structural forces for grout pressure  $p_g = 50, 100, 150$  and  $200$  kPa for different  $K_0 = 1.0$  and  $1.5$ ). The structural forces were plotted for the reference lining ring located at the mid-plane of FE model ( $y' = 0$ ), for the cases  $y'/D = -1.9$ ; the examined lining ring is first activated and  $y'/D = -7$ ; after the end of the tunnel construction. The plotted values correspond to values averaged first over the ring elements and then over the ring width. Generally, the variation of the grout pressure has a negligible effect on the computed structural

forces. It only seems to affect the initially developed axial forces for the  $K_0 = 1.0$  case, resulting to a 100 kN variation in the axial force for the 150 kPa variation in the grout pressure.

**Figure 4.20** shows a comparison of the structural forces at the crown, the springline and the invert for grout pressure 50 kPa to 200 kPa at the lining ring located at the middle plane, as a function of the EPB position for  $K_0$  values (1.0-1.5). The bending moment is approximately constant as the EPB advances forward for both  $K_0 = 1.0$  and 1.5. However the initially computed axial forces, reach a constant value only after the EPB advances one machine length away (12m) from the examined cross-section. As already mentioned in the previous section, this can be attributed to the fact that it takes some time for the forces to fully equilibrate after the lining ring is activated.

### **4.3.2 Face pressure**

A typical range of face pressure (for EPB construction method at this depth) was selected varying from 100 to 250 kPa. The effect of the applied face pressure was examined in terms of surface displacements.

#### **4.3.2.1 Comparison of surface settlements**

**Figure 4.21** compares the ground surface deformations at central section of FE model ( $y' = 0$ ) for face pressure  $P_f = 100, 150, 200$  and 250 kPa for different  $K_0$  values (1.0 and 1.5) at the three reference locations of the EPB machine,  $y'/D = 7.1, 0.7$  and  $-6.8$ . The face pressure starts to affect the resulting displacements in the middle plane as the EPB approaches the examined section. The main effect takes place for  $y'/D = 0.7$ , when the EPB reaches the examined section.

It can be seen that a variation of 150 KPa in the face pressure results in a maximum variation of 2.7 mm in the vertical displacement and 1.2 mm in the transverse horizontal direction. As the machine advances forward, approaching the rear face of the model the resulting variation in the settlement displacements is almost reduced in half, i.e. a maximum variation of 1.5 mm in the vertical displacement and 0.7 mm in the transverse horizontal direction. This can be explained by the fact that the soil rebounds to its initially position as the EBP machine approaches the rear boundary of the model ( $y'/D = -6.7$ ) (**Figure 4.11b**). This behavior is related to plastic soil deformations occurring around the tunnel shield. The effect of the face pressure on the structural forces is negligible. This was expected as the face pressure isn't directly related to lining system.

	<b>Material Model</b>	<b><math>\gamma</math> [ kN/m<sup>3</sup> ]</b>	<b><math>E'</math> [MPa]</b>	<b><math>\nu'</math></b>
<b>Grout</b>	K-M* 2006	15	$0.5-100 \cdot 10^3$	0.18-0.4
<b>Lining</b>	Linear Elastic	25	25,400	0.15

\*Kasper and Meschke (2006)

**Table 4.1. Properties of tunnel lining and grout**

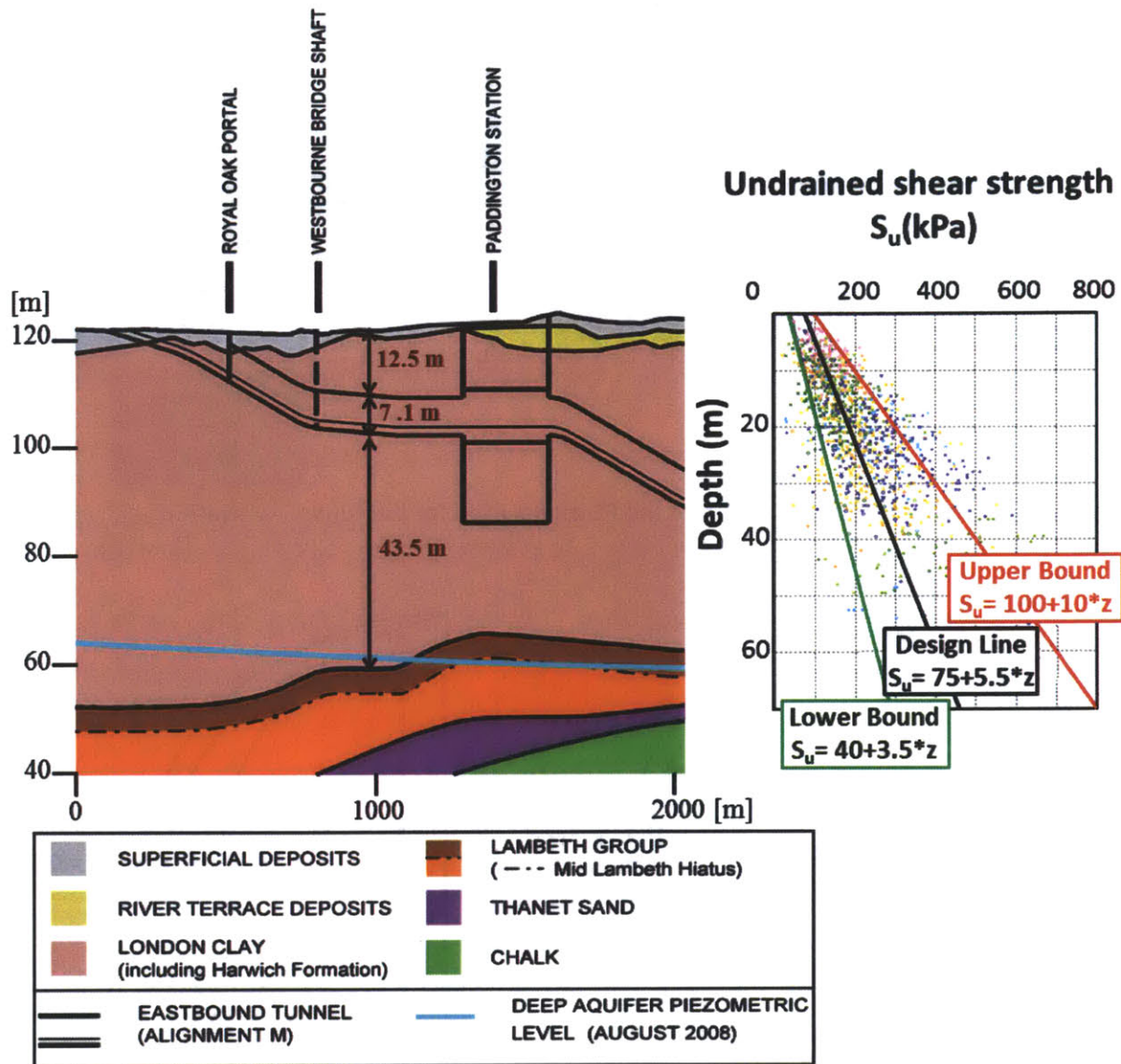


Figure 4.1 Soil Profile at Paddington Station area (source: Crossrail Report, 2012)

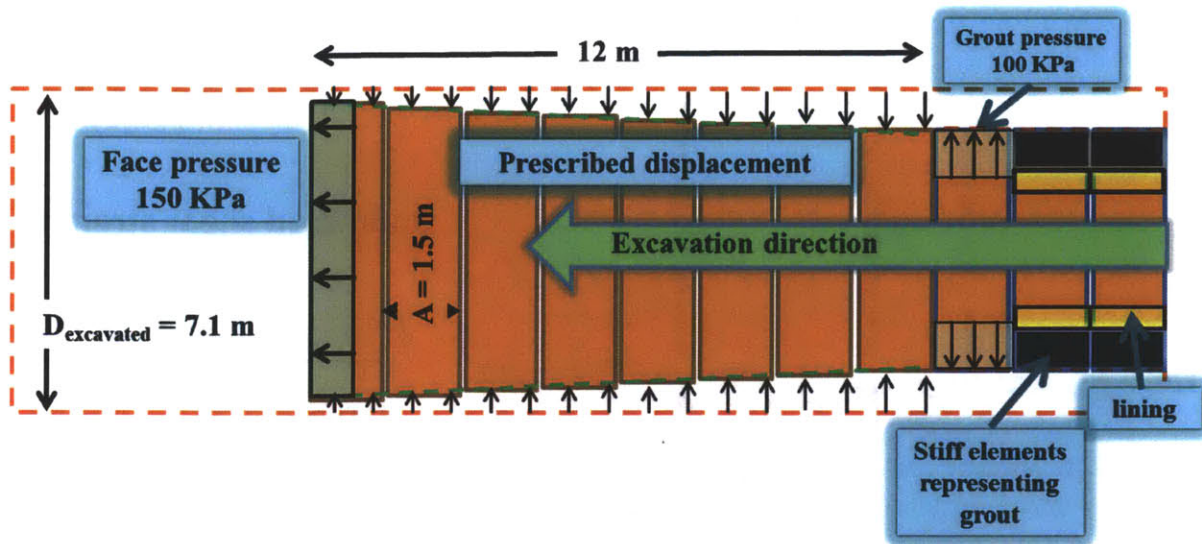
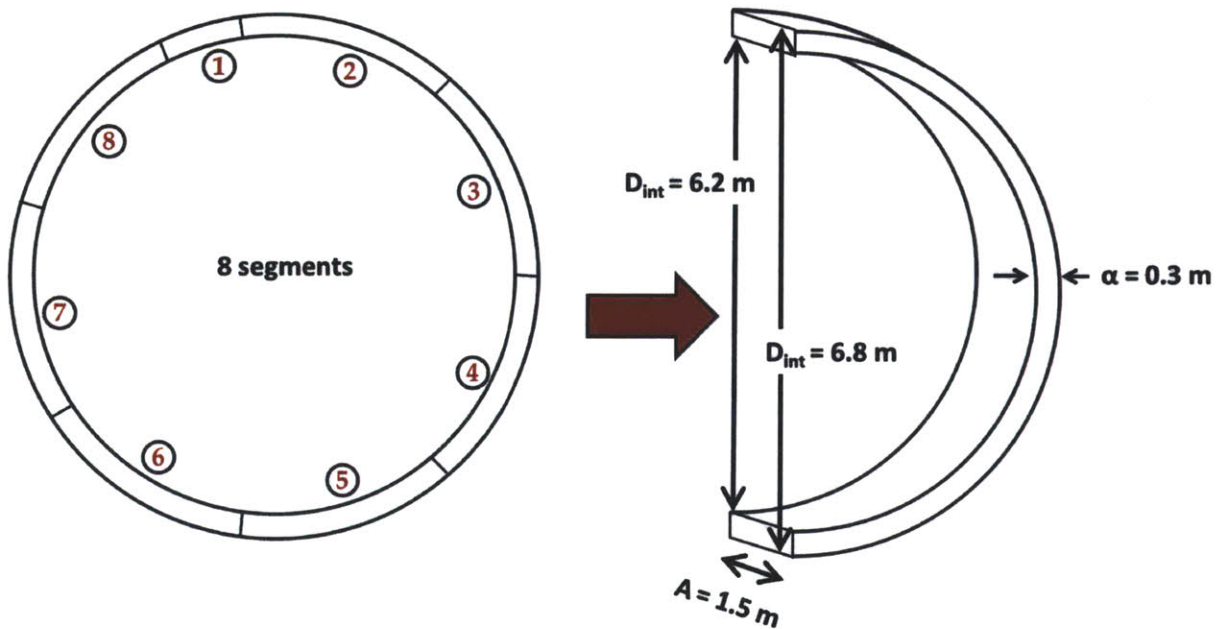


Figure 4.2. Schematic representation of the FE model used for the tunnel excavation



a) Precast segmental lining system

b) Dimensions of plate element representing lining

Figure 4.3 Precast segmental lining system



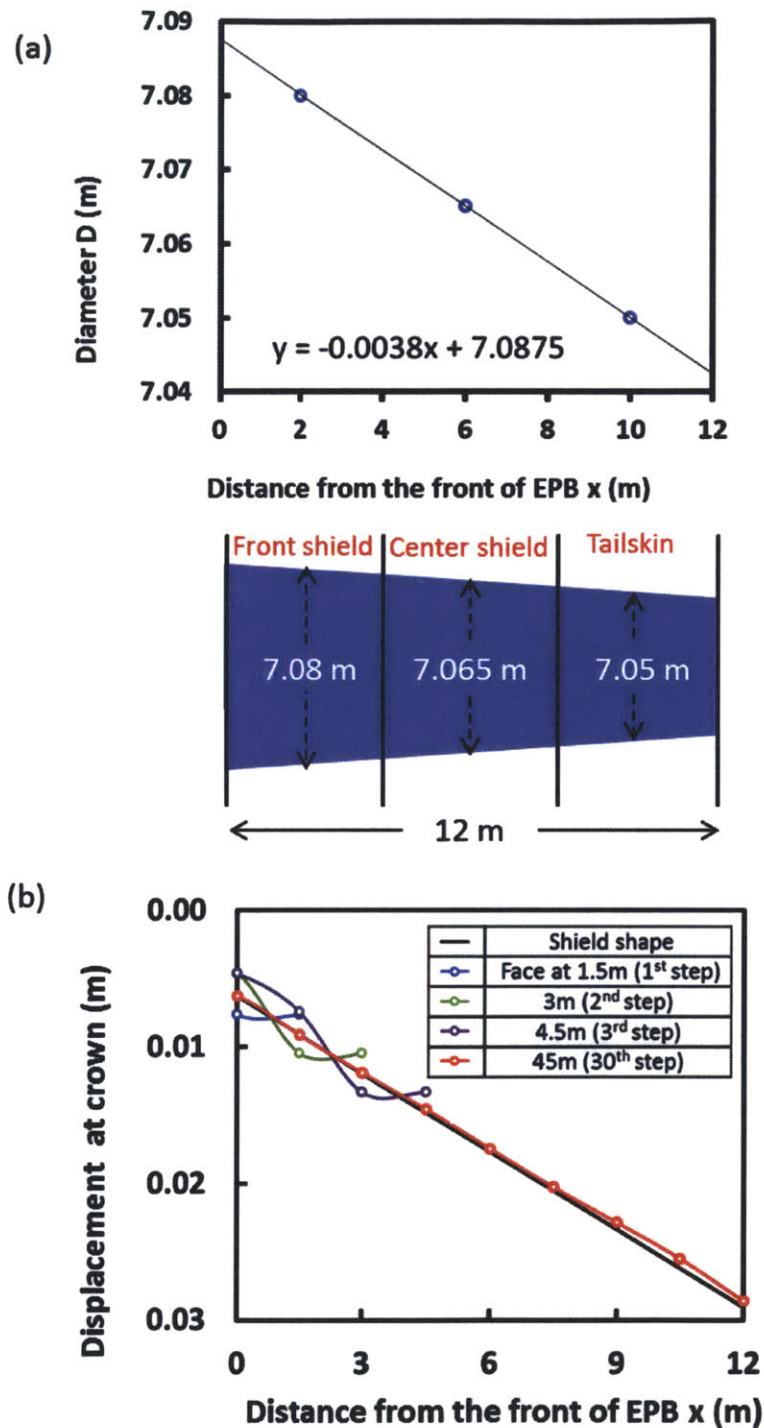
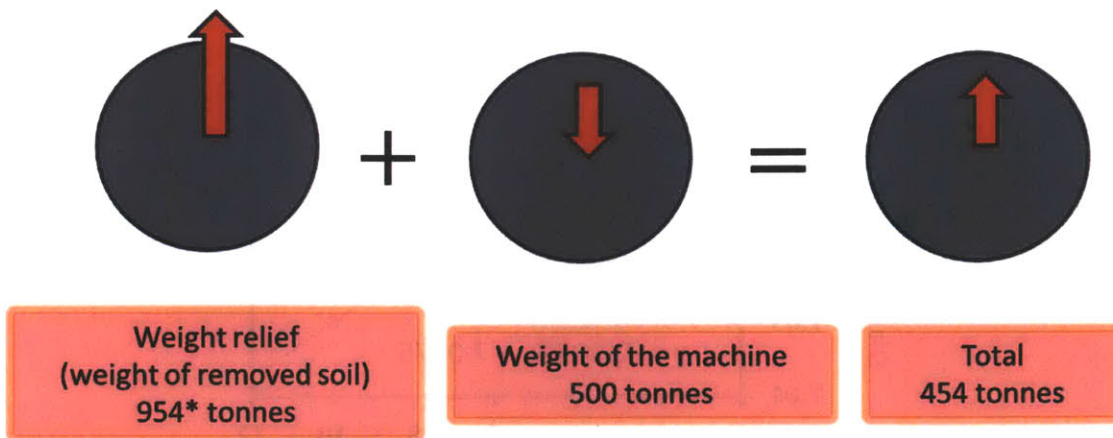


Figure 4.4 Shape of conical EPB shield (a) dimensions of the shield based on the diameter of the front shield, center shield and tailskin, (b) comparison of the applied displacements on the crown nodes of the shield skin in the 3D model to the desired shape of the shield, for three different positions of the EPB face shield.



\*weight of removed soil=(unit weight)·(volume)= $(20 \cdot 0.1) \cdot \left(\pi \cdot \frac{7.1^2}{4} \cdot 12\right) = 954 \text{ tonnes}$

Figure 4.5 The buoyancy effect that cancels out the weight of the machine

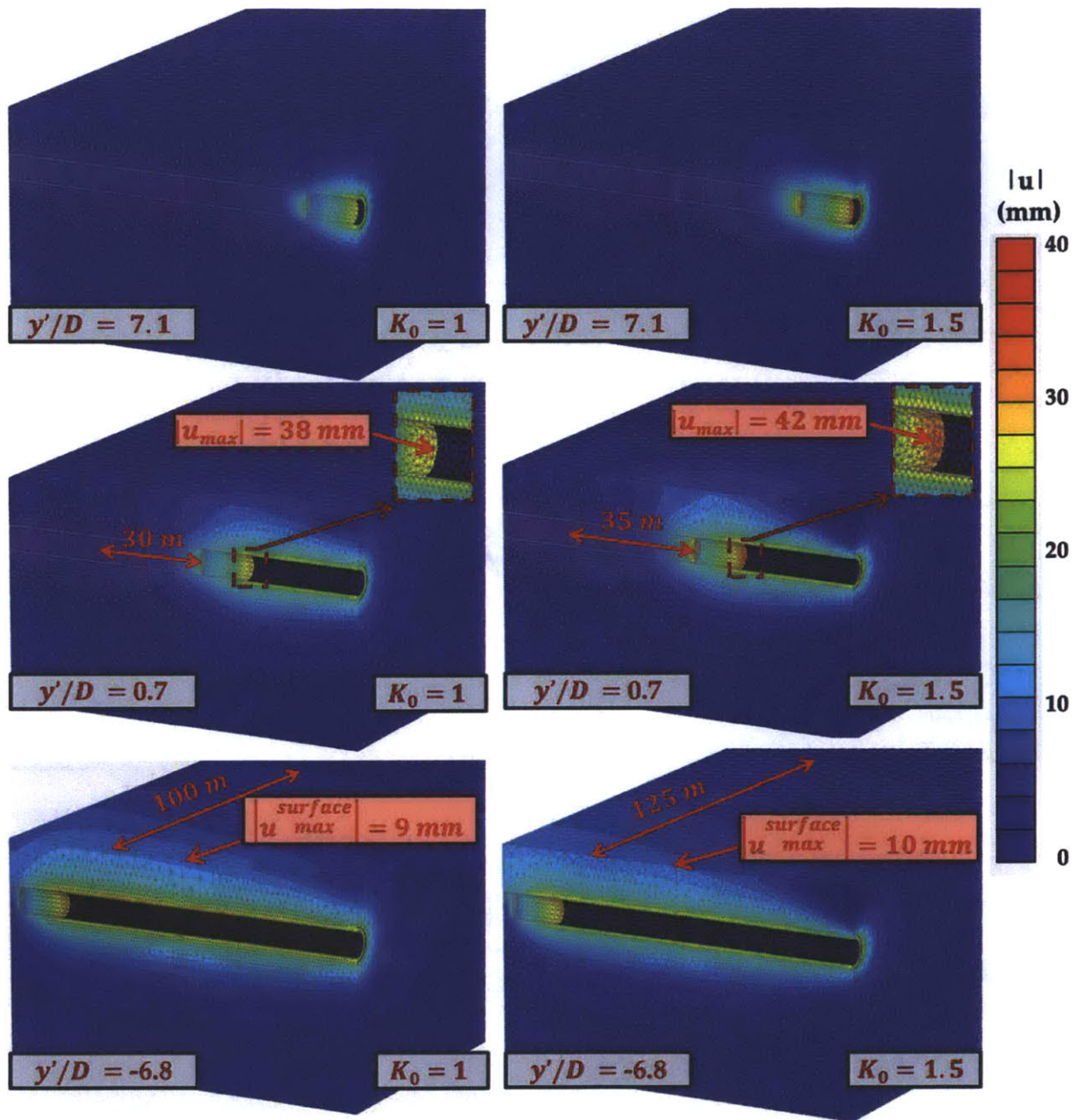


Figure 4.6 Contours of ground displacements  $|u|$  at the three locations of the EPB machine for  $K_0=1$  and  $K_0=1.5$



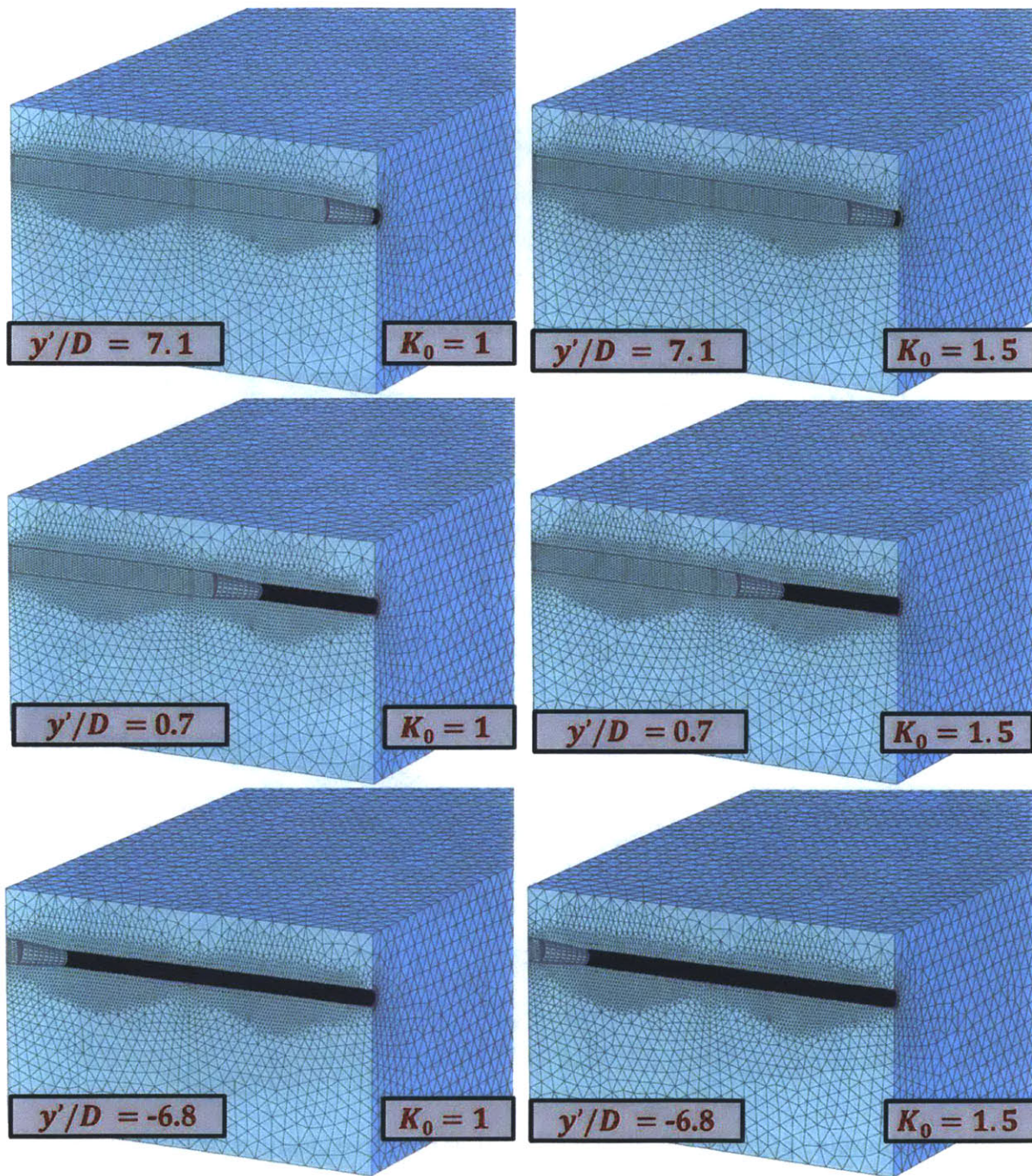
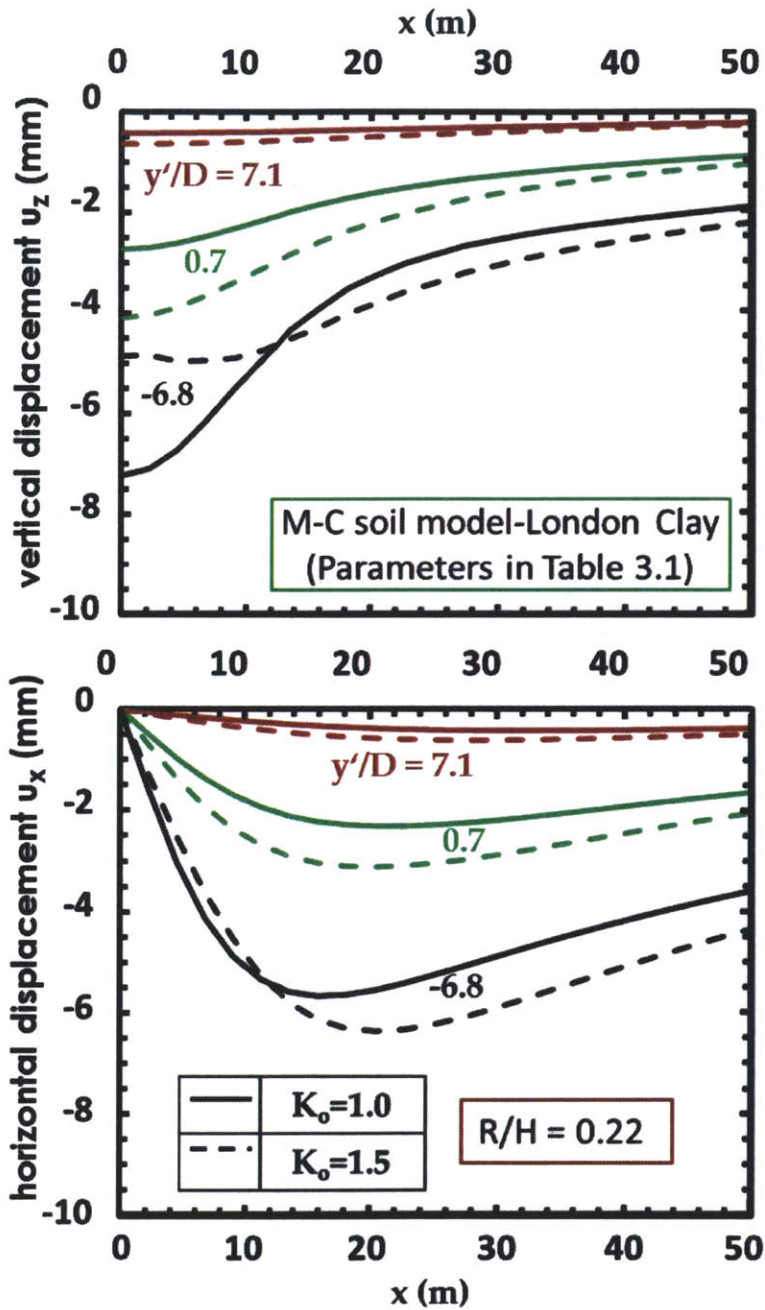


Figure 4.7 Deformed mesh scaled up by 50 times, at the three locations of the EPB machine for  $K_0=1$  and  $K_0=1.5$

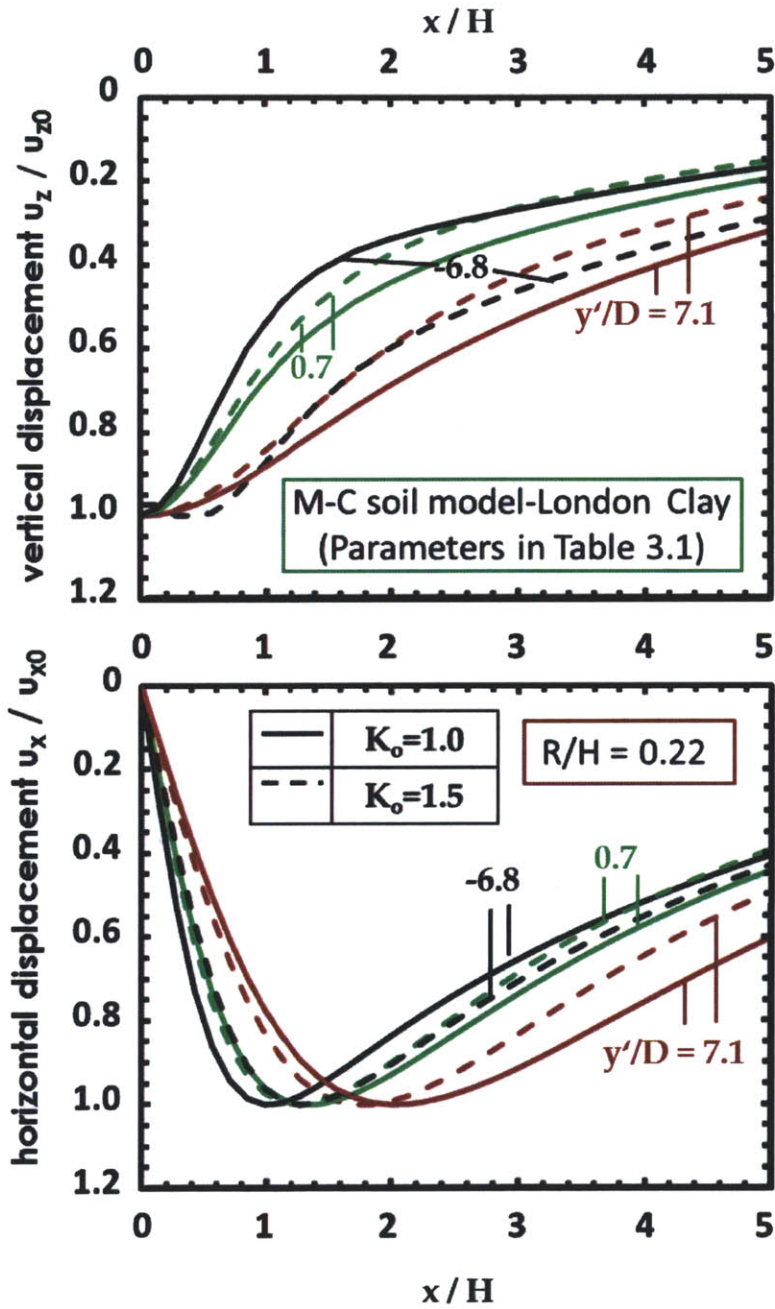


a) Vertical displacement components

b) Lateral displacement components

Figure 4.8 Effect of  $K_0$ -conditions on computed surface deformations at mid-section of the base case FE model simulating EPB tunneling London Clay





c) Normalized vertical displacements

d) Normalized lateral displacements

Figure 4.8. (Cont'd) Effect of  $K_0$ -conditions on computed surface deformations at mid-section of the base case FE model simulating EPB tunneling London Clay

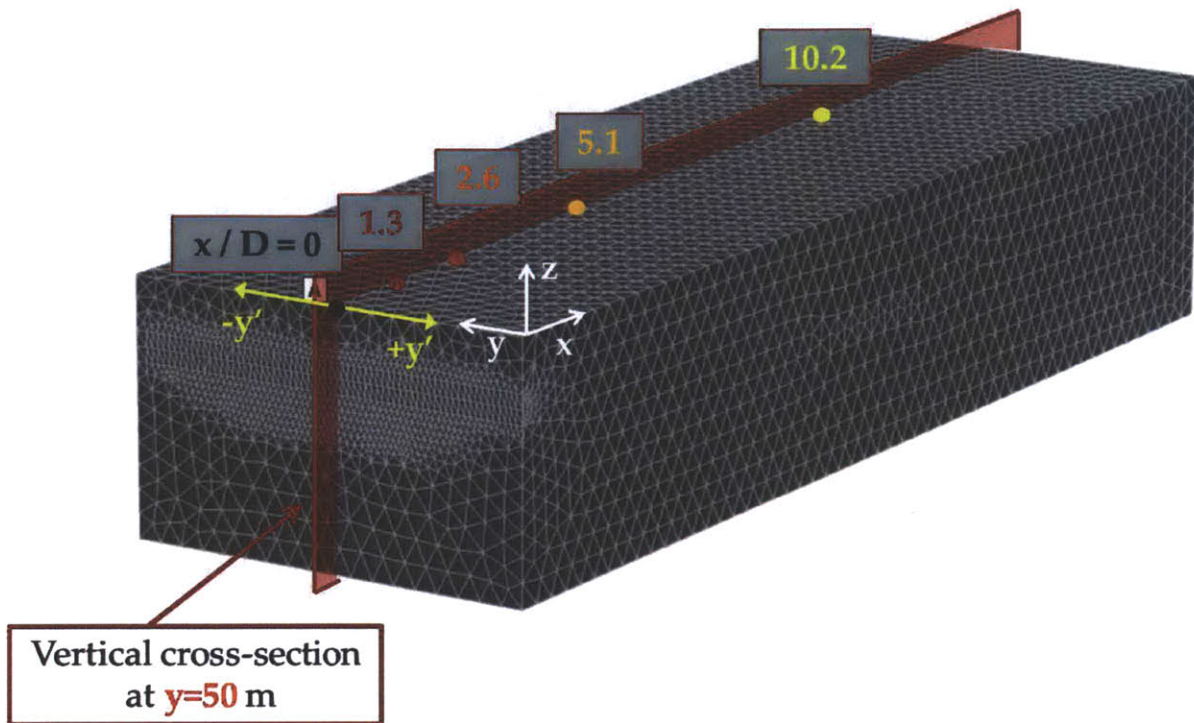


Figure 4.9 Middle-plane ( $y' = 0$ ) and the five selected locations to be examined along the mid-plane

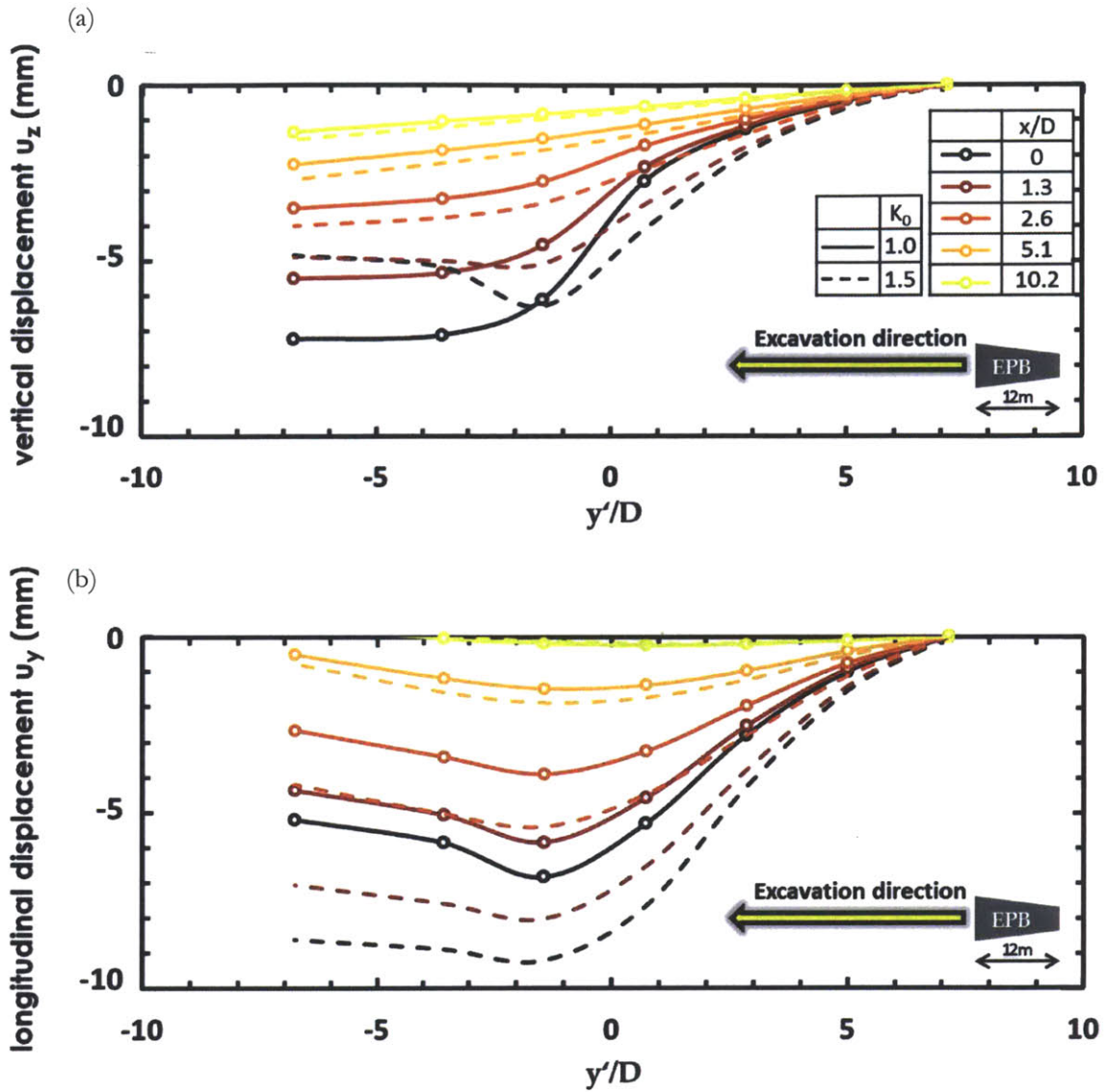
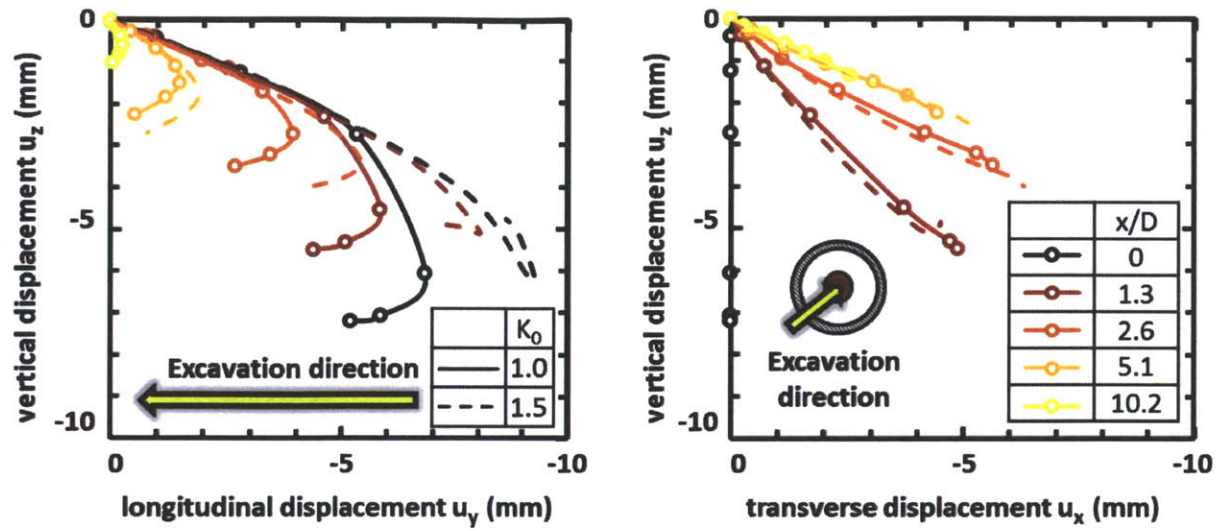


Figure 4.10. Development of surface displacements as functions of the EPB face location at five different locations along the mid-plane of FE model for  $K_0$  1.0 and 1.5 (a) settlements  $u_z$  longitudinal and (b) displacements  $u_y$





a) Displacement vectors in longitudinal planes      b) Displacement vectors in transverse plane

Figure 4.11 Displacement trajectories for surface points along the center-plane of the base case FE model of EPB tunneling in London Clay for  $K_0$  1.0 and 1.5 values

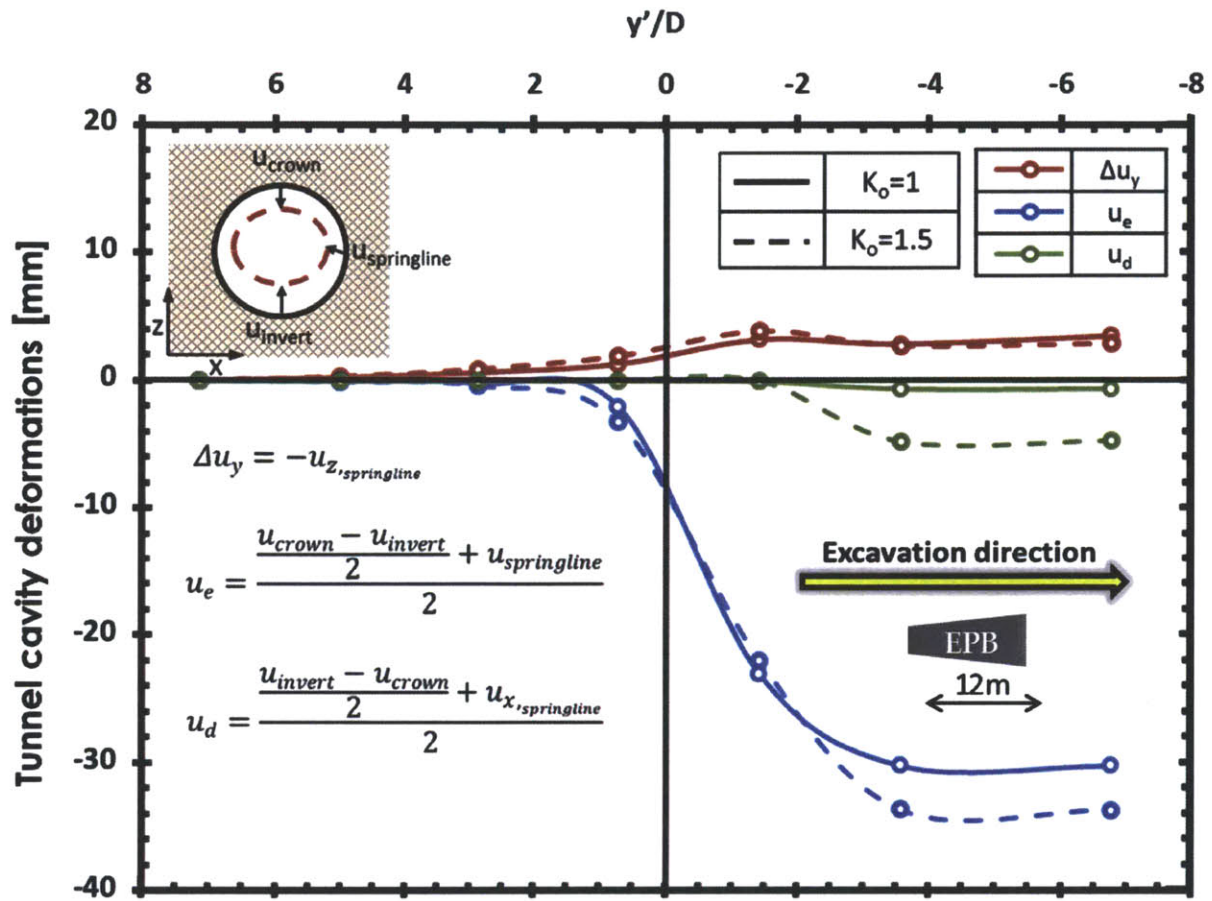
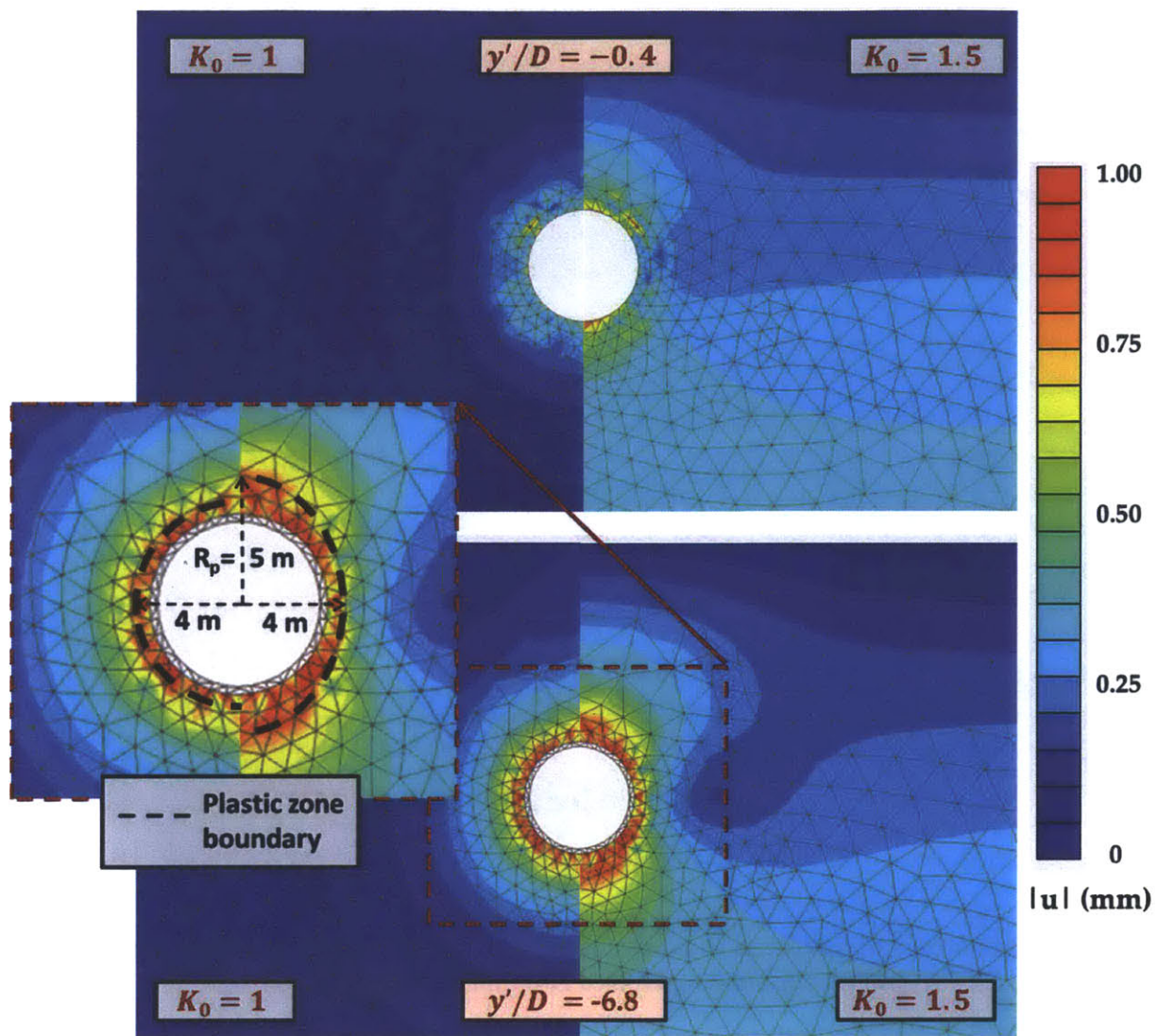


Figure 4.12. Effect of  $K_0$ -conditions on interpreted cavity deformation mode parameters from base case FE model of EPB tunneling in London Clay



a) Plastic zone along the mid plane cross section when the face of the EPB has just passed the examined cross-section ( $y'/D=-0.4$ ) and when the EPB is exiting for  $K_0$  1.0 and 1.5

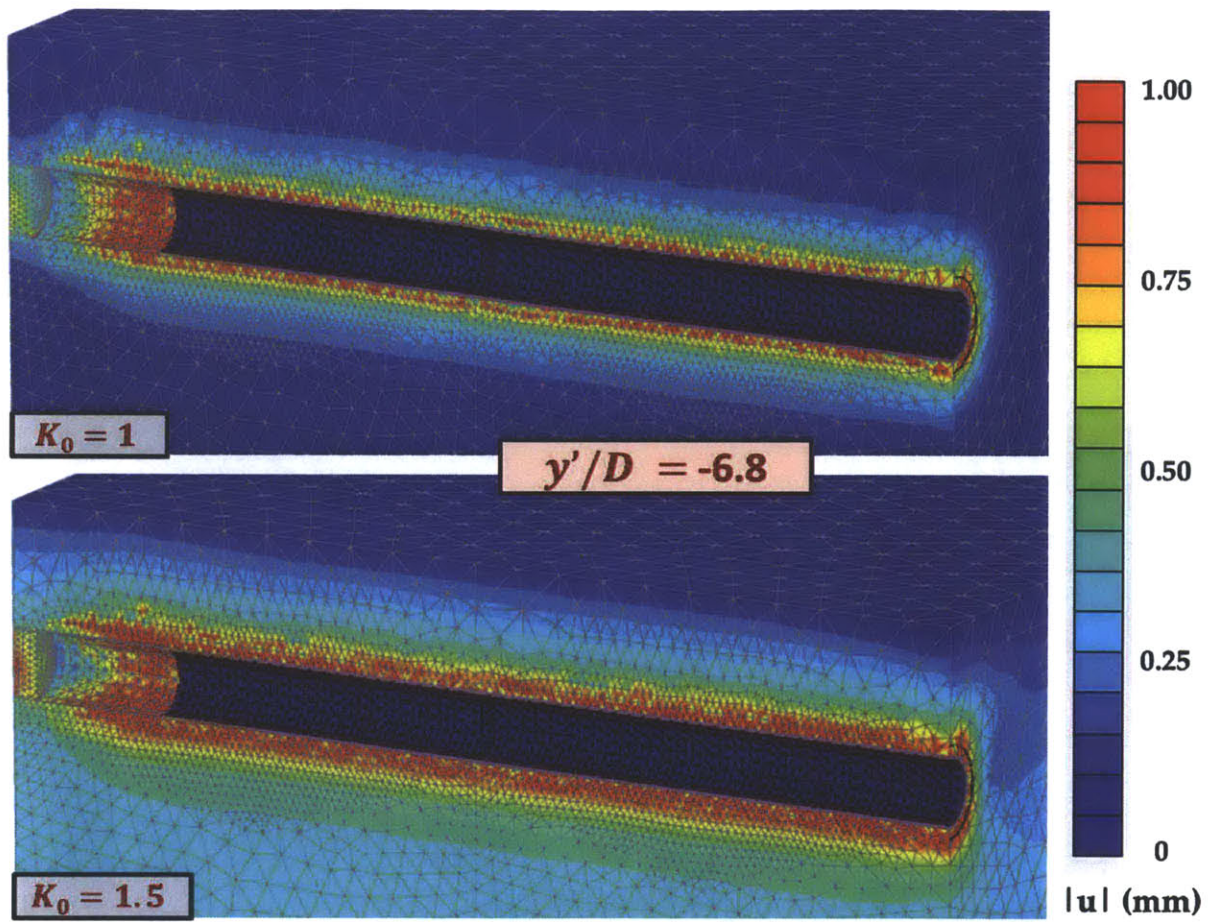


Figure 4.13 Contours of mobilized shear strength  $\tau_{rel}$  showing effect of  $K_0$ -conditions on extent of plastic yielding around EPB tunnel in London clay



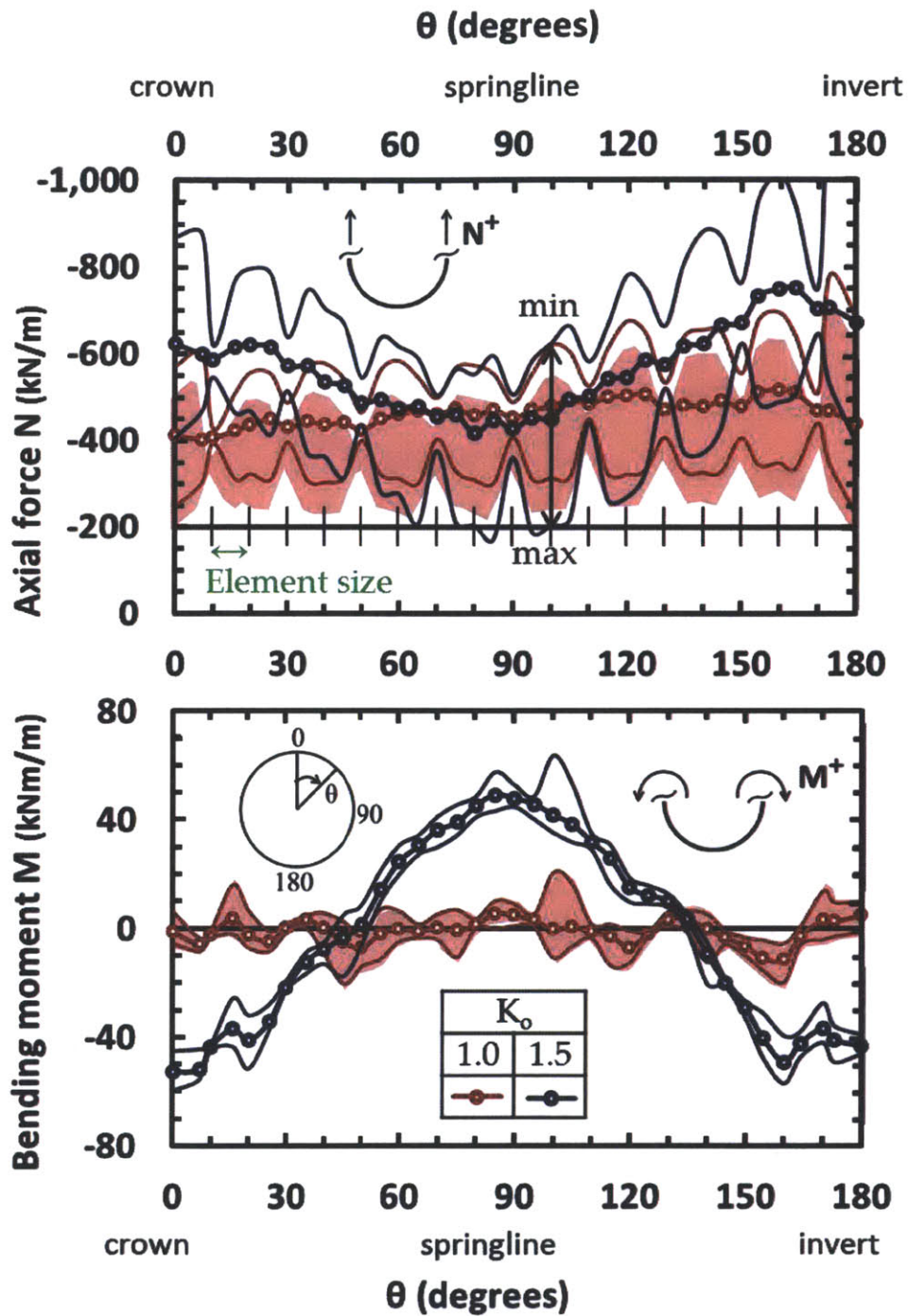


Figure 4.14. Structural forces in linings for  $K_0$  1.0 and 1.5 values, for the lining ring located at the middle plane, after construction process is completed

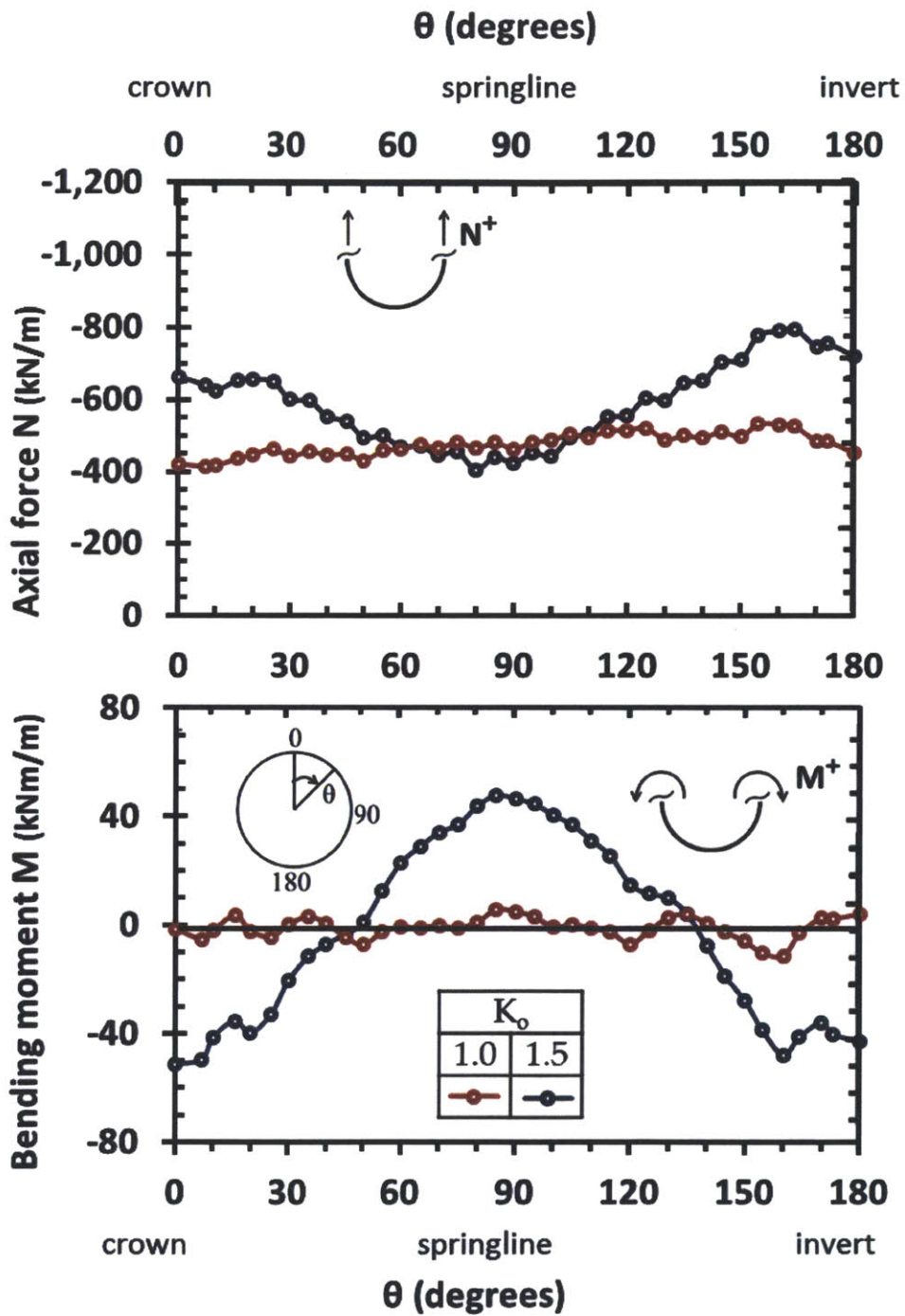


Figure 4.15 Structural forces in linings for  $K_0$  1.0 and 1.5 values, for the lining ring located in the middle plane, when the ring is first activated  $y'/D = -1.9$  and at the end of the construction process  $y'/D = -7$ .

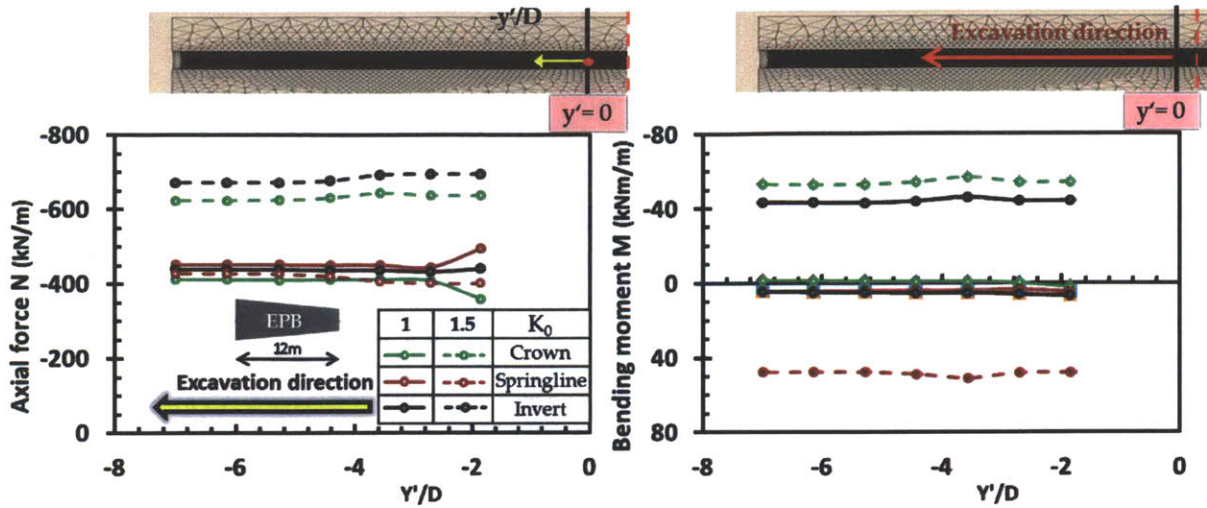


Figure 4.16 Structural forces in lining for crown, springline and invert for the lining ring located at the middle plane ( $y' = 0$ ) for  $K_0=1$  and  $K_0=1.5$  as a function of the EPB position.

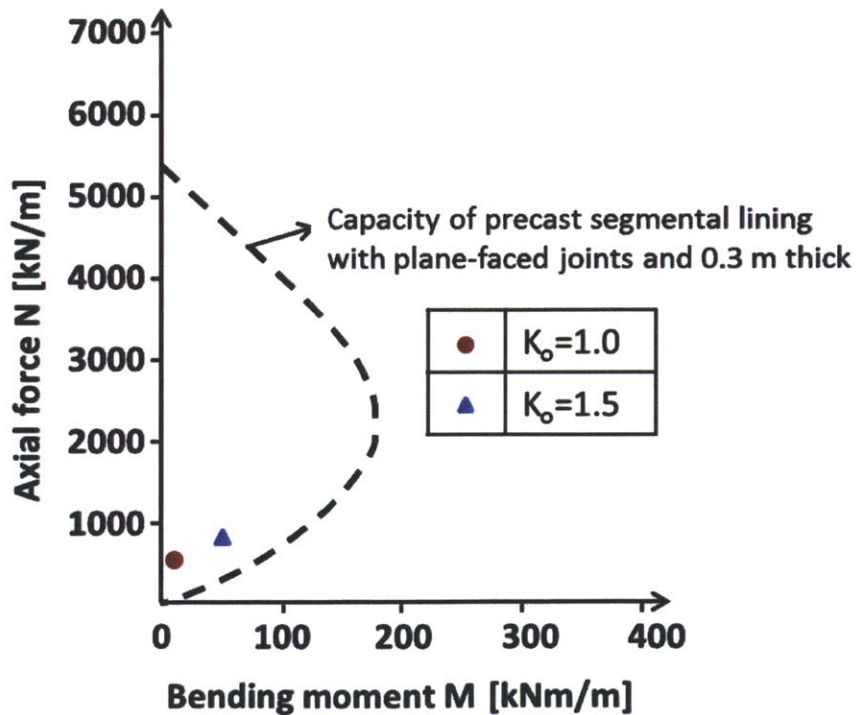


Figure 4.17 Interaction diagram M-N for segmental lining with the values of the computed structural forces in the lining for  $K_0$  1.0 and 1.5 values corresponding to the 3D base case model (source :Iftimie, 1996)

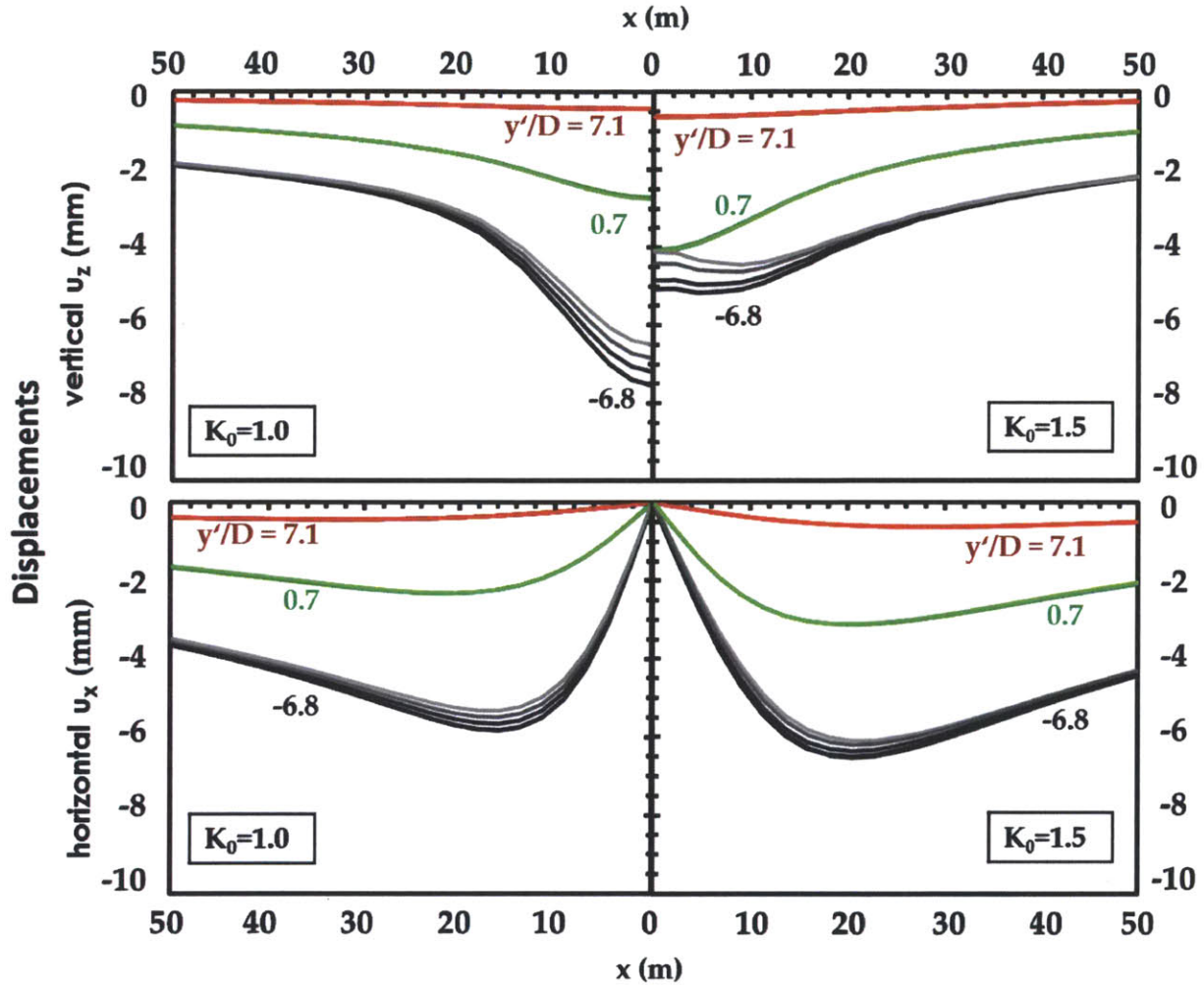


Figure 4.18 Comparison of ground surface deformations at central section of FE model ( $y'=0$ ) for grout pressure 50 to 200 kPa

Grout pressure [kPa]	$y'/D$		
	7.1	0.7	-6.8
50	—	—	—
100	—	—	—
150	—	—	—
200	—	—	—



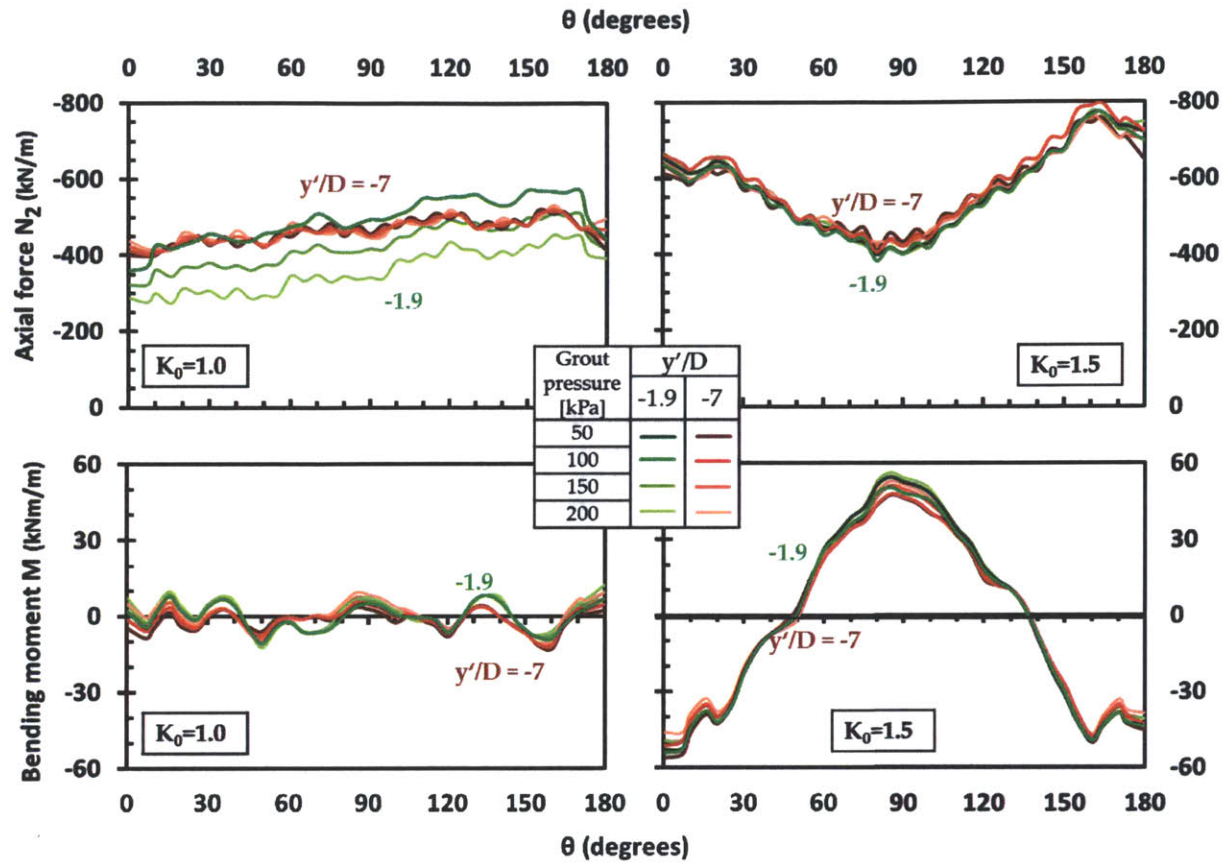


Figure 4.19 Structural forces in the middle ring ( $y' = 0$ ) for  $K_0$  1.0 and 1.5 values at grout pressure 50 to and 200 kPa

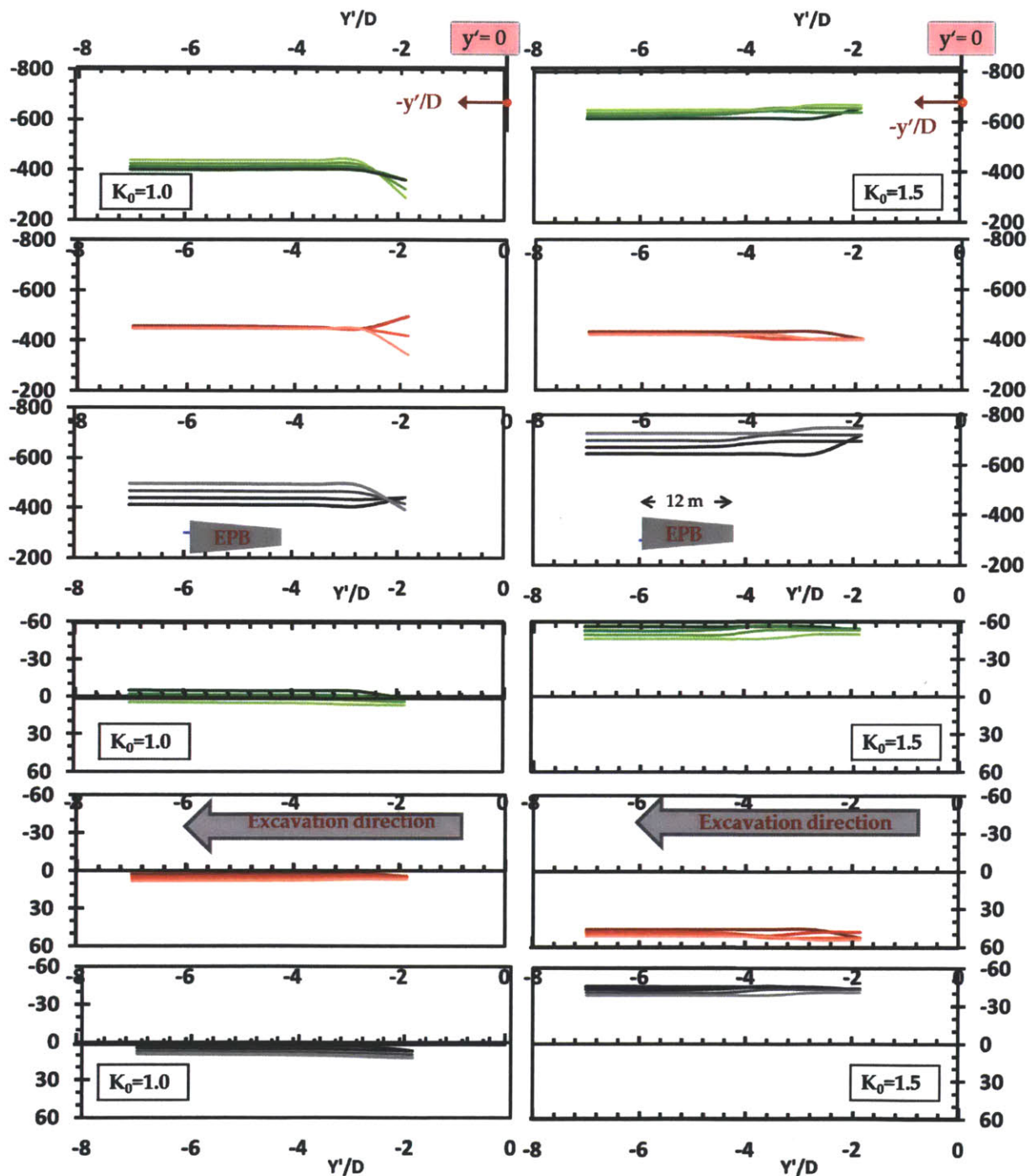


Figure 4.20 Comparison of structural forces as a function of the EPB position, at the crown, springline and invert, for grout pressure 50 kPa to 200 kPa at the middle lining ring, for  $K_0$  1.0 and 1.5 values.

Grout pressure [kPa]	Spring line	Invert	Crown
50	—	—	—
100	—	—	—
150	—	—	—
200	—	—	—

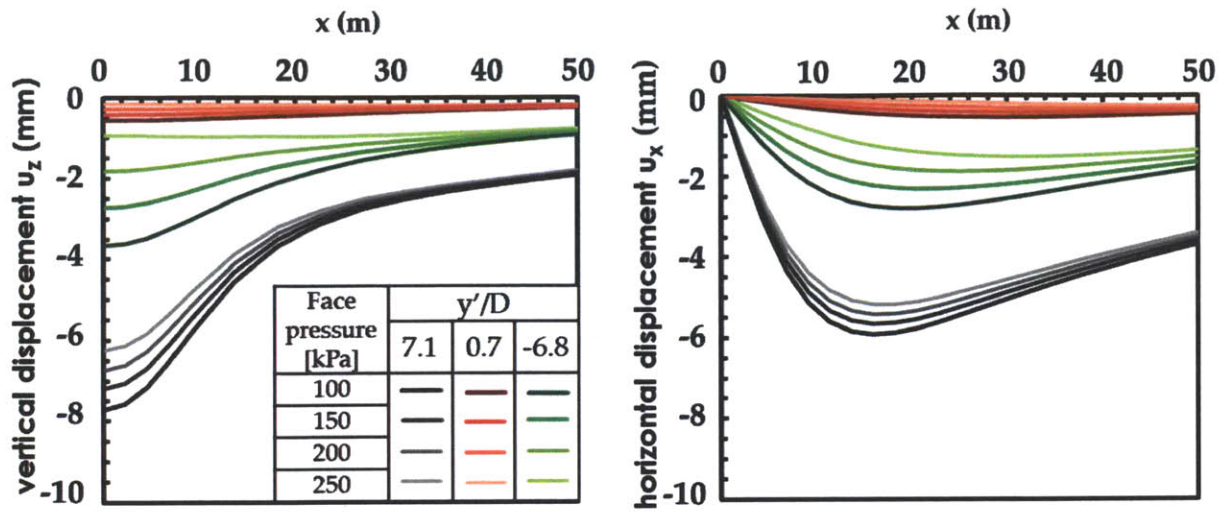


Figure 4.21 Comparison of ground surface deformations at central section of FE model ( $y' = 0$ ) for face pressure 100 to 250 kPa



## 5 Effect of FE assumptions on EPB Tunneling Performance

One of the biggest uncertainties in predicting tunnel performance using FE methods is the representation of the tunneling process itself. The previous chapter has shown results obtained using a sequential model for describing the advance of a 7 m diameter EPB machine in low permeability London clay under the assumption of undrained conditions. Key approximations in this model relate to:

1. Small strain approximation of the excavation process.
2. Simplified boundary conditions at the shield soil interface assuming full contact with prescribed radial displacements, no shear stresses are applied tangential to the interface (i.e the friction in the soil-machine interface is ignored)
3. Tail void is initially represented by a grout pressure for 1.5 m behind the shield and then the already emplaced ring is activated along with the hardened grout.
4. Steering of machine along a defined horizontal trajectory.

### 5.1 Comparison of base case 3D model with KRATOS

It is interesting to compare the 3D base case FE model (created using Plaxis) with a more sophisticated 3D model using Kratos-Ekate software developed by Kasper and Meschke, (2004).

**Figure 5.1** illustrates the different simulation approaches used for each model. The most important feature of the Kratos model is that the TBM is represented as a distinct deformable structure in frictional contact with the soil. The Kratos model can therefore account for

a) the gap formed between the machine and the soil

b) the shear stresses developed at the soil-machine interface and

c) simulate steering of the machine by prescribe non-uniform jack thrusts

In contrast, the base case FE model imposes a displacements boundary condition to represent the conical shape of the shield, assuming there is no gap between the soil and the machine , no friction at the soil-machine interface and advancing of the shield in a horizontal trajectory.

In Kratos, the TBM shield advances through the soil on a specified path using an array of hydraulic jacks. The hydraulic jacks (represented by truss elements) push against the emplaced lining system to steer the machine by controlling the shield orientation. The tunneling construction is model in steps , and each step consists of three stages ( see **Figure 5.2**). In the first stage the jacks are contracted (**Figure 5.2a**), in the second stage the jacks extend pushing the machine forward into the soil **Figure 5.2b** and at the third stage the soil elements from excavation face are removed and the area is re-meshed, connecting the new nodes to the TBM head **Figure 5.2c**. When the TBM has advanced forward by the length of one lining ring, new elements representing the lining are activated and the jack elements now connected to the edge nodes of the new lining. The model can also account for stationarity of the TBM by allowing time increments for the lining ring erection. Although, the base case model in Plaxis

basically uses a similar step wise approach to simulate the tunnel construction, the base case undrained model does not account for time effects. Furthermore, the length of each step has to coincide with the lining ring width, whereas for Kratos the length of each step is freely defined.

The Kratos model uses a fully saturated two-phase material, with a hydrating matrix phase, to represent time-dependent stiffness and permeability of the grout. Additionally, the grout pressure is directly applied to the front face of the solid grout elements, whereas the Plaxis model simulates grouting in a two stage process. It should be noted that although the Kratos model offers advantages in simulating the TBM trajectory, it involves much greater computational complexity.

The two models were compared (Founta et.al., 2013) using the geometry of the Crossrail project as a reference case, assuming undrained conditions with stiffness and strength parameters typical of London Clay. Results are compared in terms of ground surface displacements and the structural forces in the lining for cases with  $K_0 = 1.0$  and  $1.5$ . **Figure 5.3** compares the vertical and horizontal components of surface deformations along the transverse mid-plane of the FE model ( $y' = 0$  m) for different  $K_0$  values (1.0-1.5) at three reference locations of the EPB machine,  $y'/D = 7.1, 0.7$  and  $-6.8$ . It can be seen that both vertical and horizontal displacements of Plaxis and Kratos show good agreement for  $K_0 = 1.0$ , for all the three positions of the machine. This can be attributed to the fact that for  $K_0 = 1.0$ , the main deformation mode of the excavation boundary is uniform convergence. As a result the uniform radially imposed displacement boundary for Plaxis model produces a deformation shape at the

tunnel cavity that is similar to the deformed tunnel cavity shape produced by Kratos, where the excavation boundary freely deforms by means of relaxation of stresses.

In general, the analyses with  $K_0 = 1.5$  produce larger far field settlements ( $x > 15-20$  m) and larger lateral deformations than the analyses with  $K_0 = 1.0$ . While the horizontal displacements are similar for the two FE models, the vertical displacements differ substantially for the  $K_0 = 1.5$  case (for  $x \leq 20 - 30$ m) . This is explained by the fact that deformations of the excavation boundary for  $K_0 = 1.5$  are now described by ovalization as well as uniform convergence modes. The imposed uniform radial boundary displacement conditions used to simulate the shield in Plaxis constrains the ovalization mode, which only develops behind the shield where the soil-grout-lining system is free to deform. In contrast, the Kratos model allows the tunnel cavity to deform freely from the outset. This produces a large difference between  $K_0 = 1.0$  and  $1.5$ . As a result the Kratos model predicts smaller centerline settlements due to passage of the EPB shield ( $y'/D \leq 0.7$  to  $-6.8$ ) with maximum surface settlements occurring at an offset location,  $x = 10 - 15$ m. While these results are readily explained from the numerical models, they have yet to be resolved with respect to real field data.

**Figure 5.4** shows the development of surface settlements as a function of time for the longitudinal mid-plane. For  $K_0 = 1.0$  the surface settlements troughs of the two models are similar. Plaxis predicts larger settlements ahead of the EPB machine since the imposed boundary displacements are larger than the deformations occurring at the tunnel cavity for Kratos model ( that allows the soil to deform freely and the formation of a gap between the soil and the shield). However the final settlements of the two models are comparable at  $y'/D =$



-6.8. There is a significant difference in surface settlements for the  $K_0 = 1.5$  case. It is clear that the ovalization mode is represented in Plaxis, only after the passage of the EPB machine (after 50m advance), where the surface settlement trough starts to diverge from the  $K_0 = 1.0$  case (uniform convergence). In contrast for Kratos, the differences between the two  $K_0$  cases become apparent as the excavation face approaches the examined cross-section, and much smaller settlements are predicted for the  $K_0 = 1.5$  case.

**Figure 5.5** compares the computed structural forces in the lining for the two models after the end of the tunnel construction. The structural forces are plotted for a reference lining ring located at the mid-plane. The results correspond to values averaged first over the ring elements and then over the ring width. It can be seen that the differences in structural forces are negligible for  $K_0 = 1.0$ . As expected, the bending moment is almost zero for  $K_0 = 1.0$  (uniform convergence), whereas for  $K_0 = 1.5$ , the moment is positive for the springline and negative for crown and invert (ovalization). For the bending moment there is a good match between the two models for both  $K_0 = 1.0$  and  $K_0 = 1.5$ . For the axial force, the two models give similar results for  $K_0 = 1.0$ , whereas for  $K_0 = 1.5$  there is a large difference at the springline due to the significant effects of the ovalization mode. The observed mismatch is smaller than expected, due to the small initial stiffness of the grout that allows for significant deformations, absorbing the imposed displacements by the surrounding soil. As a result, only a part of the displacements affects the lining.

In conclusion, we can say that while comprehensive process oriented FE models such as Kratos are clearly superior for representing (and controlling) the advance of a tunnel boring machine,

the predictions of the simpler Plaxis model appear to provide very reasonable predictions of far-field ground deformations and tunnel lining forces.

Table 5.1 Material properties used in FE models

		Material Model	$\rho$ kg/m <sup>3</sup>	E MPa	$\nu$	Su KPa	E <sub>1</sub> /E <sub>28</sub>
Soil	P	Mohr Coulomb	2,000	15+1.1 · z	0.25 <i>(undrained effective stress analysis)</i>	7.5+ 0.55 · z	-
	K	Drucker Prager			0.5		
Grout	P	Kasper 2005	1,500	0.5-100 · 10 <sup>3</sup>	0.18-0.4	-	0.7
	K		2,000	50	0.4		0.65
Lining	P/K	Linear Elastic	2,500	20,000	0.2	-	-
				25,400	0.15		
Machine	P	-	-	-	-	-	-
	K	Linear Elastic	7,600	210,000	0.2	-	-

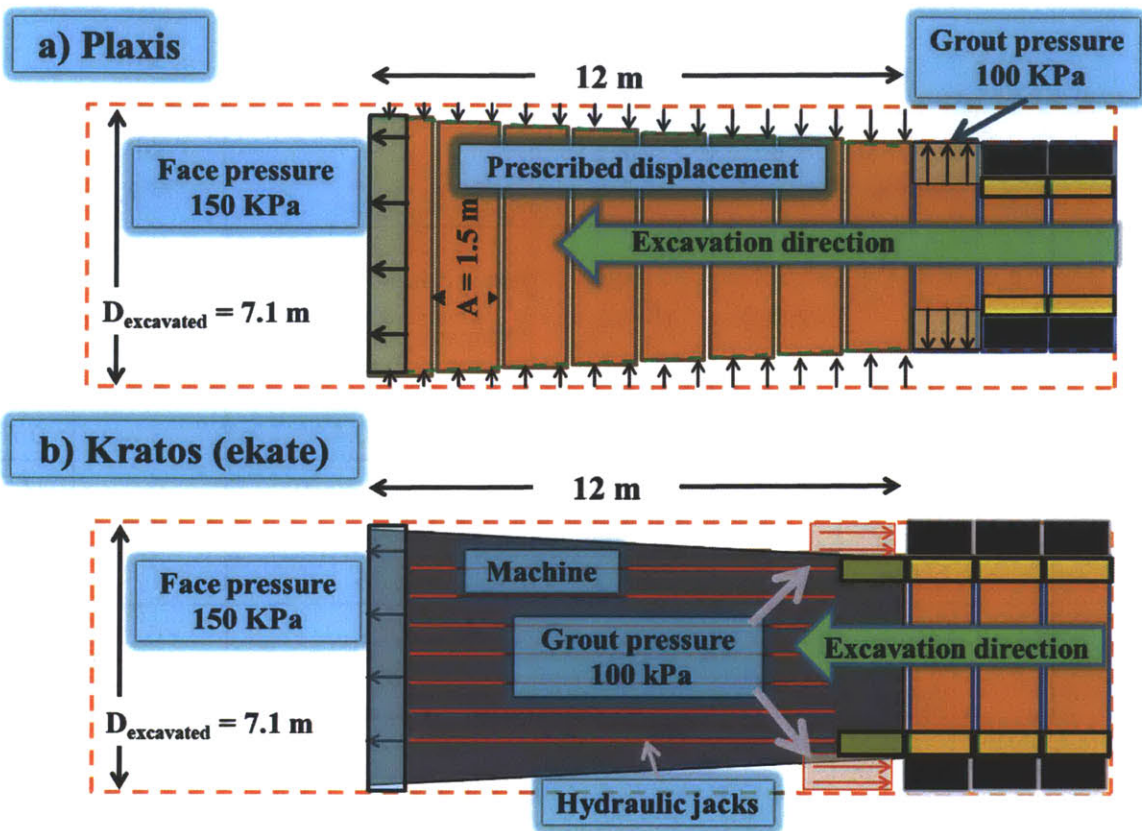


Figure 5.1 Modelling approaches for EPB mechanized tunnelling: a) Plaxis 3D™ b) Kratos-Ekate (source : Whittle et.al, 2013)

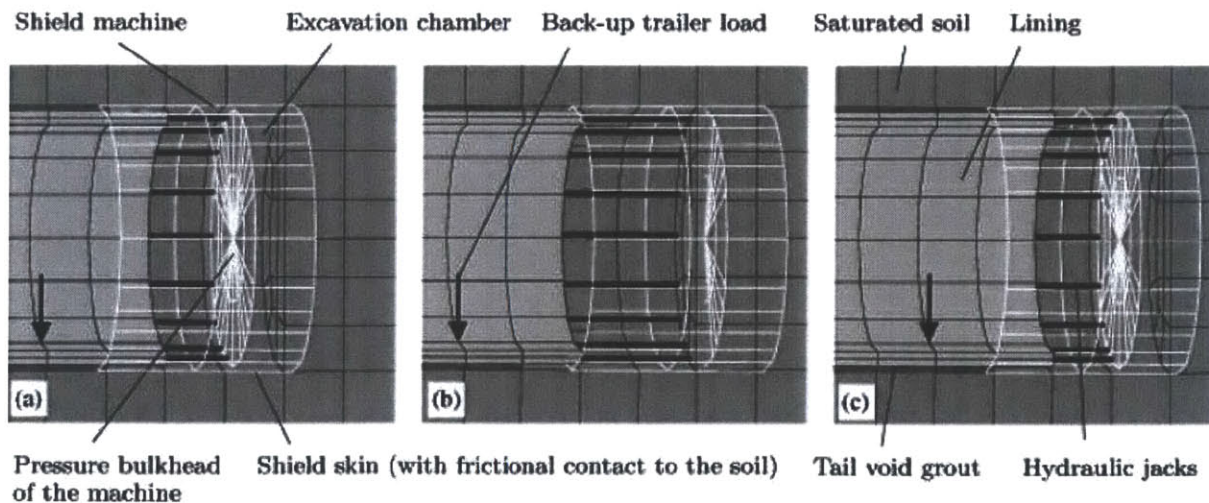


Figure 5.2 3D for closed face tunnelling: Step-by-step simulation procedure: (a) End of previous excavation step; (b) advance of the TBM; and (c) excavation of the soil and introduction of elements representing the tail void grout and the lining. (Kasper and Meschke, 2004)

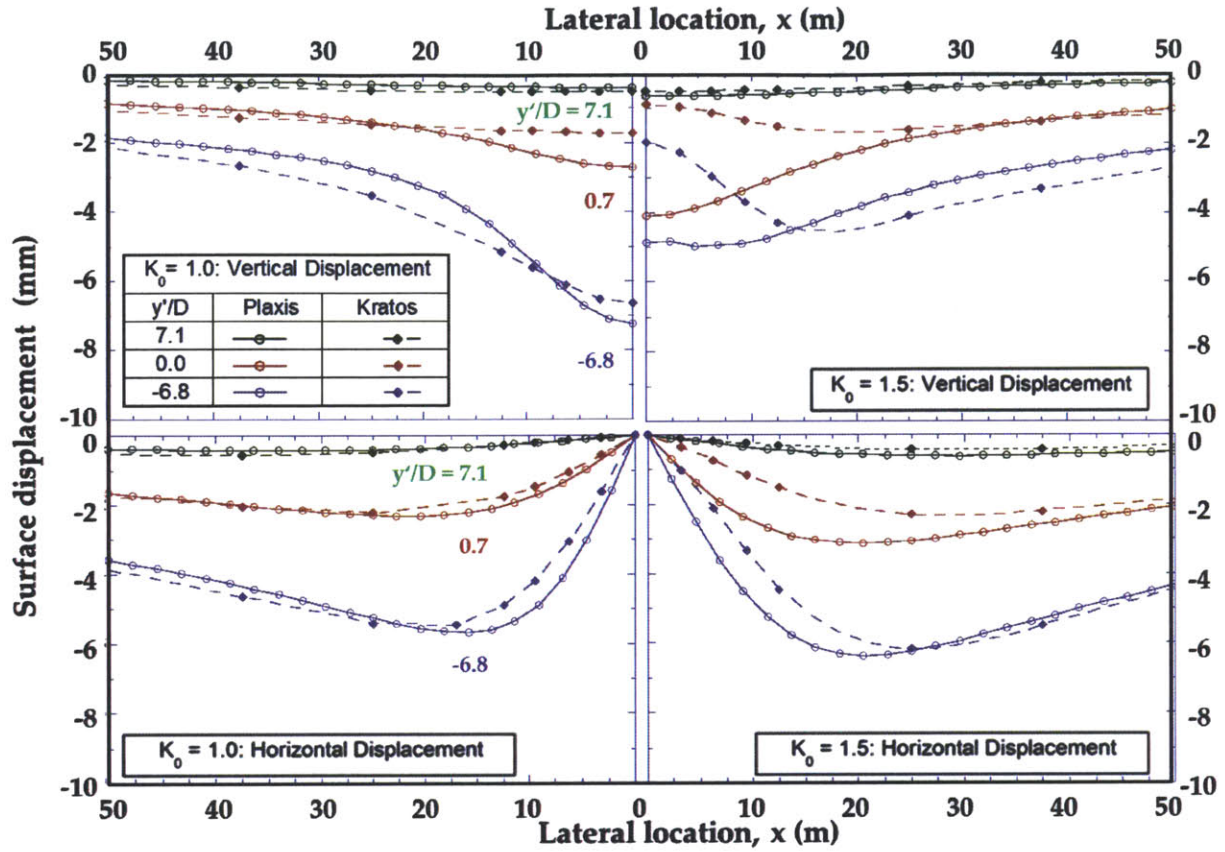


Figure 5.3 Comparison of surface settlements trough for Plaxis and Kratos FE models for different positions of machine with respect to middle cross section (source : Founta et.al, 2013)

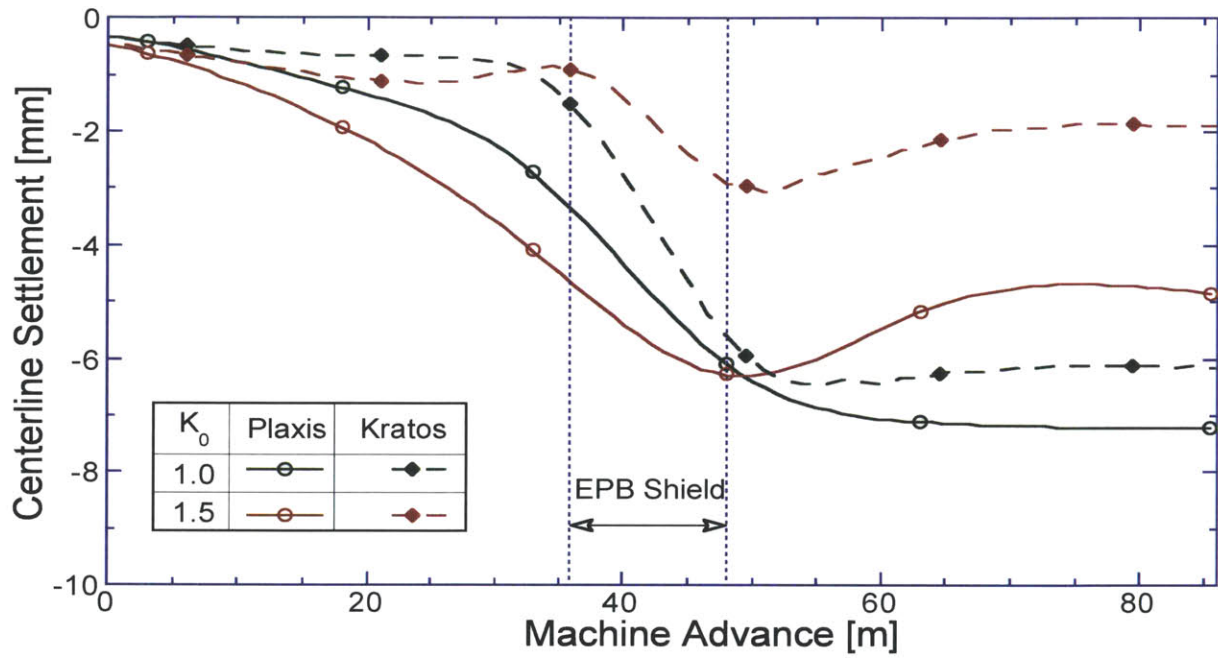


Figure 5.4 Comparison of surface settlements trough for Plaxis (P) and KRATOS (K) model for different positions of machine with respect to middle cross section



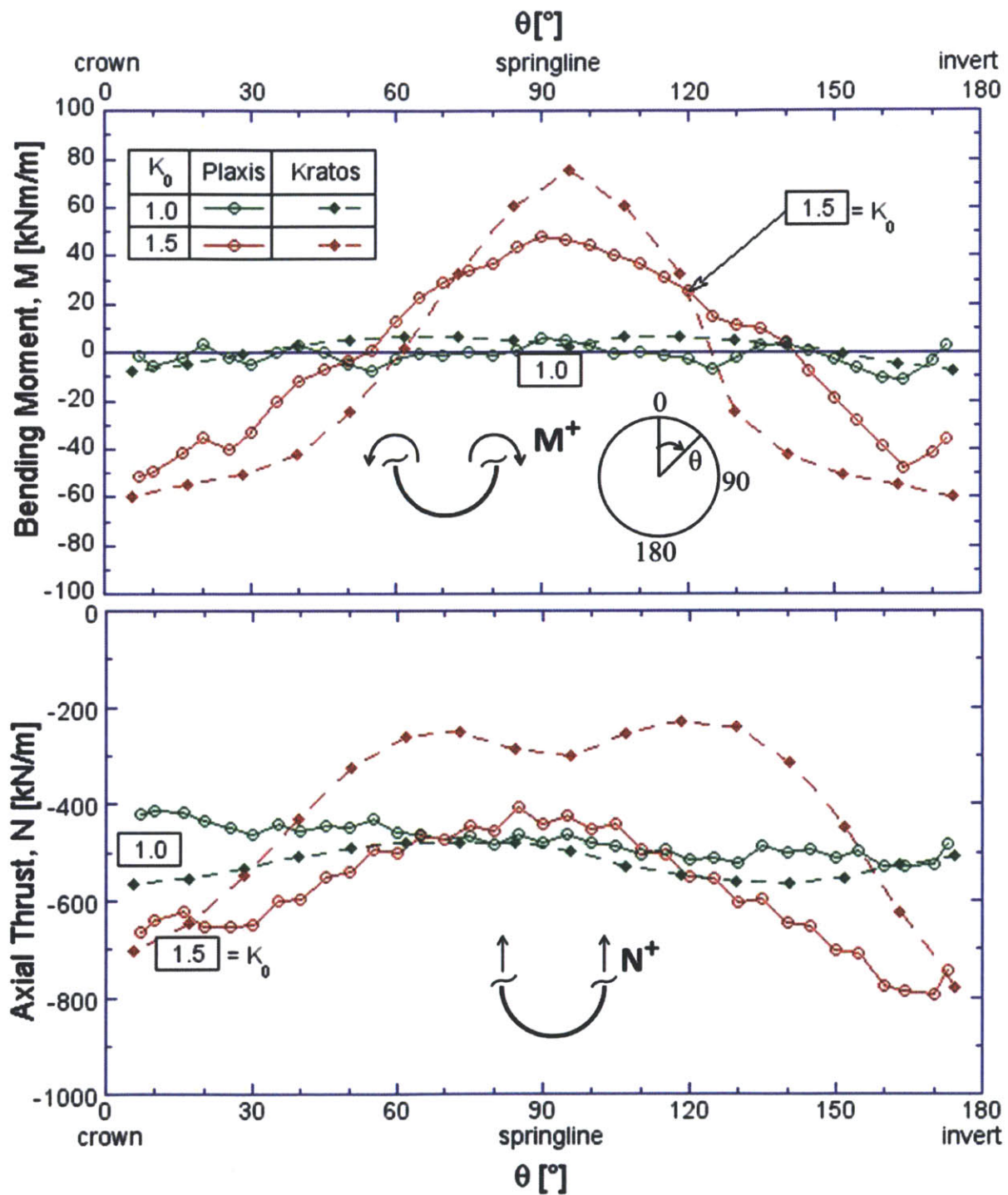


Figure 5.5 Structural forces in linings for two different modelling approaches and  $K_0$  values, for the lining ring in the middle after construction process is completed





## 6 Summary, Conclusions and Recommendations

The main goal of this study was to develop, validate and interpret a model for predicting ground movements caused by mechanized tunnel construction using an EPB machine in clay. For this purpose 2D and 3D numerical simulations were employed to investigate the effect of the mechanized tunnel excavation on ground settlements and structural forces in the lining. The Crossrail project, that is currently under construction, in central London, was considered as a reference case (**Figure 1.9**). The results obtained for the 3D base case model (**Figure 4.2**) allowed us to observe the 3D shape of the settlement trough, the yielding zone and the effect of the soil properties and input construction parameters (e.g., face , grout pressure) on the observed displacements as well as the structural stresses of the lining.

Initially, a simple elastic 2D model was created and the computed results were compared and matched with the existing analytical solutions (Verruijt, 1997; Pinto and Whittle, 2013) to confirm that the model dimensions were appropriate, ensuring accurate representation of far field ground movements. A slightly modified 2D model tunnel construction (using the stress reduction method/ $\beta$ -method) was used to observe how the trough shape and the magnitude of the surface displacement are affected by the soil properties (i.e, strength and stiffness) and the  $\beta$ -value. After that more complex numerical simulations were performed.

Initially, 3-D FE models were compared with 2D cases for unsupported tunnel construction. These results established the lateral boundary location and mesh density necessary to achieve

numerically accurate calculations. Thereafter a base case FE model (**Figure 4.2**) was developed for simulating mechanized tunnel construction using an Earth Pressure Balance (EPB) machine.

The results for the base case EPB tunnel construction showed that the analyses with  $K_0 = 1.5$  produce larger far field settlements ( $x > 15\text{-}20\text{m}$ ) and smaller lateral deformations than the analyses with  $K_0 = 1.0$ . There is also an important switch in the shape of the settlement trough for  $K_0 = 1.5$  as the tunnel face passes the mid-plane ( $y'/D = 0.7$  to  $-6.8$ ; **Figure 4.8b** and **c**), such that the maximum settlement is offset from the centerline and much smaller settlements occur at locations close to the centerline ( $x < 15\text{m}$ ). The computed structural forces in the lining, for  $K_0 = 1.0$  show that axial compression is almost constant throughout the ring with negligible bending moment. For  $K_0 = 1.5$  the ovalization mode induces significant bending moment around the ring.

In order to estimate the effects of key input parameters in the obtained results, parametric analyses were conducted to assess the influence of face pressure and grout pressure. The results indicated that the deviation in the face pressure starts to affect the surface displacements as the EPB approaches the monitored section. When the EPB has finally reached this section, the effect is maximized. Finally, as the machine advances forward, the face pressure effect reduces by a factor of two. The grout pressure has only a minor influence on the surface settlements or computed structural forces.

The 3D base case FE results were compared with a more sophisticated 3D model using Kratos-Ekate software developed by Kasper and Meschke, (2004). The two finite element models produce quite similar predictions of surface deformations and lining forces for the  $K_0 = 1.0$  case

However for  $K_0 = 1.5$ , while the horizontal displacements were similar for the two FE models, the vertical displacements differed substantially (for  $x \leq 20 - 30\text{m}$ ). The difference was attributed to the inability for the Plaxis model to capture the introduced ovalization mode shape at the soil-shield boundary. In terms of lining forces the two analyses were comparable for both  $K_0$  cases, although Kratos tends to predict smaller axial thrusts and larger bending moments at the springline for  $K_0 = 1.5$  than Plaxis. While comprehensive process oriented FE models such as Kratos are clearly superior for representing (and controlling) the advance of a tunnel boring machine, the predictions of the simpler Plaxis model appear to provide very reasonable predictions of far-field ground deformations and tunnel lining forces.

Although, the 3-D FE model presented in this thesis can be characterized as sufficient for typical tunnel projects, it can be further expanded for a more accurate representation of the excavation procedure. The next stages of development will consider more realistic constitutive modeling of soil behavior, coupled flow and deformation effects, shield-soil interface traction, the possible existence of a gap between the shield and the surrounding soil, steering effects, over excavation, soil-structure interaction etc. These additional complexities are expected to increase the computational time significantly and thus must be evaluated carefully. Another interesting aspect of this problem is the validation of this numerical model using field data of monitored cross-sections modeling interactions of the tunnel with overlying structures.



## 7 References

- [1] Van der Stoel A.E.C , Van Ree, H.J. (2000) “Strength and stiffness parameters of jet grouting columns : Full scale test Amsterdam”, International Conference on Geotechnical and Geological Engineering, Melbourne Australia, GIGS0268
- [2] Attewell, P. B. (1978) “Ground movements caused by tunneling in soil”, Proc. International Conference on Large Movements and Structures, J.D. Geddes (Ed), Pentech Press, London, 812-948
- [3] Attewell, P. B. and Woodman, J. P. (1982) “Predicting the dynamics of ground settlement and its derivatives caused by tunneling in soil”, *Ground Engineering*, 15(8), 13-22, 36
- [4] Attewell, P. B. Yeates,J., Selby A.R. (1986) “Soil movements induced by tunnelling and their effects on Pipelines and structures”, Blackie,Glasgow
- [5] Bam Ferrovia Kier ,BfK (2012) “Status Report 2-Component grouting”
- [6] Bernat, S., Cambou, B. (1996) “Soil-structure interaction in shield tunnelling in soft soil”, *Computers and Geotechnics*, 22 (3/4), 221–242, 1998.
- [7] Black, M. (2012) “Crossrail: Geotechnical Sectional Interpretative Report1&2:Royal Oak to Liverpool Street”
- [8] Clayton, C. R. I, Van Der Berg, J. P., Thomas, A. H.(2006) “Monitoring and displacements at Heathrow Express Terminal 4 station tunnels”, *Géotechnique*, 56(5), 323 –334
- [9] Clough, G. W. and Leca, E. (1989) “With focus on use of finite-element methods for soft ground tunnelling”, Review Paper in *Tunnels et Micro-Tunnels en Terrain Meuble-du Chantier a la Theorie*, Presse de l’Ecole National des Ponts et Chaussees, Paris, 531-573
- [10]Cooper, M. L. ,Chapman , D. N., Rogers, C. D. F. , Chan, A. H. C. (2002) “Movements in the Piccadilly Line tunnels due to the Heathrow Express construction”, *Géotechnique*, 52( 4), 243 –257
- [11]Deane, A. P., and Bassett, R. H. (1995) “The Heathrow Express Trial Tunnel”. *Proceedings of the Institution of Civil Engineers, Geotechnical Engineering*, 113, 144-156.
- [12]Dias, D., Kastner, R., Maghazi, M. (1999) “Three dimensional simulation of slurry shield tunnelling”, *Geotechnical aspects of underground construction in soft ground*, Tokyo, Rotterdam: Balkema; 351–6
- [13] FHWA (2011) “Technical Manual for Design and Construction of Road Tunnels - Civil Elements”, <http://www.fhwa.dot.gov/>, U.S. Department of Transportation Federal Highway Administration, Bridge, Tunnels, Chapter 6, 7 and 9
- [14]Founta V., Ninic J., Whittle, A.J., Meschke G., Stascheit J.(2013) “Numerical Simulation of Ground Movements Due To EPB Tunnelling in Clay” 3<sup>rd</sup> EURO:TUN conference:

Computational Methods in Tunneling and Subsurface Engineering, Bochum Germany, in print.

- [15] Franzius, J. N., Potts, D.M. and Burland, J.B. (2005) "The influence of soil anisotropy and  $K_0$  on ground movements resulting from tunnel excavation," *Géotechnique*, 55(3), 189-199.
- [16] GCG (2010) "Geotechnical Sectional Interpretative Report 1&2: Royal Oak to Liverpool Street, Volumes 1 and 2 Report" (No. 1D0101-G0G00-00549 and No. 1D0101-G0G00-00550)
- [17] Greenwood, J.D. (2003) "Three dimensional analysis of surface settlement in soft ground tunnelling", MEng Thesis, Dept. of Civil & Environmental Engineering, Massachusetts Institute of Technology
- [18] Ieronymaki, E. (2011) "Response of continuous pipelines to tunnel induced ground deformations", MSc Thesis, Dept. of Civil & Environmental Engineering, Massachusetts Institute of Technology
- [19] Iftimie, T. (1996) "Contributions to the concept and structural analysis of precast circular linings for shield driven tunnels", PhD Thesis, Technical University of Civil Engineering Bucharest
- [20] ITA (2004) "Underground or aboveground? Making the choice for urban mass transit systems: A report by the International Tunnelling Association (ITA). Prepared by working group number 13(WG13). Direct and indirect advantages of underground structures", *Tunnelling and Underground Space Technology*, 19(1) 3-28
- [21] Kasper, T., Meschke, G. (2004) "A 3D finite element model for TBM tunnelling in soft ground" *International Journal for Numerical and Analytical Methods in Geomechanics*, 28, 1441-1460
- [22] Kasper, T., Meschke, G. (2006) "On the influence of face pressure, grouting pressure and TBM design in soft ground tunnelling", *Tunnelling and Underground Space Technology*, 21 (2), 160-71
- [23] Komiya, K., Soga, K., Akagi, H., Hagiwara, T., Bolton, M. (1999) "Finite element modelling of excavation and advancement processes of a shield tunnelling machine", *Soils and Foundations*, 39 (3), 37-52
- [24] Layman, R. (2011) "Short term vs. long term thinking: transit, the Washington Examiner, Fairfax/Loudoun Counties vs. DC", <http://urbanplacesandspaces.blogspot.com/>
- [25] Laver, C.A. (1970) "The demand of urban mass transportation", *The Review of Economics and Statistics*, 52(3), 320-323
- [26] Machi, B. (2004) "NATM industrial method", Geo-Environmental Laboratory, Nagasaki University, <http://www.cee.nagasaki-u.ac.jp/~jiban/text/method/met19/met19.html>

- [27]Maidl, B., Herrenknecht, M., Anheuser, L. (1996) "Mechanised Shield Tunnelling", John Wiley & Sons, Technology & Engineering
- [28]Mair, R. J., Gunn, M. J. and O'Reilly, M.P. (1981) "Centrifuge testing of model tunnels in soft clay", Proc. 10th International Conference on Soil Mechanics and Foundation Engineering, Stockholm, Balkema, 1,323-328
- [29]Mair, R. J., Taylor, R. N. and Bracegirdle, A. (1993) "Subsurface settlement profiles above tunnels in clay", *Geotechnique*, 43 (2), 315-320
- [30]Mair, R.J. , Taylor, R.N.,Burland, J.B. (1996) "Prediction of ground movemetns and assessment of risk of buildings damage due to bored tunnelling , In : Mair, R.J. and Taylor R.N (eds), Geotechnical aspects of underground construction in soft ground, Proc. Int. Symp.,London, Rotterdam: Balkema
- [31]Mair, R.J. and Taylor, R.N. (1997) "Board tunneling in the urban environment", Proc. 14th International Conference on Soil Mechanics and Foundation Engineering, Hamburg, Balkema, 2353-2385
- [32]Mair, R.J. (1999) "Design and construction of tunnels in soft ground",Proceedings of the XIIth European Conference on Soil Mechanics and Geotechnical Engineering, Amsterdam, 3, 1915-1921
- [33]Melis, M. (1997) "A selection and specifications of the EPB tunnelling machines for the Madrid Metro extension", Jornadas Tecnicas sobre la ampliacion del Metro de Madrid. Fundacion AgustÅn de Bethencourt y Comunidad de Madrid, Madrid, (1)
- [34]Merritt, A.S., Mair, R.J. (2008) "Mechanics of tunnelling machine screw conveyors: a theoretical model" *Géotechnique*, 58(2), 79-94.
- [35]Möller S. (2006) "Tunnel induce settlements and structural forces in linings", PhD Thesis, Institute fur Geotechnik der Universitat Stuttgart
- [36]Net Resources International (2012) "Amsterdam Metro North-South line, Netherlands", [http://www.railway-technology.com/projects/ns\\_metro/](http://www.railway-technology.com/projects/ns_metro/)
- [37]NFM Technologies "Soft ground machines", <http://www.nfm-technologies.com/-Soft-ground-machines-.html>
- [38]Nyren, R. J. (1998), "Field measurements above twin tunnels in London Clay," PhD thesis, Imperial College, University of London.
- [39]Peck, R. B. (1969) "Deep excavations and tunneling in soft ground", Proc. 7th International Conference on Soil Mechanics and Foundation Engineering, Mexico City, State of the Art Volume, 225-290
- [40]Pinto, F. (1999) "Analytical methods to interpret ground deformations due to soft ground tunneling", MSc Thesis, Dept. of Civil & Environmental Engineering, Massachusetts Institute of Technology

- [41]Pinto, F., Zymnis, D. M. and Whittle, A. J. (2013) "Ground movements due to shallow tunnels in soft ground: 2. Analytical interpretations and predictions", to appear in *ASCE Journal of Geotechnical and Geoenvironmental Engineering*
- [42]Pinto, F. and Whittle, A. J. (2013) "Ground movements due to shallow tunnels in soft ground: 1. Analytical solutions", to appear in *ASCE Journal of Geotechnical and Geoenvironmental Engineering*
- [43]Potts, D.M., Addenbrooke, T.I. (1997) "A structure's influence on tunnelling-induced ground movements", *Geotechnical Engineering*, ICE, 125(2), 109-125.
- [44]Sagaseta, C. (1987) "Analysis of undrained soil deformation due to ground loss", *Geotechnique*, 37 (3), 301-320
- [45]Salvucci, F.P. (2003) "The "Big Dig" of Boston, Massachusetts: lessons to learn", 29<sup>th</sup> ITA World Tunnelling Congress, Amsterdam, Claiming the Underground Space, Vol 1 and 2, 37-41
- [46]Savidis, S. A., and Rackwitz, F. (2004) "Geotechnical and environmental consideration by planning and construction of the transportation infra-structure in the centre of Berlin." "Proc., 5th Int. Conf. on Case Histories in Geotechnical Engineering , Paper 5.32, University of Missouri-Rolla, Rolla, MO
- [47]Selemetas D. (2006) "The response of full-scale piles and piled structures to tunnelling", PhD Thesis, University of Cambridge
- [48]Schmidt, B. (1969) "Settlement and ground movement associated with tunnelling in soils", PhD Thesis, University of Illinois, Urbana
- [49]Sloan, S.W., Randolph, M.F., (1982) "Numerical prediction of collapse loads using finite element methods", *Int. J. Num. Analy. Meth. Geomech.* 6, 47-76
- [50]Standing, J.R., Burland, J.B. (2006)"Unexpected tunnelling volume losses in the Westminster area, London," *Géotechnique*, 56(1), 11-26.
- [51]Swoboda, G., Abu-Krishna (1999), "Three-dimensional numerical modelling for TBM tunnelling in consolidated clay", *Tunnel Undergr Space Technol*, 14, 327–333
- [52]Talmon A.M, Bezuijen, A. (2002) "Muck discharge by the screw conveyor of an EPB Tunnel Boring Machine", Proceedings of 3<sup>rd</sup> International Symposium on Geotechnical Aspect of Underground Construction in Soft Ground, Toulouse, 1, 89-94
- [53]Verruijt, A. (1997) "A complex variation solution for a deforming tunnel in an elastic half-plane", *International Journal for Numerical and Analytical Methods in Geomechanics*, 21, 77-79
- [54] Whittle A.J., Sagaseta, C. (2003) "Analyzing the effects of gaining and losing ground," *Soil Behavior and Soft Ground Construction*, ASCE GSP No. 119, 255- 291
- [55]Wong, PB (2004) "Recommended Tunnel Construction Methods Study", Working Paper, Rev. 0



- [56] Woods, E., Batty, Bowers, K., Mimmagh, F. (2007) "Channel tunnel Rail Link section 2: London tunnels", *Proceedings of the ICE - Civil Engineering*, 160(6), 24–28
- [57] Zymnis, D.M., Chatzigiannelis, I. & Whittle, A.J. (2013) "Analytical interpretation of ground movements caused by JLE tunnel construction in St James Park," to appear, *Géotechnique*.
- [58] Zymnis, D. M., Whittle, A. J., & Pinto, F. (2013) "Ground Movements due to shallow tunnels in soft ground: 2. Analytical interpretation and prediction," to appear, *ASCE Journal of Geotechnical & Geoenvironmental Engineering*.
- [59] American Concrete Institute Code
- [60] Plaxis 3D Manual 2011 version: <http://www.plaxis.nl/files/files/2D2011-4-Scientific.pdf>
- [61] Crossrail Project website : <http://www.crossrail.co.uk>



## 8 Appendices

### A. Hardening grout model

The simulation of the grout is a key parameter for the realistic representation of the EPB construction process. The grouting procedure consists of two phases, liquid injection and the hardening solid state. The first phase is assumed to extend over one tunnel segment, and is represented as a uniform pressure (liquid state of the grout). The second phase consists of the activation of solid elements to represent the hardened state of the grout.

The grout hardening is represented using the model proposed by Kasper and Meschke, (2006); KM2006 for which the grout stiffness increases with time as shown in **Figure A.1.** with the  $E^{(1)}/E^{(28)} = 0.65$ . The time parameter was introduced in the undrained FE model by assuming an advance excavation rate of 1.0 m/hr (Melis, 1997). As a result, each excavation step corresponds to a time step of 1.5 hrs. For the first step behind the shield, uniform grout pressure is applied and for the next step, the lining and a ring of hardening grout around the lining are activated. The stiffness of the first activated grout ring, located 2 segments (i.e 3 m) behind the shield, corresponds to a 3 hours offset since based on the Kasper and Meschke, (2006) time hardening model. As shown in **Figure A.3** the gray columns represent the incremental values that correspond to the grout stiffness for each activated ring behind the shield.

Finally as the construction of the Crossrail project started, real data for the grout properties was provided. In **Figure A.2** the results of the laboratory test of the grout compressive strength as a function of time are presented. In order to correlate the compressive strength to grout stiffness, “ACI code” for concrete is used:

$$E_c = 4700 \sqrt{f'_c} \quad MPa$$

The lower bound stiffness constraint is based on recommendations of van der Stoel and van Ree, 2000 for jet grouting columns:

$$E_{cm} = 500 (f_c)^{2/3} \quad MPa$$

**Figure A.3.** depicts a comparison between the grout stiffness derived with all the aforementioned methods, as well as the constant set of grout parameters that was used in the “base case” model (**Table A.1**). It becomes clear that the examined Kasper and Meschke, (2006) model is close to the real data, since the initial grout stiffness is the one that mainly affects the most the resulting settlements as well as the structural forces in the lining. So the results of the surface displacements were identical for the Kasper and Meschke’s, (2006) approach and the “base case” model. For the structural forces in the lining (**Figure A.4**) there is a noticeable difference between the two methods for the  $K_0=1.5$  case when the lining is first activated. However, at the end of the construction both methods converge to the same value. This difference can be attributed to the fact that the stiffness of the grout for the base case model is a factor of two larger than that assumed by the KM2006 model. In this way for KM2006 model, the element representing the grout has a lower stiffness and absorbs the movements of the surrounding ground in a greater degree. So the resulting forces in the lining are more similar to those of the  $K_0=1$  case i.e. the axial force is almost constant and the moment is small (close to zero). Then as the grout stiffness increases up to a value that the deformation of the surrounding soil is transferred directly to the lining, the structural forces converge to the same value for the two methods.

**Table A.1 Grout hardening properties for Kasper and Meschke2006 versus Crossrail data**

<b>KM2006</b>		
$E_{28}$ (GPa)	$\nu$	Time offset
20	0.2	1 ring (3 hours)
<b>Constrained displacements</b>		
100 kPa grout pressure for 1 ring		
<b>Assumed excavation rate 1m/h</b>		

<b>Base case model (Crossrail)</b>		
E(GPa)	$\nu$	Time offset
1.5	0.2	1 ring (3 hours)
<b>Constrained displacements</b>		
100 kPa grout pressure for 1 ring		

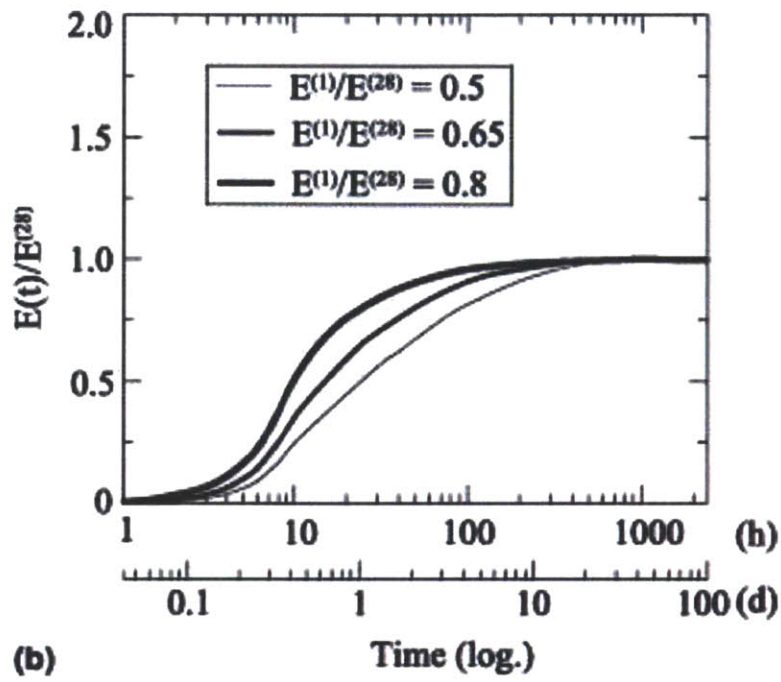


Figure A.1 Time-dependent Young's moduli of the tail void grout ( Kasper and Meschke2006)

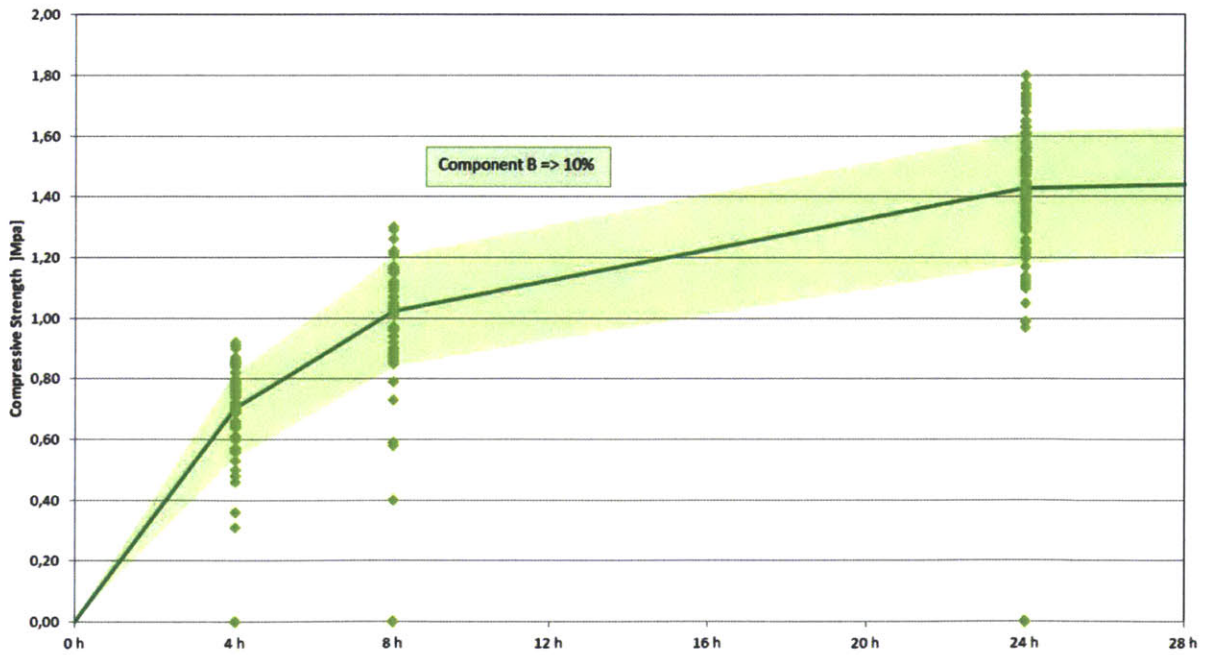


Figure A.2 Grouting cube test results: Compressive strength (MPa) as a function of time (h) (Source:Crossrail Geotechnical report 2012-2013)

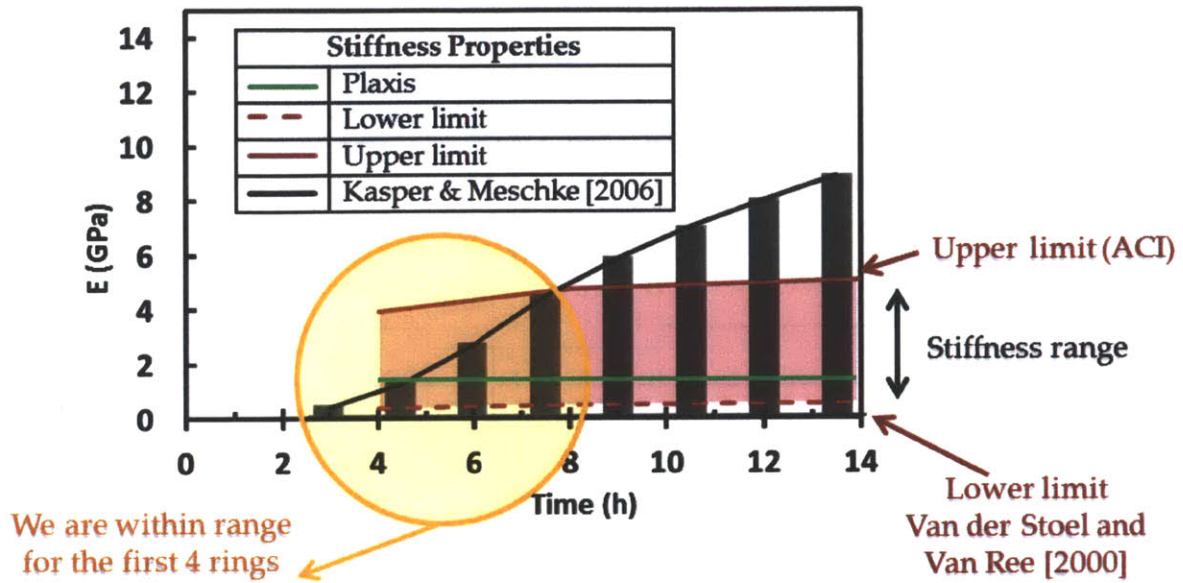


Figure A.3 Grout stiffness as a function of time. Comparison between: i) Kasper and Meschke, (2006), ii) Van der Stoel and Van Ree (2000) and ACI using laboratory data from the Crossrail Project and iii) value used for Plaxis 3D base case model.

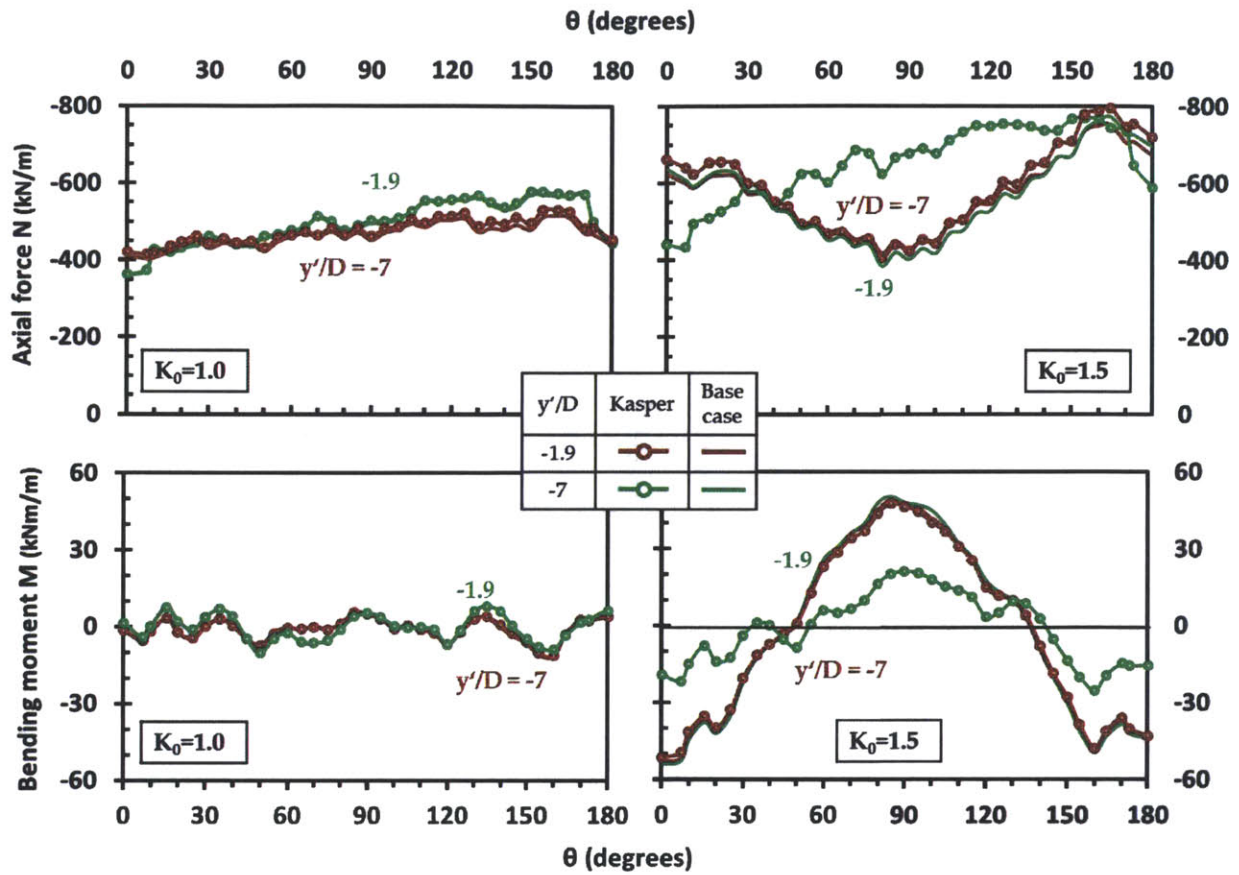


Figure A.4 Structural forces in the middle ring ( $y' = 0$ ) for Kasper and Meschke,2006 model are compared to the base case model (Crossrail) for  $K_0=1$  and  $K_0=1.5$



## B. Scripts for computing tunnel induced displacements using analytical solutions

The following code depends on the javascript library for complex numbers:

<https://github.com/dankogai/js-math-complex>

This is the javascript code for calculating the exact analytical solutions by Verruijt, 1997:

```
function Exact(params) {
  var N = params.N;
  var v = params.v;
  var h = params.h;
  var r = params.r;
  var E = params.E;
  var kappa = 3 - 4*v;
  var alpha = h/r - Math.sqrt(h*h/r/r-1);
  var alpha2 = alpha * alpha;
  var G = E / 2 / (1+v);

  var a = new Array(2*N);
  var b = new Array(2*N);
  var c = new Array(2*N);
  var d = new Array(2*N);
  var A = new Array(2*N);
  var B = new Array(2*N);

  for(var k=0;k<N*2;k++) {
    ak = Math.Complex(0);
    bk = Math.Complex(0);
    ck = Math.Complex(0);
    dk = Math.Complex(0);
    Ak = Math.Complex(0);
    Bk = Math.Complex(0);
  }

  function f(k) {return (1-alpha2)*k;}
  function g(k) {return (1+kappa*Math.pow(alpha2,-k));}
```

```

function compute(p) {
  b0 = p;
  a0 = p.con();
  for(var k=0;k<N;k++) {
    var fk=f(k),fk1=f(k+1),gk=g(k),gk1=g(k+1),gik=g(-k),gik1=g(-k-1);
    var par = fk1 * fk1 + alpha2 * gk1 * gik1;

    var aa, ab, aA, aB;
    aa = fk * fk1 + alpha2 * alpha2 * gk1 * gik;
    ab = -gk * fk1 + alpha2 * fk * gk1;
    aA = gk1*alpha2;
    aB = fk1;
    ak+1 = Math.Complex.add(
      Math.Complex.add(
        ak.mul(aa/par),
        bk.mul(ab/par)
      ),
      Math.Complex.add(
        Ak+1.mul(aA/par),
        Bk.mul(aB/par)
      )
    );

    var ba, bb, bA, bB;
    ba = (-fk * gik1 + alpha2 * fk1 * gik);
    bb = (fk * fk1 + gk * gik1);
    bA = fk1;
    bB = -gik1;
    bk+1 = Math.Complex.add(
      Math.Complex.add(
        ak.mul(ba/par),
        bk.mul(bb/par)
      ),
      Math.Complex.add(
        Ak+1.mul(bA/par),
        Bk.mul(bB/par)
      )
    );
    if(k>10 && ak+1.sub(ak).abs() < 1e-9 && bk+1.sub(bk).abs() < 1e-9 ) return ak+1;
  }
  return 0;
}

function finda0() {
  var st, en, md, vst, ven, vmd;
  st = Math.Complex(-100,-100);
  en = Math.Complex(+100,+100);
  vst = compute(st);
}

```

```

ven = compute(en);
for(var i=0;i<100;i++) {
  md = Math.Complex.add(st,en).div(2);
  vmd = compute(md);
  var re, im;
  if( vmd.re * vst.re < 0 ) en = Math.Complex( md.re, en.im );
  else st = Math.Complex( md.re, st.im );
  if( vmd.im * vst.im < 0 ) en = Math.Complex( en.re, md.im );
  else st = Math.Complex( st.re, md.im );
}
return md;
}

function computeCoefficients(obj) {
  var palpha = 1;
  for(var k=0;k<N+2;k++) {
    Ak = (Ak.con()).mul( palpha );
    Bk = (Bk).div(palpha);
    palpha *= alpha;
  }

  var a0 = finda0();
  compute(a0);

  for(var k=0;k<=N;k++) ak = ak.con();

  c0 = a0.con().neg().sub( a1.div(2) ).sub( b1.div(2) );
  d0 = a0.con().neg().sub( a1.div(2) ).sub( b1.div(2) );
  c1 = b1.con().neg().sub( a2 );
  d1 = a1.con().neg().sub( b2 );

  for(var k=2;k<N;k++) {
    ck = bk.con().neg().add( ak-1.mul( (k-1)/2.0 ) ).sub( ak+1.mul( (k+1)/2.0 ) );
    dk = ak.con().neg().add( bk-1.mul( (k-1)/2.0 ) ).sub( bk+1.mul( (k+1)/2.0 ) );
  }

  obj.a0 = a0;
  obj.Duz = 0;
  obj.Duz = obj.findDisplacements(100000,0).im;
}

this.uniform = function(ue) {
  A0 = Math.Complex(0,2*G*ue*alpha);
  B0 = Math.Complex(0,2*G*ue*alpha);
  A1 = Math.Complex(0,-2*G*ue);
  computeCoefficients(this);
}

```

```

this.ovalization = function(ud) {
  for(var k=1;k<N+2;k++)
    Bk = Math.Complex(0,2*G*ud*(Math.pow(alpha,k-1)*Math.pow(1-alpha2,2)));
  A0 = Math.Complex(0,2*G*ud*alpha*(alpha2-2));
  B0 = Math.Complex(0,2*G*ud*alpha*(alpha2-2));
  A1 = Math.Complex(0,2*G*ud*alpha2);
  computeCoefficients(this);
}

this.findDisplacements = function(x,z) {
  var zeta_nom = Math.Complex(-z,x).mul(1+alpha2).sub(h*(1-alpha2));
  var zeta_denom = Math.Complex(-z,x).mul(1+alpha2).add(h*(1-alpha2));
  var zeta = Math.Complex.div(zeta_nom,zeta_denom);

  var phi = a0;
  for(var k=1;k<N;k++) {
    phi = phi.add( ak.mul( zeta.pow(k) ) );
    phi = phi.add( bk.mul( zeta.pow(-k) ) );
  }

  var psi = c0;
  for(var k=1;k<N;k++) {
    psi = psi.add( ck.mul( zeta.pow(k) ) );
    psi = psi.add( dk.mul( zeta.pow(-k) ) );
  }

  var dphi = Math.Complex(0);
  for(var k=1;k<N;k++) {
    dphi = dphi.add( ak.mul( zeta.pow( k-1).mul(k) ) );
    dphi = dphi.add( bk.mul( zeta.pow(-k-1).mul(-k) ) );
  }
  var w = zeta.add(1).mul( zeta.con().neg().add(1).pow(2) ).div( zeta.neg().add(1) ).mul(0.5);
  var disp = phi.mul(kappa).add( dphi.con().mul(w) ).sub( psi.con() );
  return disp.div( 2*G ).sub( Math.Complex(0,this.Duz) );
}
}

```

Usage:

```

var params = {
  N : 50,
  v : 0.25,
  h : 16,
  r : 3.5,
  E : 120000,
  ue : -0.01,
  ud : 0.005
};

```

```

var Unif = new Exact( params );
Unif.uniform( params.ue );

var Oval = new Exact( params );
Oval.ovalization ( params.ud );

var displacement = Unif.findDisplacements(x,z).add( Oval.findDisplacements(x,z) );
//Gets a complex number in the form x+zi

```

This is the javascript code for calculating the approximate analytical solutions by Pinto and Whittle, 2012:

```

function ApproxUniform(params) {
  var N = params.N;
  var v = params.v;
  var h = params.h;
  var r = params.r;
  var E = params.E;
  var ue = params.ue;
  var kappa = 3 - 4*v;
  var G = E / 2 / (1+v);
  var rh = r/h;

  this.Duz = -4*ue*rh*( 8*(1-v) - (1-2*v)*rh*rh )/(4+rh*rh)/(4+rh*rh);

  function deep(x,z) {
    return Math.Complex( ue * x * r / (x*x + z*z), ue * z * r / (x*x + z*z) );
  }
  function correction(x,z) {
    var par = x*x + (z-h)*(z-h);
    return Math.Complex(
      4*ue*r * (
        (1-v)*x/par -
        (z-h)*x*z/(par*par)
      ),
      2*ue*r* (
        ( 2*(z-h)*x*x + h*( x*x - (z-h)*(z-h) ) )/(par*par) -
        2*(1-v)*(y-h)/par
      )
    );
  }
  this.findDisplacements = function(x,z) {
    return deep(x,z+h).sub( deep(x,z-h) ).add( correction(x,z) );
  }
}

function ApproxOval(params) {
  var N = params.N;
  var v = params.v;
  var h = params.h;
  var r = params.r;

```

```

var E = params.E;
var ud = params.ud;
var ue = params.ue;
var kappa = 3 - 4*v;
var G = E / 2 / (1+v);
var rh = r/h;

this.Duz = -2*ud/kappa*rh* ( (1-8*v)*rh*rh*rh*rh + (11-8*v)*4*rh*rh - 32 )/(4+rh*rh)/(4+rh*rh)/(4+rh*rh);

function deep(x,z) {
  return Math.Complex( ud * x * r / kappa *
    (kappa*(x*x+z*z)*(x*x+z*z)-(3*z*z-x*x)*(x*x+z*z-r*r)) / Math.pow(x*x + z*z,3),
    -ud * z * r / kappa *
    (kappa*(x*x+z*z)*(x*x+z*z)-(3*x*x-z*z)*(x*x+z*z-r*r)) / Math.pow(x*x + z*z,3) );
}

function correction(x,z) {
  var par = x*x + (z-h)*(z-h);
  return Math.Complex(
    8*ud*r/kappa*(
      x*(x*x+z*z-h*h)*(1-v)/(par*par)-
      x*z*(z*(x*x+z*z)+2*h*(h*h-x*x)-3*z*h*h)/(par*par*par)
    ),
    8*ud*r/kappa*(
      x*x*(2*h-z)-z*(z-h)*(z-h)*(1-v)/(par*par)-
      (z-h)*(h*z*(z-h)*(z-h)-x*x*((x*x+z*z)+h*(z+h)))/(par*par*par)
    )
  );
}

this.findDisplacements = function(x,z) {
  return deep(x,z+h).sub( deep(x,z-h) ).add( correction(x,z) );
}
}

```

#### Usage:

```

var params = {
  N : 50,
  v : 0.25,
  h : 16,
  r : 3.5,
  E : 120000,
  ue: -0.01,
  ud: 0.005
};

var Unif = new ApproxUniform( params );

var Oval = new ApproxOval( params );

var displacement = Unif.findDisplacements(x,z).add( Oval.findDisplacements(x,z) );

//Gets a complex number in the form x+zi

```

This is the Matlab code for matching the computed tunnel cavity deformations using the stress reduction method ( $\beta$ -method) to the approximate analytical solutions by Pinto and Whittle, 2012.

```

clc;
clear;
R = 3.5;
H = 16;
v = 0.49;

A = xlsread('test.xlsx');
X = A(:,3);
Z = A(:,4);
Ux = A(:,5);
Uz = A(:,6);
rows, cols = size(A);
e = 1e-6;
n = 0;
j = rows;

for i=1:rows
    if (X(i)>= 0) && (X(i)<(3.5+e))
        if abs(X(i)^2+(Z(i)+16)^2 -3.5^2)<e && ( n==0 || (abs(X(i)-x(n))> e) )
            n = n+1;
            x(n) = X(i);
            z(n) = Z(i);
            ux(n) = Ux(i);
            uz(n) = Uz(i);
            theta(n) = atan2(x(n),(z(n)+16));
        end
    end
end
n
%Duz
%convergence
ac = 4*R/H*(8*(1-v)-(1-2*v)*(R/H)^2)/(4+(R/H)^2)^2;

%ovalization
ao = 2/(3-4*v)*R/H*((1-8*v)*(R/H)^4+(11-8*v)*4*(R/H)^2-32)/(4+(R/H)^2)^3;
rows,cols = size(x);

for k=1:cols
    a((2*k-1))= cos(theta(k));
    b((2*k-1))= -cos(theta(k));

    ab((2*k-1),1)=a((2*k-1));
    ab((2*k-1),2)=b((2*k-1));
    ab((2*k-1),3) = 1;

    a((2*k))=sin(theta(k));
    b((2*k))=sin(theta(k));
end

```

```

ab((2*k),1) = a((2*k));
ab((2*k),2) = b((2*k));
ab((2*k),3) = 0;

c((2*k-1),1)=uz(k);
c((2*k),1)=ux(k);
end
displacements=ab\c
nu=ab*displacements;

for ki=1:cols
    nuz(ki)=nu(2*ki-1);
    nux(ki)=nu(2*ki);
    nutotal(ki)=(nux(ki)^2+nuz(ki)^2)^0.5;

end
for ki=1:cols

    utotal(ki)=(ux(ki)^2+uz(ki)^2)^0.5;

end
figure(1)
plot( x + 100*nu((1:cols)*2)', z + 100*nu((1:cols)*2-1)', 'r', x+ux*100,z+100*uz,'g' );

figure(2)
plot( theta,nutotal,'r', theta,utotal,'g+' );

```